1-24-2024

Control and Estimation of Unmanned Aerospace Vehicles in the presence of Constraints and Dynamic Uncertainties

Abhijit Dongare
Syracuse University

Abstract

In the first part of this dissertation, we consider the control of autonomous systems in the presence of pointwise-in-time state and control constraints. Firstly, we propose the attitude and pointing control of a rigid body in the presence of constraints. Artificial potentials are used to achieve desired tracking and avoid pointing direction constraints. The proposed control law ensures the asymptotic convergence to the desired attitude and pointing direction. Additionally, the control of driftless control-affine systems is also considered. The feedback system converges in a stable manner to the desired safe set in the state space, while avoiding the unsafe exclusion zones in the state space and maintaining control input constraints. The problem of constraints satisfaction is then extended to the case where system model is unknown or partially known. The design of reference governors is proposed to the data-driven control of systems with unknown input-output dynamics. The Lyapunov analysis ensure that the output of the reference governor-based control system converges to a desired output trajectory that meets the constraints.

In the second part of this dissertation, we consider state estimation on the Lie group of rigid body motions, $\mathrm{SE}(3)$. A finite-time stable pose estimation scheme is proposed to provide estimates of the pose from three-dimensional point cloud measurements obtained by a body-mounted optical sensor(s). This observer is designed directly on the Lie group of rigid body motions, SE(3), and is model-free. The proposed Lyapunov analysis shows finite-time stability and its robustness to bounded measurement noises.

CONTROL AND ESTIMATION OF UNMANNED AEROSPACE VEHICLES IN THE PRESENCE OF CONSTRAINTS AND DYNAMIC UNCERTAINTIES

by

Abhijit Ulhas Dongare

B.E., University of Mumbai, 2015
M.S., Syracuse University, 2018

Dissertation
Submitted in partial fulfillment of the requirements for the degree of
Doctor of Philosophy in Mechanical and Aerospace Engineering.

Syracuse University
December 2023

विद्या ददाति विनयं विनयाद्याति पात्रताम् ।
पात्रत्वाद्धनमाप्नोति धनाद्धर्मं ततः सुखम् ॥

(True knowledge leads to discipline,
from discipline comes worthiness,
from worthiness one obtains wealth,
from wealth one does good deeds,
that leads to happiness).

Acknowledgements

Over the course of five years, I have accumulated a debt of gratitude. I would like to start with my advisor, Dr. Amit Sanyal. I thank him for his efforts, his patience for all this years. He instilled a great deal motivation, confidence and curiosity in me. The motivation which will help me keep going for years to come. I learned a lot from him, especially his dedication and ability to solve problems.

I thank Dr. Ilya Kolmanovsky for his efforts and giving me an opportunity to attend his class. I am also grateful to Dr. William Wylie and Dr. Victor H Duenas for classes they taught.

I thank Dr. Sasi P. Viswanathan, who provided me opportunity to work on hardware stuff and his encouragement. I also thank Dr. Reza Hamrah and Ningshan for their contribution and encouragement.

I thank my friends Romesh Prasad, Dr. Joshua Burton and Joshua Jessen for all the scientific discussions.

I thank Smit Pandit, Reshma Pandit, Bishal Biswas, Harshal More, Ninad Bhavsar, Sumit Edke and Ronit Das for all the fun times we had.

I thank everyone mentioned above for their efforts and I hope that one day I will be worthy of all their affection.

Finally, I am eternally grateful to my parents and sister Jai, who supported and shaped me throughout my life.

September, 2023 Abhijit Dongare

Contents

List of Figures

Chapter 1

Introduction

Autonomous unmanned vehicles have gained significant attention over past few years. The applications of these vehicles span multiple domains such as military, space exploration, inspection of infrastructure like buildings and bridges, farming, underwater research and exploration, wildlife tracking, package delivery, and remote sensing. Autonomous systems pose us with a number of challenges, including guidance, trajectory tracking and constraints satisfaction that has attracted the attention of many researchers. Constraints in the autonomous systems are limitations that system must adhere to for safe and efficient operation. These constraints primarily consists of pointwise-in-time state and control constraints.

The first phase of this work, which includes Chapters 2 and 3, outlines attitude tracking control and pointing direction control in the presence of constraints using artificial potentials. The literature on artificial potentials includes path planning for collision avoidance, formation control. Artificial potentials have been used as a way for collision avoidance (Khatib and Maitre, 1978). Collision avoidance can be distributed among several levels of control as described in (Khatib, 1985) and (Khatib, 1986) instead of just as a

high level problem. This significantly helps to increase the safety in real-time operations. Obstacles detected can be avoided by constructing repulsive artificial potential fields around them, and destinations and waypoints are represented as attractive potentials. The concept of artificial potentials has also been used in robot path planning (Rimon and Koditschek, 1992). The artificial potential function can be designed to include information on the environment. Guidance for multiple robots can also be carried out using artificial potentials (Warren, 1990). Artificial potentials can be used for fast and efficient path planning by prioritizing robots accordingly. Artificial potentials have also been applied in spacecraft formation control (Renevey and Spencer, 2019). A scheme for autonomous rendezvous in orbit with a target can be designed using an artificial potential function (Lopez and McInnes, 1995). Spacecraft collision avoidance during a rendezvous maneuver using an artificial potential for guidance and sliding mode control for tracking is another application (M. Mancini and Punta, 2020). Artificial potential using relative orbital elements to achieve a relative orbit was treated in (Spencer, 2016). Another application of artificial potential is for in orbit servicing (Tatsch and Fitz-Coy, 2006). This concept uses a simple attractive and a dynamic repulsive artificial potential, which prioritizes obstacles to avoid by assigning weight factors. Applications to formation control for multiple unmanned aerial vehicles are discussed in (Yin, Cam, and Roy, 2017) and (Skyrda, Chepizhenko, and Davydenko, 2019). The former chapter describes formation tracking control in a constrained space. It uses the formation potential field which is a modified artificial potential field that maintains the formation along with collision avoidance among the vehicles and also the surroundings. The latter chapter describes a formation potential field for formation control and collision avoidance in dynamic environments. Another approach involves use of logarithmic barrier potentials in terms of

quaternions, for spacecraft attitude control in order to avoid constraints and remain in certain zones (Lee and Mesbahi, 2011).

These prior works use feedback of the full attitude state of the rigid body. However, the full attitude state may not always be available or necessary for pointing control. For pointing (boresight) control, the problem is one of *reduced attitude control* of a rigid body, where the configuration space is the sphere $\mathbb{S}^2$, consisting of unit vectors in $\mathbb{R}^3$. Spacecraft attitude pointing control with sun direction vector avoidance for large angle maneuvers using Euler angles was carried out in (Mclnnes, 1994). Attitude control for large angle rotations using quaternions are studied, e.g., in (Wie and Barba, 1985). Among the prior literature related to reduced attitude control, (Bullo and Murray, 1995) is focused on control on $\mathbb{S}^2$ and stabilization of the spacecraft about an unactuated axis of rotation. An extensive study of control on spheres is performed in (Brockett, 1973). In (Isidori, 1995), an underactuated spacecraft is asymptotically stabilized using state feedback law. A detailed review of rigid body attitude control, with particular emphasis on stability and stabilization, was provided in (Chaturvedi, Sanyal, and McClamroch, 2011). It describes full and reduced attitude control on the configuration spaces $\mathrm{SO}(3)$ and $\mathbb{S}^2$ respectively, and almost global stability on the respective state spaces. Boresight control and guidance is studied in (Pong and Miller, 2015), which also discusses different scenarios for applications like pointing, tracking and searching. Other prior research on reduced attitude (or pointing direction) control includes, e.g., (Tsiotras and Longuski, 1994), (Chaturvedi, McClamroch, and Bernstein, 2009), (Krishnan, Reyhanoglu, and McClamroch, 1994), and (Chaturvedi and McClamroch, 2007). Constraints in attitude control is another relevant area of research in attitude control with obvious practical applications. Unmanned vehicles and spacecraft can have different types of constraints that limit attitude control

inputs, including limits on angular velocity and torque, besides pointing direction constraints. Prior literature has explored different control and state constraints in attitude and reduced attitude control, and solutions to overcome them. Artificial potential functions have been used for navigation of a vehicle towards a desired set or reference, while avoiding obstacles (Mclnnes, 1994),(Lee and Mesbahi, 2014),(Kulumani and Lee, 2017). Undesirable attitude and pointing direction avoidance was studied in (Spindler, 2002), using geometric mechanics. A cost function was optimized to ensure the avoidance of an excluded direction. Logarithmic barrier potential functions were used in (Lee and Mesbahi, 2011), (Kulumani and Lee, 2017) to avoid exclusion zones in pointing direction. The former work also had a mandatory zone constraint and used a back-stepping controller. The latter work used an adaptive controller to stabilize the system in presence of an unknown disturbance. Another study of exclusion and mandatory zones was given in (Hablani, 1999). Angular velocity constraint along with dynamic pointing constraint was considered in (Hu, Chi, and Akella, 2019). The velocity constraint was satisfied by limiting the angular velocity error, leading to conservative results. Spacecraft formation control in the presence of attitude and position constraints was considered in (Garcia and How, 2005). They employed rapidly-exploring random trees for path planning along with a smoother for optimization. The control of an underactuated axisymmetric spacecraft was considered in (Tsiotras and Luo, 2000). A discontinuous control law was designed for asymptotic tracking and stabilization. Note that discontinuous control has practical impediments for spacecraft control, where it may excite structural vibrations in flexible space structures.

An approach involving Model Predictive Control was also proposed in (Gupta et al., 2015) to satisfy the control constraints. Both thrust and exclusion zone constraints were

considered. A fast solver method for the optimization problem was also proposed. The work in (Nicotra et al., 2020), considers actuator saturation and exclusion zones. This is a two step scheme, where a reference trajectory is generated in quaternion space in the first step. Then a reference governor is applied to the pre-stabilized system to satisfy the control constraints. Along the same lines, (Nakano et al., 2018) studies torque and inclusion zone constraints on $\mathrm{SO}(3)$ using an explicit reference governor. However, these schemes often rely on online optimization, for which significant computational power is required to implement in real time. Additionally, these schemes also employ artificial potential-like functions for navigation. Geometric tracking controllers based on the Special Euclidean group $\mathrm{SE}(3)$ that avoid singularities and instabilities of other control laws, were reported in (Shi, Zhang, and Zhou, 2015; Lee, Leok, and McClamroch, 2010; Mellinger and Kumar, 2011; Kushleyev et al., 2013; Rudin et al., 2011; Fernando et al., 2011; Lee, Leok, and McClamroch, 2012; Lee et al., 2013; Goodarzi, Lee, and Lee, 2015; Invernizzi and Lovera, 2017). It is worth mentioning that all these controllers are obtained in continuous time.

Attitude tracking control using time-varying artificial potentials: This work uses the framework of geometric mechanics along with time-varying artificial potential fields to guide a rigid body through desired attitude waypoints and settle into a desired final rest attitude. The concepts of "virtual leaders" along with artificial potentials on the Lie group of rigid body motions in three dimensional Euclidean space is used to control multiple autonomous vehicles (Leonard and Fiorelli, 2001). Spacecraft formation control in the framework of geometric mechanics can be done using artificial potentials and a virtual leader (Lee, Sanyal, and Butcher, 2015). Artificial potentials is also used for collision avoidance in Riemannian manifolds (Assif et al., 2018). The work in (Kulumani and Lee, 2017) involves geometric control of attitude using both attractive and repulsive potentials

for guidance. The desired attitude is obtained asymptotically while avoiding undesirable orientations. The novelty of this work is that it uses time-varying artificial potentials for guidance through desired waypoints on the Lie group $SO(3)$ of rigid body attitude. Further, the time-varying artificial potentials used here are defined only on closed (compact) intervals of time, designed to coincide with time intervals at which the desired waypoints should be reached.

Attitude pointing control using artificial potentials: Our approach to pointing control in the presence of control torque and pointing direction constraints, uses smooth artificial potentials and knowledge of maximum permissible angular velocities (or energy level) of the rigid body. This chapter is organized as follows. Section **??** describes the attitude pointing control problem and introduces required notation. Section **??** describes the artificial potential functions. The attractive potential function is centered at the desired pointing direction. This attracts the body-fixed sensor pointing direction to the desired pointing direction. The repulsive potential function is designed to avoid an undesirable pointing direction.

The Chapter 4 focuses on guidance and control of driftless control-affine systems in the presence of constraints. The objective is to guide the system to a target state or a subset of the state space, while avoiding exclusion zones that may have obstacles, and enforcing control input constraints.

Our approach in this chapter exploits control barrier functions. A barrier function of states of a dynamical system, is a function that increases in value when the state approaches the boundary from inside of a constraint admissible region that is a sublevel set of this function. A control barrier function is a barrier function for a controlled dynamical system such that the system satisfies the barrier function condition (Ames et al., n.d.).

These functions can be used to satisfy output, state, or control input constraints (Tee, Ge, and Tay, 2009), (Wills and Heath, 2004). Control barrier functions in the context of barrier certificates and control Lyapunov functions are studied in (Wieland and Allgöwer, 2007), while their relations to control Lyapunov functions are studied in (Ames, Grizzle, and Tabuada, 2014). The recently introduced framework of integral control barrier functions (Ames et al., 2021) can be used to simultaneously satisfy control input and state exclusion zone constraints, and is applicable to the problem posed in this work. In this chapter, the design of the barrier function is based on bump functions that have compact support.

The approaches mentioned till now are primarily used for systems well-known dynamics models with little or no uncertainties. However, the increase in the complexity of practical control systems and applications, poses significant challenges in deriving accurate models of nonlinear systems. In many applications involving control of autonomous vehicles operating in remote or inaccessible environments, obtaining an accurate model may be impossible as the environmental uncertainties are unknown a priori. This leads to imperfections and uncertainties in the model relating inputs and outputs of the system. Applications where nonlinearly stable and robust data-enabled control schemes can be a game changer, include a large class of autonomous systems, legged robots, and aerospace vehicles. For these systems, control design based on data-driven techniques represents an attractive approach for feedback control in real time. The chapter 5 introduces data-driven based control of nonlinear control-affine system with uncertain dynamics. Chapter 6 introduces design of reference governors for constrained data-driven control.

Feedback control of uncertain nonlinear systems while ensuring stability and robustness is a challenging research problem of long-standing interest. Design of these controllers based on a mathematical model of a system is a widely used approach. However, the increase in the complexity of practical control systems and applications, poses significant challenges in deriving accurate models of nonlinear systems. In many applications involving control of autonomous vehicles operating in remote or inaccessible environments, obtaining an accurate model may be impossible as the environmental uncertainties are unknown a priori. This leads to imperfections and uncertainties in the model relating inputs and outputs of the system. Applications where nonlinearly stable and robust data-enabled control schemes can be a game changer, include a large class of autonomous systems, legged robots, and aerospace vehicles. For these systems, control design based on data-enabled techniques represents an attractive approach for feedback control in real time. The main contribution of this work is to provide a stable and robust real-time uncertainty identification and output tracking control scheme for systems with uncertain dynamics and desired output trajectory tracking.

Data-driven and data-enabled control schemes include the classical proportional-integral-derivative (PID) schemes that remain an industry standard. A data-enabled predictive control design for an unknown system was proposed in (Coulson, Lygeros, and Dörfler, 2019; De Persis and Tesi, 2020), which computes a data-enabled optimal control using a receding horizon approach. This approach is analogous to model-predictive control (MPC) for a linear time-invariant system. Learning-based MPC with robustness and stability properties is given in (Aswani et al., 2013) and with safety guarantees in (Wabersich and Zeilinger, 2018). Nonlinear MPC with a cost function tuned using reinforcement learning is used for data-enabled control in the case of an uncertain dynamics model in (Gros and

Zanon, 2019). Early work on the use of neural networks for the control of unknown nonlinear systems appeared in (Li and Slotine, 1989; Psaltis, Sideris, and Yamamura, 1988). Later works using adaptive neural networks were applied to uncertain MIMO nonlinear systems in presence of input nonlinearities (Chen, Li, and Chen, 2016), for systems with time-delays (Chen et al., 2009) and systems with state constraints (He, Chen, and Yin, 2015). A data-enabled approach in the presence of actuation uncertainty was given in (Taylor et al., 2021), which used learning-based certificate functions (Boffi et al., 2021). Most of these existing nonlinear data-enabled control scheme designs often require online optimization and have limited stability (e.g., (Hou and Jin, 2011; Tanaskovic et al., 2017; Dai and Sznaier, 2021)).

A model-free control approach, termed intelligent PID control, was proposed in (Fliess and Join, 2013), (Fliess, 2009). In this approach, the lack of a given mathematical model for a single-input single-output (SISO) system is countered by an ultra-local model that describes the unknown input-to-output dynamics of the system. The biggest advantage of this approach is that the ultra-local model (ULM) is not an approximation of the true dynamics, but an exact local representation of the system based on the given input-output data at each time instant. In addition, it does not require online optimization, which makes it computationally very light. These advantages give it a considerable edge when compared to alternate approaches like reinforcement learning based on neural nets, data-enabled predictive control, Koopman operator-based approaches, and their combinations (Brunke et al., 2022; Kaiser, Kutz, and Brunton, 2018). The application of this approach to control of a quadrotor was considered in (Younes et al., 2016). The integration of MPC with an ULM ("ULMPC control") was proposed in (Wang and Wang, 2020).

A generalization of the ultra-local model to multi-input multi-output (MIMO) nonlinear systems was formulated in (Sanyal, 2022). This generalization uses a black box MIMO ultra-local model representation of the system in discrete time. Although a majority of the prior literature uses continuous time methods, the data-enabled scheme in (Sanyal, 2022) uses a discrete-time ULM with model estimation and control schemes that are Hölder-continuous. This makes it more suitable for implementation on onboard computers for autonomous systems, besides ensuring the robustness and stability of the overall system with discrete-time control inputs and output measurements. In this work, we extend the approach in (Sanyal, 2022) by using a gray-box ultra-local model for a nonlinear control-affine system with a control influence matrix and known and unknown parts in its input-to-output dynamics.

A data-enabled predictive control design for an unknown system was proposed in (Coulson, Lygeros, and Dörfler, 2019) which computes a data-driven optimal control using a receding horizon approach. This approach is analogous to MPC for a linear time-invariant case. The application of model-free control to a quadrotor is considered in (Younes et al., 2016). The integration of MPC with an ultra-local model is proposed in (Wang and Wang, 2020). An example of a learning-based reference governor for constraint satisfaction is proposed in (Liu et al., 2019) and (Liu et al., 2020). This scheme modifies the governor parameters over time to ensure constraint satisfaction. In the former work, the constraints are satisfied only after the learning phase of the model, while in the latter work, constraints are satisfied during the learning phase of the model as well.

Chapter 7 proposes pose estimation scheme on $\mathrm{SE}(3)$ using vision based sensors. State estimation on the Lie group of rigid body motions, $\mathrm{SE}(3)$, is essential for aerial vehicles, spacecraft, and underwater vehicles. In the absence of global navigation satellite systems

(GNSS) in these applications, onboard sensors that include vision, lidar, infrared, sonar, and inertial sensors are used to provide information on the pose (position and orientation) of the vehicle body with respect to an inertial (spatial) reference frame.

Pose estimation in real time is required for feedback control of translational and rotational motion during the operations of autonomous vehicles. The set of all possible poses of a rigid body is given by the special Euclidean group in three dimensions, denoted as $\mathrm{SE}(3)$ in (Bloch et al., 2003; Bullo and Lewis, 2004). This group is a semi-direct product of the real Euclidean linear space of translations $\mathbb{R}^3$ and the Lie group of 3×3 real orthogonal matrices with determinant 1, called the special orthogonal group and denoted $\mathrm{SO}(3)$. The nonlinear and compact configuration space of three-dimensional rotations, $\mathrm{SO}(3)$, makes $\mathrm{SE}(3)$ a nonlinear and non-contractible space, and therefore, attitude and pose estimation are inherently nonlinear problems. As the translational and rotational motions of rigid bodies are usually coupled and their attitude cannot be directly measured by onboard sensors, a pose estimation scheme has to compute the pose from vector measurements obtained from sensors mounted on the rigid body.

This work proposes a finite-time stable pose estimation (FTS-PE) scheme to provide estimates of the pose from three-dimensional point cloud measurements obtained by a body-mounted optical sensor(s). This scheme has the advantages of: (1) estimating the pose of the body in a finite-time stable manner over the entire state space of rigid body motions; and (2) not requiring knowledge of the dynamics model of the vehicle. This estimation scheme can enhance the autonomy and reliability of autonomous vehicles in uncertain environments without (continuous) access to global navigation satellite systems (GNSS). In practice, the dynamics of a vehicle may not be perfectly known in such environments, especially when it is under the action of poorly known forces and moments.

Attitude estimation has a well-established history, with early research such as (Black, 1964; Wahba, 1965) proposing static attitude determination methods for each set of direction vector measurements. However, the performance of static attitude determination schemes can be unsatisfactory in the presence of measurement noise and bias components. Therefore, estimation schemes like the extended Kalman filter ((Shuster, 1990; Choukroun, Bar-Itzhack, and Oshman, 2006)) and multiplicative extended Kalman filter ((Markley, 1988)) are often used for attitude estimation. Nevertheless, these schemes may perform poorly due to the restrictive assumptions they make about measurement noise, process noise, and state transitions, as noted by (Crassidis, Markley, and Cheng, 2007). Other prior approaches focused on nonlinear estimation schemes given by (Bonnabel, Martin, and Rouchon, 2009; Mahony, Hamel, and Pflimlin, 2008; Vasconcelos et al., 2010; Markley, 2006; Sanyal, 2006; Lageman, Trumpf, and Mahony, 2010; Moutinho, Figueirôa, and Azinheira, 2015), where the attitude estimate evolves on the Lie group $SO(3)$ (or $TSO(3)$, if angular velocity is also being estimated). The emergence of such estimators was to avoid the use of unit quaternions or local coordinate descriptions like Euler angles to represent attitude. This is because local coordinates encounter singularities in representing attitude globally, while attitude estimators using unit quaternions for attitude representation may exhibit unwinding-type instability unless they identify antipodal quaternions with a single attitude. This instability can also result in longer convergence times compared to stable schemes. However, estimators designed directly on the Lie group of rigid body motions do not suffer from singularities and unwinding, which are common in estimators using coordinate descriptions of attitude and unit quaternions, respectively. More recent work on nonlinear deterministic estimation schemes in the geometric framework includes (Hamrah, Warier, and Sanyal, 2021; Mahony and Hamel,

2017; Hamel, Hua, and Samson, 2020; Van Goor et al., 2021; Wang, Gamagedara, and Lee, 2022; Mahony, Van Goor, and Hamel, 2022).

Due to the geometry of the compact manifold $\mathrm{SO}(3)$, no continuous attitude observer can provide convergence of the attitude estimation error to identity from all initial attitude and angular velocity estimation errors as shown by (Hamrah, Warier, and Sanyal, 2021). This is shown in prior work like (Bhat and Bernstein, 2000) and (Chaturvedi, Sanyal, and McClamroch, 2011). A continuous attitude observer or controller can, at best, be *almost global* in terms of its region of attraction, as in (Chaturvedi, Sanyal, and McClamroch, 2011). For an attitude observer, almost global stability implies that the attitude estimate converges to the true attitude for almost all initial attitude estimates, except those in a set of zero measure in the state space. The attitude estimation scheme presented in (Izadi et al., 2016) follows the variational framework of the estimation scheme reported in (Izadi and Sanyal, 2014), but includes bias in angular velocity measurements and estimates a constant bias vector. Moreover, it exhibits almost global asymptotic stability, similar to the bias-free variational attitude estimator given in (Izadi and Sanyal, 2014).

There are advantages to having finite time stable pose estimation schemes: they have been shown to be more robust to disturbances and noise and provide faster convergence than an asymptotically stable scheme with similar initial transience. Additionally, a finite time stable estimation scheme can automatically make a “separation principle" possible in the case estimated state variables are used for feedback control, as observer estimates converge to true states in finite time. Finite time stable estimation schemes using sliding mode controllers and neural networks are proposed by (Li et al., 2015; Zou et al., 2011), which are not continuous. Our prior work includes (Bohn and Sanyal, 2014) and (Sanyal, Izadi, and Bohn, 2014), which proposed almost global finite time stable attitude

observers. However, the exact dynamics model including the moment of inertia is assumed to be available for estimation and the angular velocity bias was not considered. The scheme proposed by (Warier, Sanyal, and Prabhakaran, 2019) enables FTS estimation of attitude in the absence of bias, and (Hamrah, Warier, and Sanyal, 2021) presents a nonlinear FTS attitude estimation scheme that accounts for unknown bias in angular velocity measurements, both without requiring knowledge of the dynamics model of the rigid body.

This work introduces a novel pose estimation scheme, referred to as the Finite-Time Stable Pose Estimation (FTS-PE) scheme, which achieves almost global finite-time stability. The key features of this FTS-PE scheme are: (1) it performs attitude estimation directly on the Special Euclidean group $\mathrm{SE}(3)$, thereby avoiding singularities or unwinding; (2) the FTS-PE is model-free, implying that it does not rely on any assumptions about the attitude dynamics model, including knowledge of the moment of inertia or the measurement noise model; (3) the FTS-PE is continuous, Lyapunov stable and exhibits almost global finite-time convergence to the true pose and velocities in the absence of measurement errors; and (4) it is robust to time-varying noise with unknown statistics in measured angular and translational velocities, as is theoretically demonstrated.

The contributions in this dissertation have been submitted or published in the following conference proceedings and journals.

- A. Dongare, A. K. Sanyal, H. Eslamiat and S. P. Viswanathan Guidance and Tracking Control for Rigid Body Attitude Using Time-Varying Artificial Potentials, in Proceeding of the AAS/AIAA Astrodynamics Specialist Conference, 2020.

- A. Dongare, R. Hamrah, and A. K. Sanyal, Attitude Pointing Control using Artificial Potentials with Control Input Constraints, in 2021 American Control Conference

(ACC), New Orleans, USA, May 25-28, 2021.

- A. Dongare, I. Kolmanovsky, A. K. Sanyal and S. P. Viswanathan, Integrated Guidance and Control of Driftless Control-affine Systems with Control Constraints and State Exclusion Zones, in American Control Conference (ACC), Atlanta, GA, USA, June 8-10, 2022

- A. Dongare, R. Hamrah, and A. K. Sanyal, Discrete-time Control of Nonlinear Control-Affine Systems with Uncertain Dynamics, submitted in 9th Indian Control Conference (ICC-9).

- A. Dongare, R. Hamrah, I. Kolmanovsky and A. K. Sanyal, Reference Governor for Constrained Data-Driven Control of Aerospace Systems with Unknown Input-Output Dynamics, in 7th IEEE Conference on Control Technology and Applications, August 16-18, Bridgetown, Barbados

- A. Dongare, R. Hamrah, and A. K. Sanyal, Finite-time Stable Pose Estimation on $\mathrm{SE}(3)$ using Onboard Optical Sensors, submitted in Automatica.

The remainder of this dissertation is structured as follows. Chapter 2 gives problem formulations and some mathematical preliminaries, and also presents a attitude tracking control scheme in continuous time for a rigid body in SO(3), using time-varying artificial potentials. Chapter 3 deals with pointing direction control of a rigid body with a body-fixed sensor, in the presence of control constraints and pointing direction constraints. In Chapter 4, an integrated guidance and control scheme for autonomous control-affine systems is proposed. The admissible control inputs is represented with a convex and compact ellipsoidal set and convex ellipsoidal sets are the exclusion zones to be avoided in

the state space. In Chapter 5, an approach for data-enabled control of discrete nonlinear control-affine systems with uncertain (“gray-box") dynamics is proposed. Chapter 6 describes the design of reference governor to satisfy pointwise-in-time output and control constraints in the setting of data-driven control. Chapter 7 presents a finite-time stable pose estimation scheme for autonomous vehicles undergoing rotational and translational motion in three dimensions, using measurements from onboard optical sensors. Chapter 8 reports the numerical simulation results and comparison of some of the state-of-the art pose estimation schemes as well as experimental results. Chapter 9 concludes the dissertation and outlines possible future directions.

Chapter 2

Guidance and Tracking Control for Rigid Body Attitude Using Time-Varying Artificial Potentials

In this chapter, we present a guidance and attitude tracking control scheme in continuous time for a rigid body in SO(3), using time-varying artificial potentials. This novel idea leads to generation of an attitude trajectory that passes through desired attitude waypoints and feedback tracking of this trajectory.

In 2.1, attitude dynamics of a rigid body on SO(3) and attitude waypoints is given. These waypoints can also be used for avoiding attitude or pointing direction constraints so that safe attitude navigation is ensured.

In 2.2, artificial time-varying potential fields at these waypoints that are attractive, are introduced. Bump functions of time, which are smooth but not real analytic, are used to generate these potentials at the desired attitude waypoints. For the terminal attitude, a different type of smooth function is used. The rigid body attitude in these time-varying potential fields gets attracted towards the desired attitude waypoints during certain time

periods. This generates an attitude trajectory passing through these desired waypoints sequentially in time. A Lyapunov analysis is carried out to show stable attitude tracking through the desired waypoints and ending at the terminal attitude, using these time-varying artificial potentials.

In 2.3, numerical simulations are carried out to test the performance of this attitude guidance and tracking scheme.

2.1 Problem Formulation

2.1.1 Coordinate Frame Definition

The configuration space of rigid body attitude motion is the Lie group $\mathrm{SO}(3)$. The attitude is described by a rotation matrix relating a body-fixed coordinate frame to an inertial coordinate frame. We consider a coordinate frame $\mathcal{B}$ fixed to the body and another coordinate frame $\mathcal{I}$ that is fixed in space and takes the role of an inertial coordinate frame. Let $R \in \mathrm{SO}(3)$ denote the orientation (attitude) of the body, defined as the rotation matrix from frame $\mathcal{B}$ to frame $\mathcal{I}$.

2.1.2 Rigid Body Attitude Dynamics with Control Input Torque

The model for attitude dynamics of a rigid body acting under a control torque is outlined here. The attitude of the rigid body is given by the rotation matrix $R \in \mathrm{SO}(3)$ from body-frame coordinate frame to an inertial frame. The angular velocity of the rigid body is represented in body-fixed frame and is denoted by $\Omega \in \mathbb{R}^3$. The attitude kinematics is given by

$$\dot{R} = R\Omega^{\times}, \tag{2.1}$$

where $(\cdot)\colon \mathbb{R}^3 \to \mathfrak{so}(3)$ is the skew-symmetric cross product operator and $\mathfrak{so}(3)$ is the Lie algebra of $\mathrm{SO}(3)$, identified with the linear space of 3×3 skew-symmetric matrices. Note that the cross-product operator is given by:

$$x^{\times} = \begin{bmatrix} x_1 \\ x_2 \\ x_3 \end{bmatrix}^{\times} = \begin{bmatrix} 0 & -x_3 & x_2 \\ x_3 & 0 & -x_1 \\ -x_2 & x_1 & 0 \end{bmatrix}. \tag{2.2}$$

The attitude dynamics is given by

$$J\dot{\Omega} = -\Omega \times J\Omega + \tau_c, \tag{2.3}$$

where J is the inertia matrix of the body expressed in the body-fixed coordinate frame and $\tau_c \in \mathbb{R}$ is the control input torque which is applied to the rigid body about its center of mass. The rigid body here is considered to be stationary in terms of translational motion.

2.1.3 Attitude Waypoint Navigation

The goal of the attitude waypoint navigation is to enable smooth reorientation of the rigid body from its initial attitude to the desired final attitude. This navigation is realized by a given finite set of attitude waypoints through which the rigid body is required to reorient itself. These waypoints are given in the form of rotation matrices from body-fixed frame

$\mathcal{B}$ to inertial frame $\mathcal{I}$ ordered according to a strictly increasing sequence of time instants, as follows:

$$\begin{aligned} &R_{d_1}, R_{d_2}, ..., R_{d_n} \in \mathrm{SO}(3), \\ &\text{with } R_{d_i} = R_d(t_i) \in \mathrm{SO}(3) \text{ and } t_1 < t_2 < ... < t_n. \end{aligned} \tag{2.4}$$

Here, $R_{d_1}, R_{d_2}, ..., R_{d_{n-1}}$ are the intermediate attitude waypoints and $R_{d_n} = R_f$ is the final attitude waypoint.

2.2 Time-Varying Artificial Potential

The approach for guidance and navigation of the rigid body attitude, with equations (2.1) and (2.3) describing its attitude motion, is formulated here. A bump function is used to design a time-varying artificial potential function for attitude guidance, as described here. The artificial potential function is designed as the product of a time-varying bump function that has compact support in time, and a Morse function on the Lie group of rigid body rotations. A Morse function is a non-degenerate function with a disjoint set of critical points (Milnor, Spivak, and Wells, 1969). Positive definite Morse functions form the best candidates for Lyapunov functions on *non-contractible* manifolds, i.e., spaces that cannot be contracted continuously to a point. The stability analysis of the overall guidance and tracking control is carried out to show stable trajectory generation through these waypoints, using Lyapunov analysis with a time-varying Morse-Lyapunov function.

2.2.1 Bump Functions for Intermediate Waypoints

At each intermediate attitude waypoint, we design a time-varying function to describe the potential field. This is in the form of a smooth bump function that is positive in a compact time interval and zero outside this interval. This function starts from zero and smoothly reaches a finite maximum (positive) value in a finite time period, before smoothly decaying to zero in finite time. The finite time periods of rise and decay are the one-sided widths of this function. These widths on either side of the function can be equal or different. We call the left side of the bump function as a “smooth step-up" function and the right side of the bump function as a “smooth step-down" function. The function depicted in Fig. 2.1 has different widths on either side, and hence this bump function is asymmetrical.

Consider an i^{th} asymmetrical bump function $\phi_i : \mathbb{R} \to \mathbb{R}$ that is smooth (Fry and McManus, 2002; Loring, 2008) and compactly supported, given by

$$\phi_i(t) = \begin{cases} e^{\dfrac{-k_{l_i}\Delta t_i^2}{\sigma_{l_i}^2(\sigma_{l_i}^2 - \Delta t_i^2)}} & t \in (t_i - \sigma_{l_i}, t_i] \\ e^{\dfrac{-k_{r_i}\Delta t_i^2}{\sigma_{r_i}^2(\sigma_{r_i}^2 - \Delta t_i^2)}} & t \in (t_i, t_i + \sigma_{r_i}) \\ 0 & \text{elsewhere,} \end{cases} \tag{2.5}$$

where $\Delta t_i = t - t_i$, σ_{l_i} is the width of the left side of the bump function and σ_{r_i} is the width of the right side of the bump function. The k_{l_i} and k_{r_i} are the scalar control gains that control the steepness of the left and right side of the bump function respectively. The time instant t_i is the time when the rigid body reaches corresponding desired attitude waypoint R_{d_i}. The maximum value of this bump function is unity when $t = t_i$. The

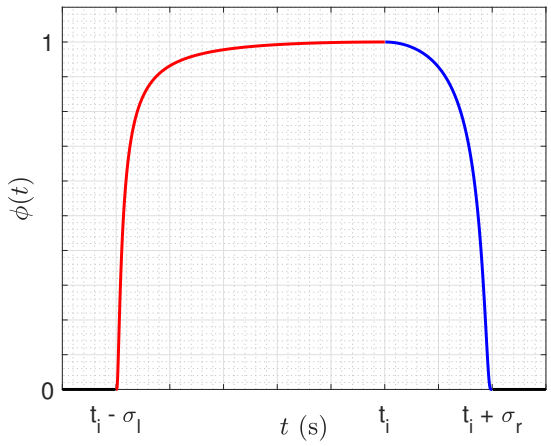

FIGURE 2.1: Asymmetric Bump Function

derivative of the left side of the asymmetric bump function is given by:

$$\dot{\phi_{l_i}}(t) = -2k_{l_i}\Delta t_i \left(\frac{1}{\sigma_{l_i}^2(\sigma_{l_i}^2 - \Delta t_i^2)} + \frac{\Delta t_i^2}{\sigma_{l_i}^2(\sigma_{l_i}^2 - \Delta t_i^2)^2} \right) e^{\frac{-k_{l_i}\Delta t_i^2}{\sigma_{l_i}^2(\sigma_{l_i}^2 - \Delta t_i^2)}}. \tag{2.6}$$

Note that $\dot{\phi_{l_i}}(t)$ is positive as $t - t_i$ is negative. Similarly the derivative of the right side of the bump function is given by:

$$\dot{\phi_{r_i}}(t) = -2k_{r_i}\Delta t_i \left(\frac{1}{\sigma_{r_i}^2(\sigma_{r_i}^2 - \Delta t_i^2)} + \frac{\Delta t_i^2}{\sigma_{r_i}^2(\sigma_{r_i}^2 - \Delta t_i^2)^2} \right) e^{\frac{-k_{r_i}\Delta t_i^2}{\sigma_{r_i}^2(\sigma_{r_i}^2 - \Delta t_i^2)}}, \tag{2.7}$$

and the derivative is negative since $t - t_i$ is positive in this case.

2.2.2 Smooth Step-Down Function for Initial Attitude

We use a “smooth step-down" function for the initial attitude at time $t = 0$, which starts at a constant value of 1 (for $t \leq 0$) and thereafter decays to 0 in finite time, as follows:

$$\phi_b(t) = \begin{cases} 1 & t \in (-\infty, 0) \\ e^{\frac{-k_b t^2}{\sigma_b^2(\sigma_b^2 - t^2)}} & t \in [0, \sigma_b), \end{cases} \tag{2.8}$$

where $t \in [0, \sigma_b)$ and σ_b is the width of this function. The derivative of this function (for $t \geq 0$) is,

$$\dot{\phi}_b(t) = -2k_b t \left(\frac{1}{\sigma_b^2(\sigma_b^2 - t^2)} + \frac{t^2}{\sigma_b^2(\sigma_b^2 - t^2)^2} \right) e^{\frac{-k_b t^2}{\sigma_b^2(\sigma_b^2 - t^2)}}. \tag{2.9}$$

2.2.3 Smooth Step-Up Function for Final Waypoint

The bump functions used to go through the intermediate attitude waypoints are “two-sided", i.e., they rise from 0 smoothly to a maximum value of 1 and then decay smoothly back to 0. But for the final waypoint we need only a “smooth step-up" function that starts with zero and rises to the maximum value of 1 and settles there. Consider the following function:

$$\phi_f(t) = \begin{cases} e^{\frac{-k_f \Delta t_f^2}{\sigma_f^2(\sigma_f^2 - \Delta t_f^2)}} & t \in (t_f - \sigma_f, t_f] \\ 1 & t \in (t_f, \infty), \end{cases} \tag{2.10}$$

where σ_f is the width of this function, k_f is the parameter to control the steepness of the function, t_f is the time when the rigid body reaches its final waypoint. The time derivative of this function, which is positive in the time interval $(t_f - \sigma_f, t_f)$, is given by:

$$\dot{\phi}_f(t) = -2k_f \Delta t_f \left(\frac{1}{\sigma_f^2(\sigma_f^2 - \Delta t_f^2)} + \frac{\Delta t_f^2}{\sigma_f^2(\sigma_f^2 - \Delta t_f^2)^2} \right) e^{\frac{-k_f \Delta t_f^2}{\sigma_f^2(\sigma_f^2 - \Delta t_f^2)}}. \tag{2.11}$$

2.2.4 Attractive Potential

We define the attitude tracking error for the i^{th} desired attitude waypoint as $Q_i = R_{d_i}^{\mathrm{T}} R(t)$ for $t \in [t_{i-1}, t_i]$. As the rigid body approaches the i^{th} desired attitude waypoint, the corresponding attitude error Q_i decays to zero. Once the attitude waypoint is achieved, the rigid body then again reorients itself to achieve the next waypoint. Thus, the rigid body passes through the series of reorientations. The attitude error thus goes to zero in piecewise manner. This continues to occur, till the rigid body achieves it's final attitude and then stabilizes. The attractive potential $AP(Q,t)\colon \mathrm{SO}(3) \times \mathbb{R}^+ \to \mathbb{R}^+$ is given by the following Morse function (Milnor, 1963),

$$AP_i(Q_i, t) = \langle K_i(t), I - Q_i \rangle, \tag{2.12}$$

where $K_i(t) = \phi_i(t) K_o$ and $K_o = \mathrm{diag}(K_1, K_2, K_3)$ and $\phi_i(t)$ is a bump function. The positive diagonal matrix K_o consists of control gain values $K_1, K_2, K_3 > 0$ and are unique. Representation of the attractive potential is given in Fig. 2.2. This value reaches its minimum value of zero as $Q_i \to I$.

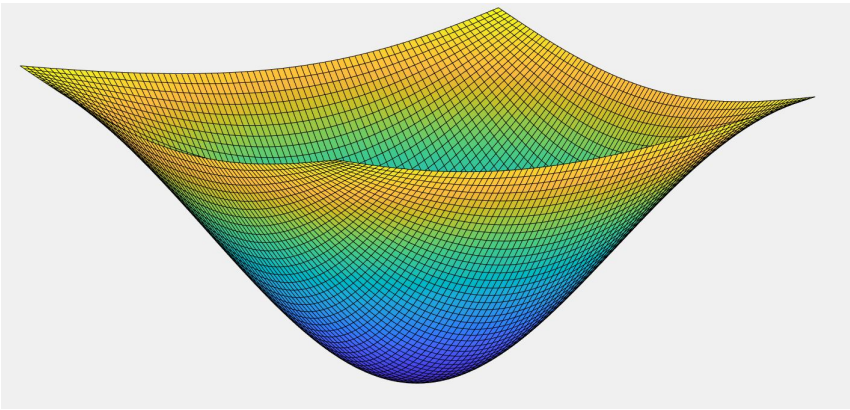

FIGURE 2.2: Attractive Potential

2.2.5 Repulsive Potential

The attractive potential is used to attract the rigid body to a desired attitude. Similarly, a repulsive potential (Kulumani and Lee, 2017) is used to avoid undesirable orientations. The rigid body should be able to avoid these undesirable attitudes at all times. Here, we assume that the undesirable attitudes are present at all times and are not changing. Hence, the function is not explicitly time-varying. This potential function has non-negative values ranging from zero to infinity as the rigid body approaches the undesirable orientation. The repulsive potential is an analytic function that is given by the following exponential function,

$$RP(R(t)) = e^{\frac{f}{\cos(\Psi) - r^T R^T v}} - 1, \tag{2.13}$$

where $r \in \mathbb{S}^2$ is the unit vector (in body frame) specifying the pointing direction of the sensor, and $v \in \mathbb{S}^2$ is the vector (in inertial frame) pointing towards an undesirable direction. The term $r^T R^T v$ specifies the angle between the sensor pointing direction and the direction vector to be avoided. The angle Ψ is the required minimum angular separation between them such that $\Psi \in (0, \pi/2)$. The positive constant f controls the shape of the function. The compact support of the repulsive potential (on $SO(3)$) decreases as the value of f decreases. This ensures that the effect due to the repulsive potential vanishes beyond the neighborhood of the minimum angular separation for the undesirable direction. We enforce the condition of zero exposure of the sensor to the undesirable zone. The above condition can be exercised with following constraint,

$$\cos(\Psi) - r^T R^T v > 0. \tag{2.14}$$

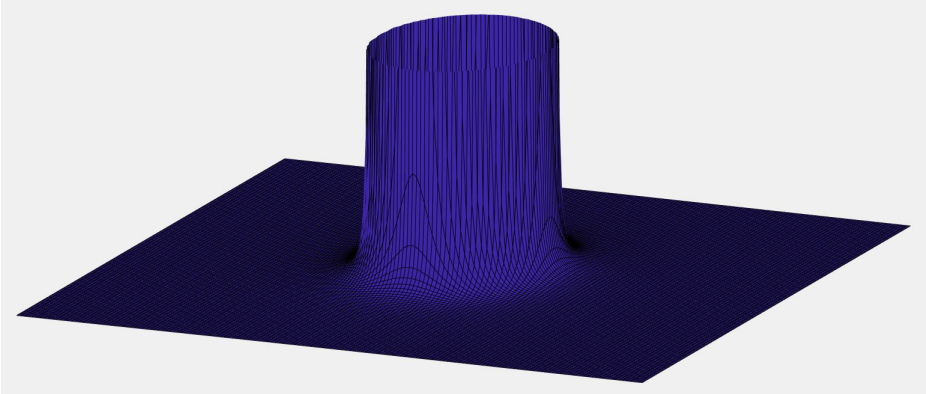

FIGURE 2.3: Repulsive Potential

The repulsive potential is illustrated in Fig. 2.3 .

2.2.6 The Potential Function

The potential function is the sum of attractive and repulsive potential functions. Let $R_{d_i} \in \mathrm{SO}(3)$ denote an intermediate desired attitude at time t_i. The potential function is given by:

$$U(Q_i, t) = \sum_{i=1}^{n} AP_i(Q_i, t) + RP(R(t)), \tag{2.15}$$

where $AP_i(Q_i, t)$ and $RP(R(t))$ are given by equations (2.12) and (2.13), respectively. The potential function is explicitly time-dependent. The attractive potential is $AP_i(Q_i, t) = 0$, when $Q_i = I$. Additionally, the bump function for a particular desired attitude waypoint is positive only in the respective time intervals. Outside those time intervals the attractive potential is not acting and equal to zero. Unlike the attractive potential, the repulsive potential is not time-varying and it is always acting. From the condition in equation (2.14), we see that the repulsive potential is always positive. Hence we can conclude that the potential function is a positive definite function at all times. The derivative of the

above potential function is given by:

$$\frac{d}{dt}U(Q_i,t) = \sum_i \frac{d}{dt}AP_i(Q_i,t) + \frac{d}{dt}RP(R(t)), \tag{2.16}$$

$$\frac{d}{dt}U(Q_i,t) = \sum_i (\langle \dot{K}_i(t), I - Q_i\rangle + S_{K(t)}(Q_i^{\mathrm{T}})\Omega) + \rho\cdot\Omega. \tag{2.17}$$

where ρ is given by

$$\rho = \left(\frac{-f(R^{\mathrm{T}}v)^{\times}r}{(\cos(\Psi) - r^{\mathrm{T}}R^{\mathrm{T}}v)^2} e^{\frac{f}{\cos(\Psi) - r^{\mathrm{T}}R^{\mathrm{T}}v}} \right), \tag{2.18}$$

$S_{K(t)}(Q_i) = \mathrm{vex}(K_i(t)Q_i - Q_i{}^{\mathrm{T}}K_i(t))$ and $\mathrm{vex}(\cdot)\colon \mathfrak{so}(3) \to \mathbb{R}^3$ is the inverse of the $(\cdot)^{\times}$ map.

2.2.7 Design of the Control Law

Theorem 2.2.1. *Consider the attitude kinematics and dynamics of a rigid body given by eqs. (2.1)-(2.3). Let t_i and R_{d_i} denote the sequences of time instants and desired attitude waypoints at these instants, as defined by (2.4), and let $Q_i(t) = R_{d_i}^{\mathrm{T}}R(t)$ for $t \in (t_{i-1}, t_i]$ be the attitude error, as defined earlier. Define*

$$L_0(t) = \begin{cases} \dot{\phi}_{i_l}(t) & \in (t_i - \sigma_{i_l}, t_i] \\ \dot{\phi}_f(t) & \in (t_f - \sigma_f, t_f] \\ 0 & \textit{elsewhere}, \end{cases} \tag{2.19}$$

where $\dot{\phi}_{i_l}$ and $\dot{\phi}_f$ are the derivatives of the smooth functions defined in equations (2.6) and (2.11) respectively. The time instants t_i and t_f are those at which the rigid body reaches the intermediate attitude waypoints and the final waypoint. Let $L(t)$ be the positive definite matrix such that $L(t) = L_0(t)I + J$, where $L_0(t)$ is positive semi-definite. Define the control law as

$$\tau_c = -S_{K(t)}(Q_i) - \rho - L(t)\Omega, \tag{2.20}$$

where ρ is as defined in (2.18), $S_{K_i(t)}(Q_i) = vex(K_i(t)Q_i - Q_i^{\mathrm{T}}K_i(t))$, and $vex(\cdot)\colon \mathfrak{so}(3) \to \mathbb{R}^3$ is the inverse of the $(\cdot)^{\times}$ map. The control law (2.20) then stabilizes the attitude dynamics of the rigid body to $(R, \Omega) = (R_f, 0)$.

Proof. Consider the following (candidate) Morse-Lyapunov function:

$$V(Q_i, \Omega, t) = \frac{1}{2}\Omega^{\mathrm{T}}J\Omega + U(Q_i, t), \tag{2.21}$$

defined piecewise on the time interval $(t_{i-1}, t_i]$. It can be seen that $V(Q_i, \Omega, t)$ is a positive definite function. Using equation (2.16) the derivative of the above Morse-Lyapunov function is given by:

$$\dot{V} = \Omega^{\mathrm{T}}J\dot{\Omega} + \frac{d}{dt}U(Q_i, t). \tag{2.22}$$

Using equation (2.3) we have the following:

$$\dot{V} = \Omega^{\mathrm{T}}\left(J\Omega \times \Omega + \tau_c + S_{K(t)}Q_i\right) + \rho \cdot \Omega + \dot{\phi}_i(t)\langle K_o, I - Q_i\rangle. \tag{2.23}$$

Substituting the control law from equation (2.20), we get,

$$\begin{aligned}\dot{V} &= -\Omega^{\mathrm{T}} L(t)\Omega + \dot{\phi}_i(t)\langle K_o, I - Q_i\rangle \\ &= -\Omega^{\mathrm{T}}(L_0(t)I + J)\Omega + \dot{\phi}_i(t)\langle K_o, I - Q_i\rangle.\end{aligned} \tag{2.24}$$

As the second term on the right hand side in the derivative of the Lyapunov function in eq. (4.34) is non-definite, it may need to be compensated by the negative first term. However, as this term is transient in nature, we design the $L_0(t)$ to mimic the increasing and decreasing portions of $\dot{\phi}_i(t)$ in order to compensate its effect over the time interval $(t_{i-1}, t_i]$.

When the rigid body approaches the final desired attitude, the attractive potential will have $\phi_f(t)$ as the "smooth step-up" function. As the derivative $\dot{\phi}_f(t)$ is positive, the term $\dot{\phi}_f(t)\langle K_o, I - Q_f\rangle$ will be positive in the time interval $(t_f - \sigma_f, t_f]$. So we design $L_0(t) = \dot{\phi}_f(t)$ to compensate for this effect during this transient time interval when $\dot{\phi}_f(t)$ is not zero. This ensures that the transient effects are mitigated and the attitude error $Q_f = I$ when $t = t_f$. For time is $t > t_f$, $\dot{\phi}_f(t)$ is zero. As a result, we get

$$\dot{V} = -\Omega^{\mathrm{T}} J\Omega \;\forall\, t > t_f. \tag{2.25}$$

Therefore, using the invariance principle on the state space $\mathrm{TSO}(3)$, we can conclude that (R, Ω) converges locally asymptotically to $(R_f, 0)$.

The attractive potential function has a global minimum value when $R = R_f$ and $t = t_f$. Thus, the global minimum is with respect to $R \in \mathrm{SO}(3)$ and $t \in \mathbb{R}_+$. The repulsive potential has a global maximum with respect to $R \in \mathrm{SO}(3)$ in the undesirable zone, i.e. in the region where $\Psi > \cos^{-1}(r^{\mathrm{T}} R^{\mathrm{T}} v)$. From the equation of repulsive potential (2.13),

we can conclude that when $r^{\mathrm{T}} R^{\mathrm{T}} v \to \cos(\Psi)$, then the potential function $U \to \infty$. As, the rigid body approaches towards the undesirable zone, the control torque generates large repulsive torques. Thus, the rigid body reorients itself away from the undesirable zone and towards the global minimum.

□

2.3 Numerical Simulation Results

This section gives some simulation results to demonstrate the potential function formulated in the earlier section. For the purpose of simulation one intermediate waypoint is considered.

2.3.1 Discretized Equations of Motion

For this simulation, the continuous dynamics and kinematics equations are replaced by the corresponding discretized equations of motion. A Lie group variational integrator (LGVI) is used for discretizing the continuous equations of motion. A LGVI preserves the structure of the configuration space, which in this case is the Lie group $\mathrm{SO}(3)$, without any parametrization or reprojection. Variational Integrators (Marsden and West, 2001) are a class of numerical integrators which conserve the momentum map and symplectic structure when the dynamics is almost conservative or fully conservative. The discrete equations of motion for Lie Group Variational Integrator scheme are given by (Nordkvist and Sanyal, 2010),

$$
\begin{aligned}
R_{k+1} &= R_k F_k, \\
J\Omega_{k+1} &= F_k^T J\Omega_k + h\tau_k,
\end{aligned}
\tag{2.26}
$$

where h is the fixed time step such that $h = t_{k+1} - t_k$, subscript k is the k^{th} time step of the simulation and $F_k \approx \exp(h\Omega_k^{\times}) \in \mathrm{SO}(3)$ guarantees that R_k evolves on $\mathrm{SO}(3)$.

2.3.2 Numerical Simulation

The proposed time-varying artificial potential scheme presented is simulated for a rigid body navigating around one undesirable zone towards its final orientation. This simulation has one intermediate and one final desired attitude waypoint. The simulation for the above scheme assumes the inertia matrix as $J = \mathrm{diag}(0.08, 0.15, 0.19)$ kgm^2. The direction of sensor in body-fixed frame is given by $r = [1, 0, 0]^{\mathrm{T}}$. The initial attitude is given by $R^o = \exp([0, 0, 150 \times (\pi/180)]^{\mathrm{T}})$ and the desired final attitude is $R^F = \exp([0, 0, 0]^{\mathrm{T}})$. Finally, $R^I = \exp([0, 0, 90 \times (\pi/180)]^{\mathrm{T}}) \times \exp([0, 7 \times (\pi/180), 0]^{\mathrm{T}})$ defines the one intermediate waypoint. The undesirable zone is located at $\exp([0, 0, 45 \times (\pi/180)]^{\mathrm{T}}) \times \exp([0, 10 \times (\pi/180), 0]^{\mathrm{T}})$. The minimum angular separation is $\Psi = 15^o$. The time step is $h = 0.01$s and the diagonal gain matrix is $K_o = \mathrm{diag}(0.05, 0.0095, 0.159)$.

The simulation begins at $t_0 = 0$s and ends at $t_E = 40$s. The rigid body reaches the intermediate waypoint at $t_1 = 15$s and the final waypoint at $t_f = 30$s. Once the rigid body achieves the desired final waypoint at $t_f = 30$s, the rigid body then maintains its final attitude. The bump function for this simulation and its corresponding derivative is shown in Fig. 2.4 The results of the numerical simulation are summarized in Fig. 2.5.

In Fig. 2.5a, at $t = 0$s the attitude tracking error plot shows the error between current attitude and first desired attitude waypoint. This error is almost zero when time

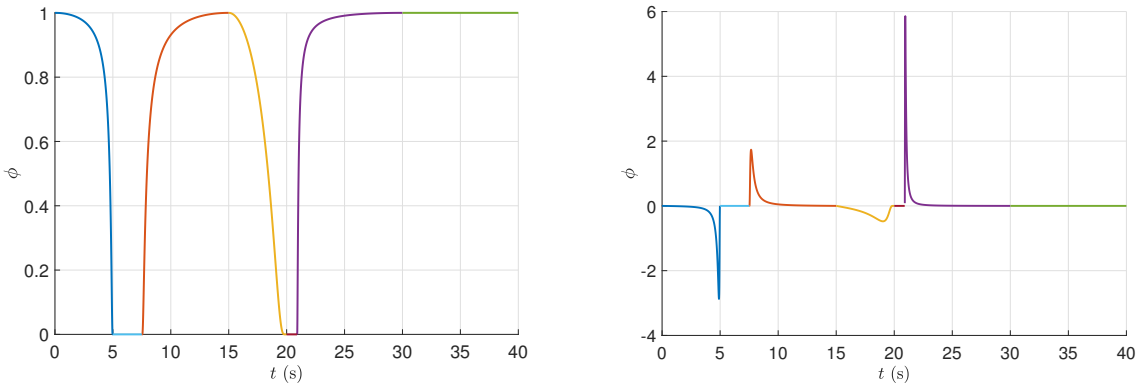

FIGURE 2.4: Bump function (left) and it's derivative (right).

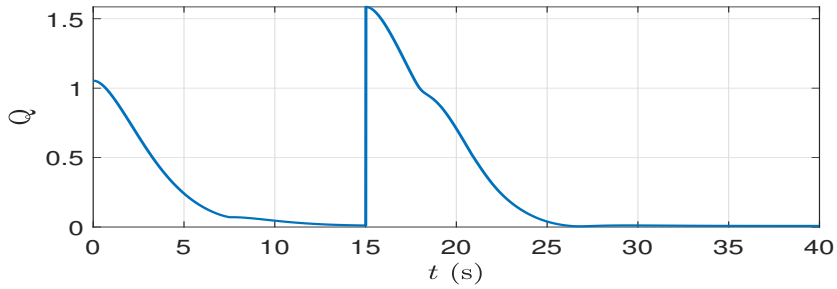

(A) Attitude Error

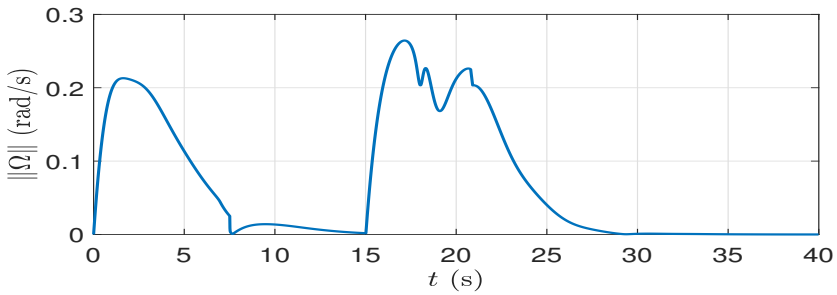

(B) Angular Velocities

approaches 15s as the rigid body moves closer to the desired intermediate attitude waypoint. After $t = 15$s the attitude error increases instantaneously to a finite value as the new desired attitude, which is the final desired attitude, becomes the new goal. Thus, the attitude error goes to zero in a piecewise manner as expected. At $t = 30$s, the rigid body

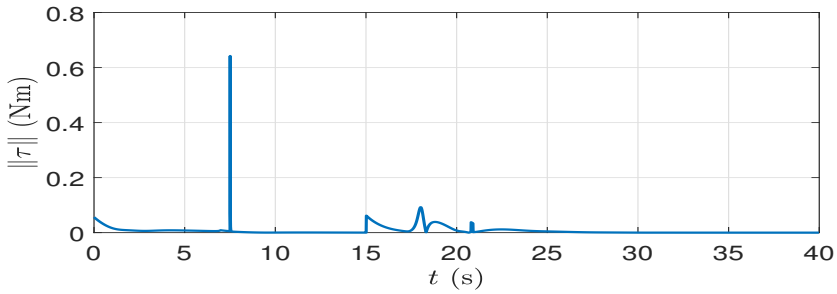

(C) Control torque

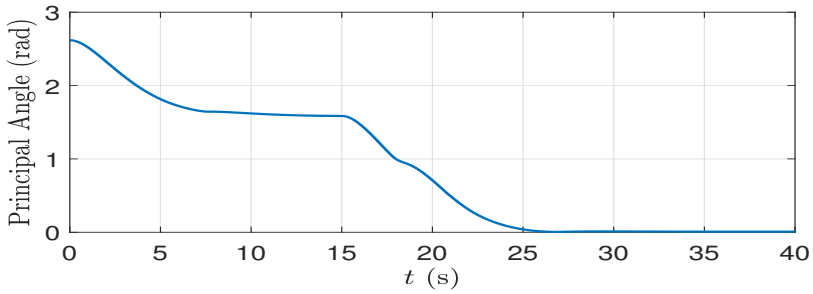

(D) Principal Angle

FIGURE 2.5: Simulation Results

achieves its final attitude and stabilizes there. The Fig. 2.6 shows the shows the pointing direction of the sensor in the inertial frame, which is represented as an unit vector on $\mathbb{S}^2$.

2.4 Conclusion

In this chapter, an integrated attitude guidance and tracking scheme that utilizes time-varying artificial potential functions is proposed. This continuous time scheme is designed directly on the configuration space of rigid-body attitude motion, $SO(3)$. The scheme can generate a desired attitude trajectory through multiple attitude waypoints and then track that desired trajectory through the waypoints. The guidance of the rigid

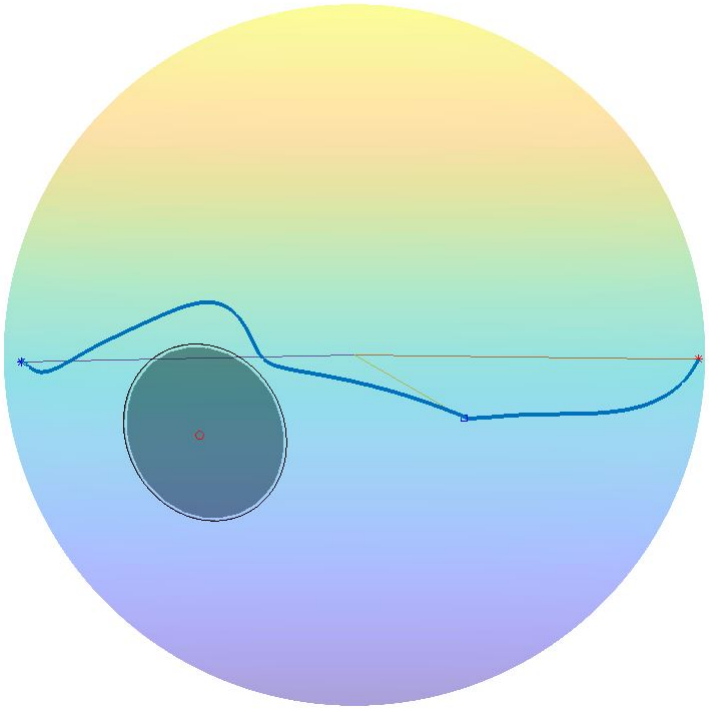

FIGURE 2.6: Trajectory of sensor fixed in body-frame

body is achieved by assigning attractive time-varying artificial potentials to desired attitude waypoints, while avoiding undesirable orientations using repulsive potentials. These attractive potentials are generated using asymmetric bump functions of time. A possible future research direction is to consider the full translational and rotational motion of rigid-bodies in $SE(3)$ and create an integrated guidance and control scheme for this full motion. Another research direction is to extend the above scheme to undesirable zones which are dynamic in nature.

Chapter 3

Attitude Pointing Control using Artificial Potentials with Control Input Constraints

This chapter presents a novel approach for pointing direction control of a rigid body with a body-fixed sensor, in the presence of control constraints and pointing direction constraints. This approach uses smooth artificial potentials and knowledge of maximum permissible angular velocities (or energy level) of the rigid body.

In 3.1, the attitude pointing control problem and required notation is introduced.

In 3.2, an attractive and repulsive artificial potential functions are introduced. This scheme relies on the use of artificial potentials where an attractive artificial potential is placed at the desired pointing direction and a repulsive artificial potential is used to avoid an undesirable pointing direction.

In 3.3, a control law is proposed which ensures almost global asymptotic convergence of the rigid body to its desired pointing direction, while satisfying the control input constraints and avoiding the undesirable pointing direction given in 3.4. Here, the control

parameters are designed such that the control input constraints are satisfied for the given system, and the corresponding control law.

These theoretical results are followed by numerical simulation results in 3.5, that provide an illustration of the scheme for a realistic spacecraft pointing control scenario.

3.1 Problem Definition

3.1.1 Coordinate Frame Definition

The configuration space of rigid body attitude motion is $\mathrm{SO}(3)$. The attitude is described by a rotation matrix relating a body-fixed coordinate frame to an inertial coordinate frame. We consider a coordinate frame $\mathcal{B}$ fixed to the body and another coordinate frame $\mathcal{I}$ that is fixed in space and takes the role of an inertial coordinate frame. Let $R(t) \in \mathrm{SO}(3)$ denote the time-varying rotation matrix for the rigid body rotating from body fixed frame $\mathcal{B}$ to inertial frame $\mathcal{I}$, where $\mathrm{SO}(3)$ denotes the group of all rotations in $\mathbb{R}^3$.

3.1.2 Rigid Body Reduced Attitude Description

Consider a rigid body (e.g. a space telescope) and its attitude dynamics. Let $p \in \mathbb{S}^2$ denote the desired pointing direction for the body fixed sensor in inertial frame. Then $\Gamma = R^{\mathrm{T}} p$ is the desired sensor pointing direction (reduced attitude) resolved in body frame. Without loss of generality, consider $e_1 = [1\ 0\ 0]^{\mathrm{T}} \in \mathbb{S}^2$ to be the boresight (pointing direction) vector of a sensor that is fixed in the body frame $\mathcal{B}$. Therefore, the pointing control objective is to rotate the body such that e_1 coincides with Γ.

Now denote by $v \in \mathbb{S}^2$ an undesirable pointing direction for the rigid body, expressed in inertial frame $\mathcal{I}$. The corresponding undesirable pointing direction resolved in the body frame is given by $\eta = R^{\mathrm{T}} v$. Therefore, the pointing exclusion zone objective is to ensure that e_1 avoids a prescribed exclusion zone around η. This exclusion zone is specified in terms of the angle between e_1 and η, which should be greater than a prescribed angle.

3.1.3 Attitude kinematics and Dynamics

Let $\Omega \in \mathbb{R}^3$ be the angular velocity of the rigid body expressed in body frame. The kinematics for the full attitude of the rigid body is given by

$$\dot{R} = R\Omega^{\times}, \tag{3.1}$$

where $(\cdot)^{\times} : \mathbb{R} \to \mathfrak{so}(3)$ is the skew-symmetric cross product operator and $\mathfrak{so}(3)$ is the Lie algebra of $\mathrm{SO}(3)$, identified with the linear space of 3×3 skew-symmetric matrices. Note that the cross-product operator is given by:

$$x^{\times} = \begin{bmatrix} x_1 \\ x_2 \\ x_3 \end{bmatrix}^{\times} = \begin{bmatrix} 0 & -x_3 & x_2 \\ x_3 & 0 & -x_1 \\ -x_2 & x_1 & 0 \end{bmatrix}. \tag{3.2}$$

The reduced attitude kinematics equation for the desired pointing direction can be

obtained by taking a time derivative of $\Gamma = R^{\mathrm{T}} p$, and substituting the full attitude kinematics (3.1). Using eq. (3.1), the reduced attitude kinematics equation is given by:

$$\dot{\Gamma} = \dot{R}^{\mathrm{T}} p = (R\Omega^{\times})^{\mathrm{T}} p = -\Omega^{\times}\Gamma = \Gamma^{\times}\Omega. \tag{3.3}$$

Similarly, the kinematics equation for the undesirable pointing direction can be obtained by taking a time derivative of both sides of the expression $\eta = R^{\mathrm{T}} v$, as follows:

$$\dot{\eta} = \dot{R}^{\mathrm{T}} v = (R\Omega^{\times})^{\mathrm{T}} v = -\Omega^{\times}\eta = \eta^{\times}\Omega. \tag{3.4}$$

The attitude dynamics of the system is modeled by

$$J\dot{\Omega} = -\Omega \times J\Omega + \tau_c, \tag{3.5}$$

where $J \in \mathbb{R}^{3\times 3}$ represents the positive definite inertia matrix of the rigid body defined in frame $\mathcal{B}$, and τ_c is the applied control input torque.

3.2 Artificial Potential

The main purpose of the artificial potential functions is to help the rigid body achieve its desired pointing direction while avoiding the undesirable pointing directions. This is enabled using the attractive and repulsive artificial potentials on $\mathbb{S}^2$ designed here.

3.2.1 Attractive artificial potential function

The body fixed sensor pointing vector on the rigid body is stabilized to the desired pointing direction using an attractive artificial potential. Consider the following attractive artificial potential for the desired pointing direction centered at Γ in frame $\mathcal{B}$:

$$U_a(\Gamma) = k_a(1 - e_1^{\mathrm{T}}\Gamma), \tag{3.6}$$

where $k_a > 0$ is the control gain value for the attractive function. From the above defining equation (3.6), we get the maximum and minimum value of the attractive potential function as:

$$\begin{cases} \max\{U_a(\Gamma)_{\Gamma\in\mathbb{S}^2}\} = 2k_a & (\text{when } \Gamma = -e_1), \\ \min\{U_a(\Gamma)_{\Gamma\in\mathbb{S}^2}\} = 0 & (\text{when } \Gamma = e_1). \end{cases} \tag{3.7}$$

Thus, this function is designed to be a positive definite function on $\mathbb{S}^2$ that has a maximum value when the sensor is pointing opposite to the desired pointing direction and a minimum value when it is pointing along the desired pointing direction. The time derivative of the above equation (3.6) is given by,

$$\dot{U}_a(\Gamma, \Omega) = -k_a e_1^{\mathrm{T}}\Gamma^{\times}\Omega. \tag{3.8}$$

3.2.2 Repulsive artificial potential function

Undesirable pointing directions can occur in rigid body pointing control applications, e.g., a star tracker sensor on a spacecraft should not be pointed directly towards the sun.

To avoid these undesirable directions, repulsive artificial potentials are designed. Consider the following smooth analytical bump function centered at η:

$$U_r(\eta) = \begin{cases} 0 & e_1^{\mathrm{T}}\eta \in [-1, \cos\Psi_0] \\ k_r e^{\frac{-b\beta(\eta)^2}{\gamma^2(\gamma^2-\beta(\eta)^2)}} & e_1^{\mathrm{T}}\eta \in [\cos\Psi_0, \cos\Psi] \\ k_r & e_1^{\mathrm{T}}\eta \in [\cos\Psi, 1] \end{cases} \tag{3.9}$$

where

$$\begin{aligned} \beta(\eta) &= e_1^{\mathrm{T}}\eta - \cos\Psi \\ \gamma &= \cos\Psi - \cos\Psi_0, \end{aligned} \tag{3.10}$$

$k_r > 0$ is a control gain value for the repulsive function and b determines the steepness of this function. The angle Ψ is the minimum required angular separation between the undesirable pointing direction and the sensor pointing direction. In the above function, angle Ψ traces an inner circular boundary. The region inside this boundary is restricted region for sensor pointing direction. The angle Ψ_0 describes the influence zone of this function. The representation of the repulsive potential function is given in Fig. 3.1. The function reaches a maximum value of k_r when $e_1^{\mathrm{T}}\eta = \cos\Psi$. As $e_1^{\mathrm{T}}\eta$ approaches the outer circle (i.e., $e_1^{\mathrm{T}}\eta = \cos\Psi_0$), the function decays to zero and remains zero outside the exclusion zone. The particular design of the repulsive potential in eq. (3.9) ensures that the function is smooth everywhere on $\mathbb{S}^2$.

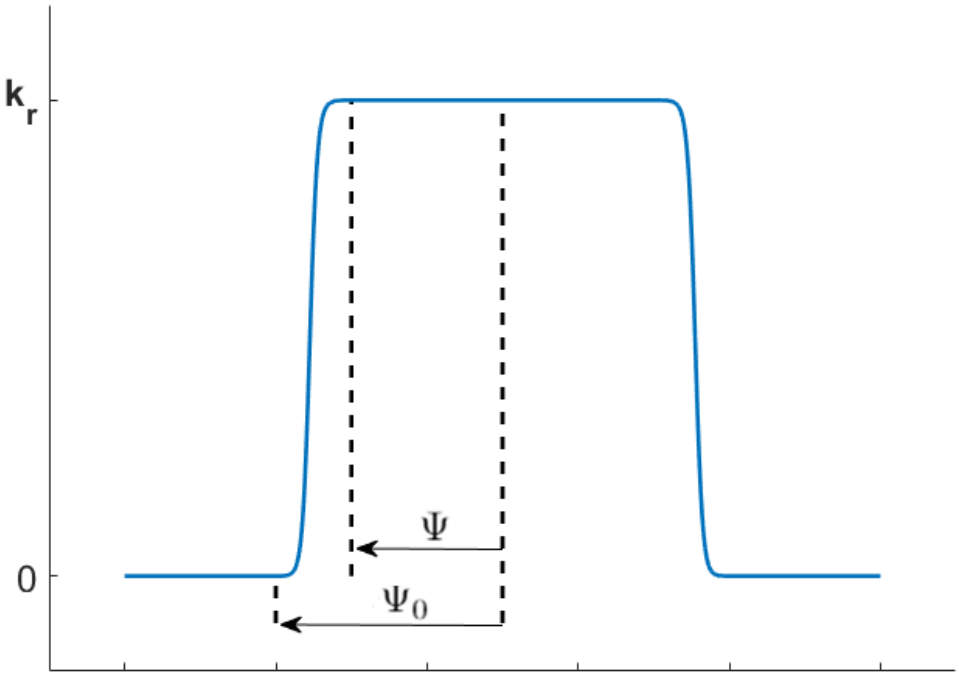

FIGURE 3.1: Representation of Repulsive potential Function

Therefore the permissible pointing directions for the body-fixed sensor is given by the set:

$$P_d = \{\Gamma \in \mathbb{S}^2 \mid \Gamma^{\mathrm{T}}\eta < \cos\Psi\}. \tag{3.11}$$

Note that $U_r(\eta)$ as defined by eq. (3.9) is continuous, and the value of $U_r(\eta) < k_r$ as long as the desired pointing direction is in the permissible set P_d. As a result, the value of this gain can be set to be the value of the initial value of a Lyapunov function that is decreasing along the dynamics of the feedback system.

The derivative of the above function is

$$\dot{U}_r(\eta, \Omega) = k_r \alpha(\eta) \Omega^{\mathrm{T}} e_1^{\times} \eta, \tag{3.12}$$

where $\alpha(\eta)$ is defined in a piecewise manner as

$$\alpha(\eta) = \begin{cases} 0 & e_1^{\mathrm{T}}\eta \in [-1, \cos\Psi_0] \\ \dfrac{-2b\beta(\eta)}{k_r\left(\gamma^2 - \beta(\eta)^2\right)^2} U_r(\eta) & e_1^{\mathrm{T}}\eta \in [\cos\Psi_0, \cos\Psi] \\ 0 & e_1^{\mathrm{T}}\eta \in [\cos\Psi, 1]. \end{cases} \tag{3.13}$$

3.3 Control Law

In this section, the control law that guarantees the convergence of the sensor pointing direction to the desired pointing direction is obtained. The Lyapunov stability analysis that ensures the *almost global* asymptotic stability of the desired pointing direction is also presented.

Theorem 3.3.1. *Consider the kinematics for the desired and undesired pointing directions given in* (3.3) *and* (3.4) *respectively, and the attitude dynamics equation given in* (3.5)*. Let* $L(t)$ *be a positive definite diagonal matrix. Define the attitude control law to be*

$$\tau_c = -L(t)\Omega + k_a e_1^{\times}\Gamma - k_r \alpha(\eta) e_1^{\times}\eta, \tag{3.14}$$

where $\alpha(\eta)$ *is defined in* (3.13)*. Further, let the desired pointing direction be outside the influence zone of the repulsive potential given by the angle* Ψ_0*. Then the proposed control law stabilizes the body-fixed sensor pointing direction to the desired pointing direction in an asymptotic manner, while avoiding the undesired direction.*

Proof. Consider the following candidate Morse-Lyapunov function,

$$V(\Gamma, \eta, \Omega) = \frac{1}{2}\Omega^{\mathrm{T}} J \Omega + U_a(\Gamma) + U_r(\eta) \tag{3.15}$$

The derivative of this Morse-Lyapunov function $\dot{V}(\Gamma, \eta, \Omega)$, substituting the equations (3.8), (3.12) and (3.13), is given by,

$$\dot{V}(\Gamma, \eta, \Omega) = \Omega^{\mathrm{T}} J \dot{\Omega} - k_a e_1^{\mathrm{T}} \Gamma^{\times} \Omega + k_r \alpha(\eta) \Omega^{\mathrm{T}} e_1^{\times} \eta.$$

Now substituting the attitude dynamics (3.5), this time derivative simplifies to:

$$\begin{aligned} \dot{V}(\Gamma, \eta, \Omega) &= \Omega^{\mathrm{T}} \left[J\Omega \times \Omega + \tau_c - k_a e_1^{\times}\Gamma + k_r \alpha(\eta) e_1^{\times}\eta \right] \\ &= \Omega^{\mathrm{T}} \left[\tau_c - k_a e_1^{\times}\Gamma + k_r \alpha(\eta) e_1^{\times}\eta \right]. \end{aligned} \tag{3.16}$$

Note that Ω and $J\Omega \times \Omega$ are orthogonal, and therefore the term $\Omega^{\mathrm{T}}[J\Omega \times \Omega]$ vanishes. After substitution of the control law (3.14) into eq. (3.16), $\dot{V}(\Gamma, \eta, \Omega)$ simplifies to:

$$\dot{V}(\Gamma, \eta, \Omega) = \dot{V}(\Omega) = -\Omega^{\mathrm{T}} L(t) \Omega. \tag{3.17}$$

Given that $L(t) = \mathrm{diag}([l_1(t), l_2(t), l_3(t)])$ where $l_i(t) > 0$ for $i = 1, 2, 3$, the above derivative of the Morse-Lyapunov function is strictly non-increasing. Therefore, $\dot{V}$ is negative semi-definite. Using LaSalle's invariance principle on $\mathrm{T}\mathbb{S}^2$, we conclude that the feedback system is asymptotically stabilized at the desired pointing direction if this direction is outside the zone of influence of the repulsive potential centered at the undesirable direction (in which case $\alpha(\eta) = 0$). Therefore, the body-fixed sensor pointing direction is stabilized to the desired pointing direction, and the given result follows. □

3.4 Control Constraints

This section provides a description of control constraints for the system that are achieved by designing certain control parameters. The design of these parameters ensure that the system stabilizes to the desired pointing direction, while satisfying the control constraints and avoiding the undesired direction.

3.4.1 Design of k_r

From equation (3.9), it is clear that the maximum value of the repulsive potential function is given by the control gain constant k_r. This maximum value occurs along the boundary

$e_1^{\mathrm{T}}\eta = \cos(\Phi)$. Now, consider a sub-level set of the state space given by,

$$V(\Gamma, \eta, \Omega) = \frac{1}{2}\Omega^{\mathrm{T}} J\Omega + U_a(\Gamma) + U_r(\eta) \leq V^{\max}. \tag{3.18}$$

The gain value k_r can be designed in a way such that the sub-level set given by equation (3.18) becomes invariant. Consider for example the following equations

$$k_r = V^{\max} = k_a(1 - e_1^{\mathrm{T}}\Gamma_I), \tag{3.19}$$

where $e_1^{\mathrm{T}}\Gamma_I$ gives the initial angular separation. The use of the criteria mentioned above points to the idea that the system will never have the required energy to violate the constraint.

Another noticeable fact is that outside of the exclusion zone we have $U_r(\eta) \equiv 0$, which implies that only the $\Omega^{\mathrm{T}} J\Omega$ and $U_a(\Gamma)$ terms govern the Lyapunov function (7.47).

3.4.2 Design of $L(t)$

Referring to equation (3.14), it can be deduced that the second and third term are orientation dependent and are bounded. Thus, the control constraints are satisfied by designing the control gain values $l_i(t)$ in the first term $-L(t)\Omega$. Rewriting the control torque equation (3.14) in the component form we get

$$\begin{Bmatrix} \tau_1 \\ \tau_2 \\ \tau_3 \end{Bmatrix} = \begin{Bmatrix} -l_1(t)\Omega_1 \\ -k_a\Gamma_3 + k_r\alpha(\eta)\eta_3 - l_2(t)\Omega_2 \\ k_a\Gamma_2 - k_r\alpha(\eta)\eta_2 - l_3(t)\Omega_3 \end{Bmatrix}. \tag{3.20}$$

We consider control torque constraints of the form:

$$-\tau_{i,min} \leq \tau_i \leq \tau_{i,max}, \tag{3.21}$$

where $\tau_{i,min}, \tau_{i,max} > 0$. Now consider the first component $l_1(t)$. From equation (3.21), the torque constraint for τ_1 can written as

$$-\tau_{1,min} \leq -l_1(t)\Omega_1 \leq \tau_{1,max}. \tag{3.22}$$

If we consider $\Omega_1 > 0$, then we have $l_1(t)\Omega_1(t) \leq \tau_{1,min}$ which leads to $l_1(t) \leq \frac{\tau_{1,min}}{\Omega_1(t)}$. And if $\Omega_1 > 0$ then $l_1(t)|\Omega_1(t)| \leq \tau_{1,max}$ which leads to $l_1(t) \leq \frac{\tau_{1,max}}{|\Omega_1(t)|}$. Therefore, the term $l_1(t)$ can be designed as follows

$$l_1(t) = \frac{\tau_{1,m}}{|\Omega_1(t)| + \epsilon_1}, \tag{3.23}$$

where $\tau_{1,m} = \min\{\tau_{1,min}, \tau_{1,max}\}$ and $\epsilon_1 > 0$ is a small positive number that can be considered a control gain parameter.

Now consider the $l_2(t)$. From (3.21), second component of torque τ_2 can be written as

$$k_a\Gamma_3 - k_r\alpha(\eta)\eta_3 + l_2(t)\Omega_2 \leq \tau_{2,min}$$
$$-k_a\Gamma_3 + k_r\alpha(\eta)\eta_3 - l_2(t)\Omega_2 \leq \tau_{2,max}.$$

If we consider $\Omega_2 > 0$ then we have

$$l_2(t) \leq \frac{\tau_{2,min} - k_a\Gamma_3 + k_r\alpha(\eta)\eta_3}{\Omega_2(t)}.$$

Likewise for $\Omega_2 < 0$

$$l_2(t) \leq \frac{\tau_{2,max} + k_a\Gamma_3 - k_r\alpha(\eta)\eta_3}{|\Omega_2(t)|}.$$

A conservative design of $l_2(t)$ therefore is of the form

$$l_2(t) = \frac{\tau_{2,m} - |k_a\Gamma_3 - k_r\alpha(\eta)\eta_3|}{|\Omega_2(t)| + \epsilon_2}, \tag{3.24}$$

where $\tau_{2,m} = \min\{\tau_{2,min}, \tau_{2,max}\}$ and $\epsilon_2 > 0$ is a small positive control gain parameter. Similarly $l_3(t)$ is also designed. From (3.21), third component of torque τ_3 is of the form

$$-k_a\Gamma_2 + k_r\alpha(\eta)\eta_2 + l_3(t)\Omega_3 \leq \tau_{3,min}$$
$$k_a\Gamma_2 - k_r\alpha(\eta)\eta_2 - l_3(t)\Omega_3 \leq \tau_{3,max}.$$

The design of $l_3(t)$ is given by

$$l_3(t) = \frac{\tau_{3,m} - |k_a\Gamma_2 - k_r\alpha(\eta)\eta_2|}{|\Omega_3(t)| + \epsilon_3}, \tag{3.25}$$

where $\tau_{3,m} = \min\{\tau_{3,min}, \tau_{3,max}\}$ and $\epsilon_3 > 0$ is a small positive control gain parameter. Thus equations (3.23), (3.24) and (3.25) give positive but time-varying gains with the assumption that $\tau_{i,m} > 0$. Since $l_1(t)$, $l_2(t)$, and $l_3(t)$ are positive, one can conclude from equations (3.24) and (3.25) it is evident that

$$\tau_{2,m} - |k_a\Gamma_3 - k_r\alpha(\eta)\eta_3| > 0 \text{ and}$$
$$\tau_{3,m} - |k_a\Gamma_2 - k_r\alpha(\eta)\eta_2| > 0. \tag{3.26}$$

This leads to a condition where the control parameters for attractive and repulsive potential function in equation (3.6) and (3.9) respectively should satisfy the relation

$$\tau_{i,m} > k_a + \alpha(\eta) k_r.$$

Using (3.13) the above equation can be written as

$$\tau_{i,m} - k_a > \frac{-2b\beta(\eta)}{\left(\gamma^2 - \beta(\eta)^2\right)^2} U_r(\eta). \tag{3.27}$$

A value of b can be obtained that satisfies the above relation.

3.5 Simulation Results

This section presents numerical simulation results for attitude pointing control using artificial potential fields. These simulation results are provided for a time period of $T = 40s$, and with time step size of $\Delta t = 0.01s$, to demonstrate the performance of the proposed pointing control scheme.

The initial conditions and other parameters used for this simulation are described here. The sensor pointing direction in the body-fixed frame is $e_1 = [1\ 0\ 0]^{\mathrm{T}}$. The initial attitude and angular velocity of the rigid body is given by $R = I$, and $\Omega_0 = [0\ 0\ 0]^{\mathrm{T}}$ in the body frame, respectively. The desired pointing direction in the inertial frame is $p = [-0.866\ 0\ 0.5]^{\mathrm{T}}$. The initial and final pointing directions are 150° apart. The undesirable pointing direction in the inertial frame is $v = [0\ 0.28\ 0.96]^{\mathrm{T}}$. The minimum required

angular separation between the sensor pointing direction and undesired pointing direction is $\Psi = 20^\circ$ and the influence zone for the repulsive potential begins at $\Psi_0 = 30^\circ$. The control torque limits are set to $\tau_{\max} = [2 \;\; 2 \;\; 2]^{\mathrm{T}}$ Nm and $-\tau_{\min} = [-2 \;\; -2 \;\; -2]^{\mathrm{T}}$ Nm. Based on eq. (3.27), the value of $b = 0.18$ is selected as appropriate. Also, the control gains for the angular velocity feedback are set to $\epsilon_1 = \epsilon_2 = \epsilon_3 = 0.5$.

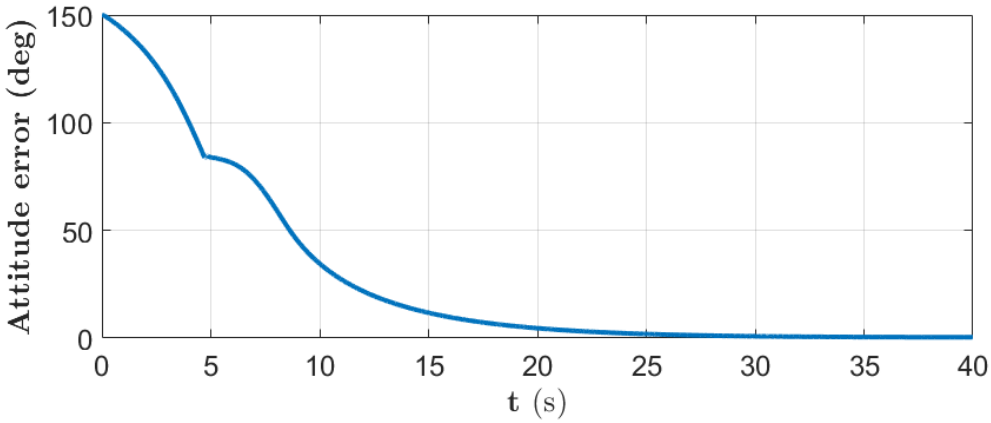

FIGURE 3.2: Attitude error in degrees

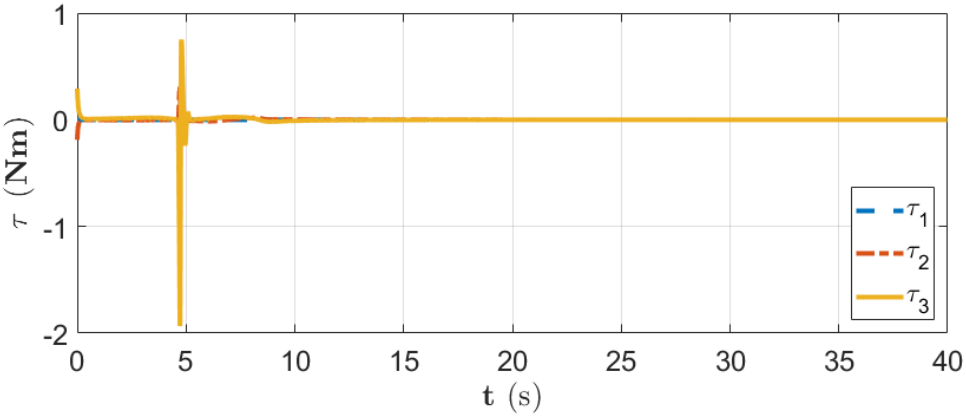

FIGURE 3.3: Torque

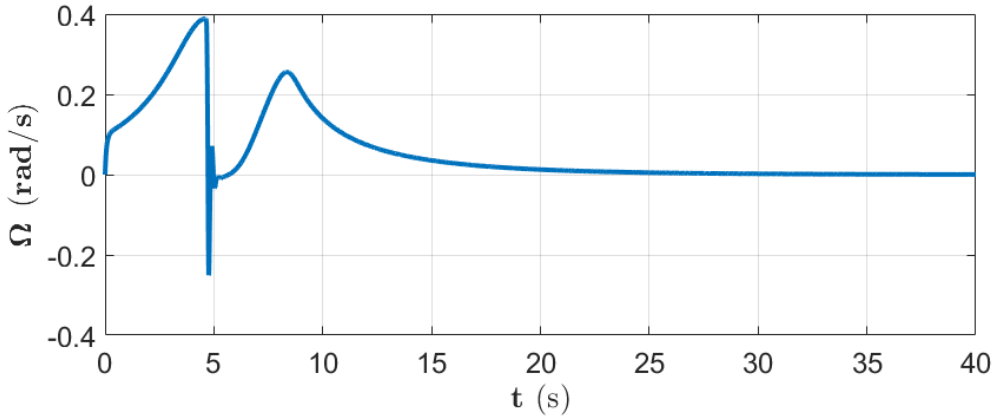

FIGURE 3.4: Angular Velocity

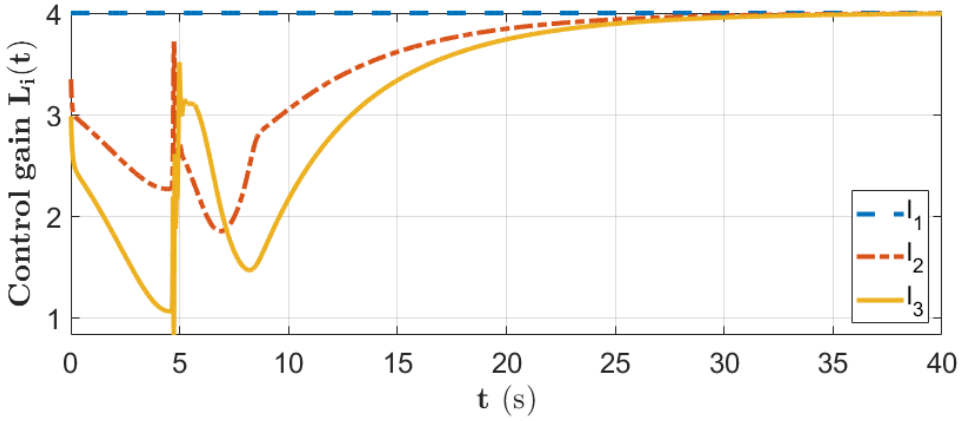

FIGURE 3.5: Control Gain Values

The results of the simulation are summarized as follows. The plot in Fig. 3.2 shows the reduced attitude error as the angular separation between current sensor pointing direction and desired pointing direction. From the parameters considered for this simulation, the initial angular separation between the sensor pointing direction and the desired pointing direction is 150°, as reflected in the plot. This error converges to zero asymptotically, as the sensor pointing direction converges to the desired direction. Plots of torque components in Fig. 3.3 show that the torque values are confined to the given upper and lower limits. Therefore, we see that this design of control gain parameters maintains the torque

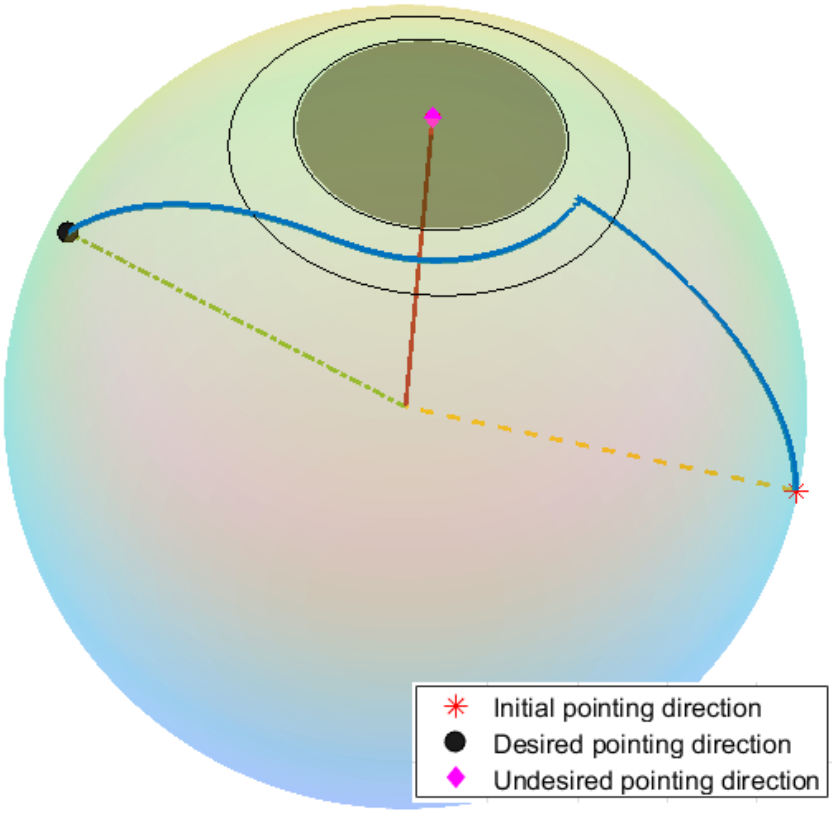

FIGURE 3.6: Trajectory traced by the sensor pointing direction as evolution of time

constraints. Except for the transients in torque values at approximately $t = 4.5$ s, the absolute values are well below the limits. The plots in Fig. 3.4 show the convergence of the angular velocities of the rigid body. Based on the theoretical development, the control gains l_1, l_2, and l_3 are designed so that they are positive, as shown in Fig. 3.5. The transients in the results at approximately $t = 4.5$ s occur when the sensor enters the influence zone of the repulsive potential and then changes direction to move away from it.

Fig. 3.6 shows the time evolution of the sensor pointing direction on S^2, as it orients itself to achieve the desired pointing direction. There is a shaded region inside the inner circular boundary which specifies the restricted zone for sensor pointing direction. The outer circular boundary indicates the beginning of the repulsive potential influence zone. The sensor pointing direction enters the repulsive potential influence zone but eventually moves away from it. The design of the control gain parameters will dictate how deep the sensor pointing direction will penetrate inside this influence zone, while the control constraints remain satisfied. The sensor then exits the influence zone to converge to the desired pointing direction.

3.6 Conclusion

This chapter presents a novel scheme for attitude pointing control and guidance of a rigid body with a body fixed sensor. The sensor has to avoid an exclusion zone around an undesirable pointing direction, and is subject to control torque constraints. This scheme relies on the use of an attractive artificial potential to guide the sensor to its desired pointing direction and a repulsive potential to avoid the undesirable pointing direction. A Lyapunov

stability analysis for the proposed control law guarantees almost global asymptotic stability of the sensor pointing direction at the desired pointing direction. The control parameters are designed so that they satisfy the control input and pointing direction exclusion zone constraints. Numerical simulations demonstrate the validity of this scheme. The results also show maintenance of the input torque constraints, as a result of the design of control gain parameters. Future research will consider pointing direction (reduced attitude) tracking of the body fixed sensor and techniques to make the control torque inputs less conservative.

Chapter 4

Integrated Guidance and Control of Driftless Control-affine Systems with Control Constraints and State Exclusion Zones

This chapter presents an integrated guidance and control scheme for autonomous control-affine systems with a convex and compact set of admissible control inputs including the origin (zero control), with convex exclusion zones to be avoided in the state space.

Section 4.1 describes the problem setup with the dynamic model for an autonomous, driftless, and control-affine system, along with assumptions on the state exclusion zones, target set in the state space to be reached, and control input constraints. This section also constructs barrier functions for the target set and exclusion zones in the state space, as well as the set of control inputs satisfying input constraints.

Section 4.2, describes the technical approach for our integrated guidance and control using an integral control barrier function. This section gives our barrier function designs

for each of the three requirements mentioned earlier: satisfying control input constraints, avoiding exclusion zones, and reaching a target set in the state space. In addition, the feedback system presented here is designed to converge in a stable manner to a target set that is compact, and in the safe region of the state space outside the exclusion zones. This technical approach is based on the newly developed method of integral control barrier functions. A smooth barrier function is designed such that the target set of states is a zero sublevel set of this function. To avoid the given exclusion zones in the state space, barrier functions with compact support are constructed with these exclusion zones as their zero superlevel sets. Finally, an integral control law is designed using a control barrier function that has the convex and compact set of admissible controls as its zero sublevel set. These components come together to provide an integral control barrier function for the feedback system. The resulting integrated guidance and control scheme ensures stable convergence of states to the desired safe set in the state space, while avoiding the unsafe exclusion zones in the state space and maintaining control input constraints.

The analytical development is followed by a set of numerical simulation results in section 4.3, which confirm the analytical findings. Here, the proposed integrated guidance and control scheme is applied to the kinematic car system.

4.1 System Model and Constraints

In this work, we design an integrated guidance and control scheme for driftless control-affine systems. The assumptions stated later in this section are reasonable, and cover several practical examples where this approach can be applied. This guidance and control approach leads to simultaneous satisfaction of state and control constraints.

4.1.1 System Model and Assumptions

Consider an autonomous and driftless control-affine system with state vector $x = [x_1 \ \dots \ x_n]^{\mathrm{T}} \in \mathbb{R}^n$ and the control input vector $u = [u_1 \ \dots \ u_m]^{\mathrm{T}} \in \mathbb{R}^m$. The system may be underactuated ($m < n$), fully actuated ($m = n$), or overactuated ($m > n$). The system dynamics is given by:

$$\dot{x} = \sum_{i=1}^{m} g_i(x)u_i = G(x)u, \tag{4.1}$$

where $g_i(x) \in \mathbb{R}^n$ for $i = 1, \dots, m$ are the control vector fields, and $G(x) = [g_1(x) \ \dots \ g_m(x)] \in \mathbb{R}^{n \times m}$. We consider the following integral control law for system (4.1)

$$\dot{u} = w, \tag{4.2}$$

where w is to be specified. An approach to design this integral control is given in Section 4.2.5.

In the remainder of this section, we describe the state and control constraints. We make two assumptions on the state constraints and one assumption on the set of constrained (admissible) controls, which are stated below.

Assumption 4.1.1. *The trajectories of the control-affine system (4.1) remain in a specified subset $\mathcal{X} \subset \mathbb{R}^n$. This set contains a target or goal set to be reached and exclusion zones to be avoided. Further, the target set and exclusion zones are ellipsoidal subsets of an ℓ-dimensional subspace of the state space, where $\ell \leq \min\{m, n\}$.*

Assumption 4.1.2. *The control influence matrix $G(x)$ is full ranked for all $x \in \mathbb{R}^n$. Further, the subspace consisting of the ℓ states that have constraints on them is controllable, available for*

feedback, and not invariant for the system (4.1).

Assumption 4.1.3. *The set of admissible control inputs is an ellipsoidal subset of* $\mathbb{R}^m$ *that is centered at the origin.*

The assumptions of ellipsoidal sets for target states, state exclusion zones, and the set of admissible control inputs keep the challenging problem of feedback guidance and control in the presence of state and control constraints tractable and are resonable in practical assumptions. Without loss of generality, under Assumption 4.1.1, we consider the state constraints applied only to the first ℓ states, which are denoted by $y \in \mathbb{R}^\ell$. The remaining states are denoted $z \in \mathbb{R}^{n-\ell}$, so that

$$x = \begin{bmatrix} y \\ z \end{bmatrix} \in \mathcal{X} \subset \mathbb{R}^n.$$

4.1.2 Target Set and Exclusion Zones in the State Space

The set of target states is assumed to be a subset of the state space that is defined and denoted as follows:

$$\begin{aligned} \mathcal{D} :=& \{y \in \mathbb{R}^\ell \mid \varepsilon \leq (y - \bar{y})^{\mathrm{T}} P_0^{-1} (y - \bar{y}) \leq 1\}, \\ & \text{where } 0 < \varepsilon < 1. \end{aligned} \tag{4.3}$$

Here $\bar{y} \in \mathbb{R}^l$ is a desired target state near which the system states should reach but not converge to, and $P_0 \in \mathbb{R}^{l \times l}$ is a (symmetric) positive definite matrix. This requires linear combinations of the states y to reach an ℓ-dimensional ellipsoidal set whose center is at $\bar{y} \in \mathbb{R}^\ell$, and where the outer ellipsoid's principal axes lengths and directions are given

by the square roots of the eigenvalues and the corresponding eigenvectors of P_0, respectively. The inner ellipsoid is concentric and co-axial with the outer one, with principal axes lengths given by the square roots of ε times the eigenvalues of P_0. Note that eq. (4.3) constrains the ℓ states in y but not the states z. An example application where a desired set like (4.3) is useful, is when a mobile robot needs to reach a bounded neighborhood of a target's position without colliding with it, but there are no such constraints on its final desired orientation and velocities. For ease of notation and later use, we define the following quantities:

$$\bar{\rho}(y) := P_0^{-1/2}(y - \bar{y}) \text{ and } \bar{r}(y) := \bar{\rho}(y)^{\mathrm{T}}\bar{\rho}(y), \tag{4.4}$$

so that:

$$\mathcal{D} = \{y \in \mathbb{R}^{\ell} \,|\, \varepsilon \leq \bar{r}(y) \leq 1\} \subset \mathcal{X}. \tag{4.5}$$

In (4.4), $P_0^{-1/2}$ denotes the primary (positive definite) square root matrix of P_0^{-1}, such that $P_0^{-1/2}P_0^{-1/2} = P_0^{-1}$.

In addition to reaching the target set, the control system must avoid specified exclusion zones within the state space. Such an exclusion zone may be required for obstacle or collision avoidance by a mobile robot, or to enforce a pointing direction restriction in spacecraft control. We consider a finite number k of exclusion zones, and characterize the ith exclusion zone centered at $y_i \in \mathbb{R}^{\ell}$ as follows:

$$\mathcal{E}_i := \{y \in \mathbb{R}^{\ell} \,|\, (y - y_i)^{\mathrm{T}} P_i^{-1}(y - y_i) \leq 1\}, \tag{4.6}$$

where $P_i \in \mathbb{R}^{\ell \times \ell}$ is a positive definite matrix. This accounts for the fact that the exclusion zone applies to only the y states but not the z states. As with the target set, we define the

following quantities for this exclusion zone:

$$\rho_i(y) := P_i^{-1/2}(y - y_i) \text{ and } r_i(y) := \rho_i(y)^{\mathrm{T}}\rho_i(y), \tag{4.7}$$

where $P_i^{-1/2}P_i^{-1/2} = P_i^{-1}$, so that:

$$\mathcal{E}_i = \{y \in \mathbb{R}^\ell \mid r_i(y) \leq 1\} \subset \mathcal{X}. \tag{4.8}$$

The time derivatives of the states that have constraints for the target set and exclusion zones, are given by:

$$\begin{aligned} &\dot{y} = G_y(x)u, \text{ where } G_y(x) = E_{\ell n}G(x), \\ &\text{and } E_{\ell n} = \begin{bmatrix} I_l & 0_{\ell,(n-\ell)} \end{bmatrix}. \end{aligned} \tag{4.9}$$

Here I_ℓ denotes the $\ell \times \ell$ identity matrix, and $0_{\ell,(n-\ell)}$ denotes the $\ell \times (n-\ell)$ matrix of zeros. As an example, eq. (4.6) can characterize an exclusion zone for the position of a mobile robot, but place no such restrictions on its orientation and velocity states. The admissible region of the state space is:

$$\Xi = \mathcal{X} \setminus \mathcal{E} \text{ where } \mathcal{E} = \bigcup_{i=1}^{k} \mathcal{E}_i, \tag{4.10}$$

and the $\mathcal{E}_i$ are defined as in (4.6). For a properly-posed control problem on Ξ, assumptions 4.1.1 and 4.1.2 should hold.

4.1.3 Set of Admissible Control Inputs

Assumption 4.1.3 applies to the set of control inputs. For ease of representation, we characterize this set as an ellipsoidal subset of $\mathbb{R}^m$ centered at the origin, as follows:

$$\mathcal{C} = \{u \in \mathbb{R}^m \mid u^{\mathrm{T}} Q^{-1} u \leq 1\}, \tag{4.11}$$

where $Q \in \mathbb{R}^{m \times m}$ is (symmetric) positive-definite. Unlike the desired set of target states in eq. (4.3) or exclusion zones for states as in eq. (4.6) which apply to only certain states, the control constraint set given by eq. (4.11) applies to all the control inputs.

As with the state constraints, we define the following quantities for this control constraint:

$$\sigma(u) := Q^{-1/2} u \text{ and } s(u) := \sigma(u)^{\mathrm{T}} \sigma(u). \tag{4.12}$$

Here $Q^{-1/2} \in \mathbb{R}^{m \times m}$ is the positive definite square root matrix $Q^{-1/2} Q^{-1/2} = Q^{-1}$, so that:

$$\mathcal{C} = \{u \in \mathbb{R}^m \mid s(u) \leq 1\}. \tag{4.13}$$

4.2 Controller Design

In this section, we develop our technical approach behind integrated guidance and control in the presence of simultaneous state and control constraints.

4.2.1 Barrier Functions for Exclusion Zones in State Space

Barrier functions are designed to enforce avoidance of the exclusion zones $\mathcal{E}_i$ given by eq. (4.6). Define

$$r_i := r_i(y) = (y - y_i)^{\mathrm{T}} P_i^{-1} (y - y_i), \tag{4.14}$$

where P_i and y_i are defined in eq. (4.6). A suitable barrier function is one that has $\mathcal{E}_i$ as a 0-superlevel set, as follows:

$$U(r_i) = \begin{cases} 0 & r_i \geq 1 + \varepsilon \\ k_r e^{\left(\frac{-b(r_i - 1)}{\varepsilon(\varepsilon - (r_i - 1))} \right)} & 1 < r_i < 1 + \varepsilon \\ k_r & r_i \leq 1 \end{cases} \tag{4.15}$$

where $U : \mathbb{R}_0^+ \to \mathbb{R}_0^+$, $b > 0$, $\varepsilon > 0$, $k_r > 0$ are parameters, and $i = 1, \ldots, k$. Here $\mathbb{R}_0^+$ denotes the set of non-negative real numbers. Note that this barrier function is a smooth bump function that has compact support in $r_i \in [0, 1 + \varepsilon]$ and is zero outside this interval.

The exclusion zone constraint (4.6) is enforced by the design of the function $U(r)$ through the appropriate selection of constant positive scalars b, ε, k_r. This is achieved by setting k_r to be slightly larger than the initial value of the overall integral control barrier function given in Section 4.2.5. The parameter ε gives an "influence zone" of this barrier function outside this exclusion zone, where trajectories of the system get repelled by this barrier, and is generally selected such that $0 < \varepsilon \ll 1$. The parameter b gives the decay rate of this function within this influence zone. From the above expression (4.15), we obtain the derivative of $U(r_i)$ with respect to r_i as:

$$U'(r_i) = \begin{cases} 0 & r_i \geq 1+\varepsilon \\ \dfrac{-b}{(\varepsilon - r_i + 1)^2} U_r(r_i) & 1 < r_i < 1+\varepsilon \\ 0 & r_i \leq 1. \end{cases} \tag{4.16}$$

Note that the composition $U \circ r_i : \mathbb{R}^n \to \mathbb{R}_0^+$ has compact support on $\mathbb{R}^n$. In addition, if ε is selected to be small enough, then it is guaranteed that

$$U(r_i)U(r_j) = 0 \text{ for } i \neq j,\ i, j \in \{1, \ldots, k\}, \tag{4.17}$$

where r_i is as defined by eq. (4.14).

With $U'(r_i)$ given by eq. (4.16), the time derivative of the barrier function $U(r_i)$ along the trajectories of system (4.1) is obtained as:

$$\begin{aligned} \dot{U}(r_i(x)) &= U'(r_i(x)) \mathcal{L}_{G_y(x)u} r_i(x) \\ &= 2U'(r_i(x))(y - y_i)^{\mathrm{T}} P_i^{-1} G_y(x) u, \end{aligned} \tag{4.18}$$

where $\mathcal{L}_{G_y(x)u} r_i(y)$ is the Lie derivative of $r_i(x)$ with respect to vector field $G_y(x)u$. Note that on the boundary of the exclusion zone $\mathcal{E}_i$, $r_i = 1$ and therefore $U'(r_i) = 0$, and $U'(r_i) < 0$ immediately outside this exclusion zone (for $1 < r_i < 1 + \varepsilon$), according to eqs. (4.15)-(4.16). Therefore, if the control scheme ensures that the term $(y - y_i)^{\mathrm{T}} P_i^{-1} G_y(x) u$ in eq. (4.18) is positive when $1 < r_i < 1 + \varepsilon$, then $\dot{U}(r_i(x)) < 0$ in this influence zone of this barrier function. This would ensure that if the initial state is outside this influence zone where $1 < r_i < 1 + \varepsilon$ and k_r is larger than the initial value of the overall integral barrier function, then the trajectories cannot enter $\mathcal{E}_i$.

4.2.2 Artificial Potential for Target Set in State Space

An artificial potential function that makes the target set given by eq. (4.3) attractive within the admissible region Ξ given by (4.10) is defined as

$$\bar{U}(\bar{r}) = (\bar{r} - 1)(\bar{r} - \varepsilon), \tag{4.19}$$

where $\bar{r}$ is set to $\bar{r}(x)$ defined in (4.4). Note that the target set $\mathcal{D}$ is a 0-sublevel set of $\bar{U} \circ \bar{r} : \Xi \to \mathbb{R}$. Therefore, this target set becomes attractive if the time derivative of $\bar{U}(\bar{r}(x))$ along the system (4.1) is negative for all $x = (y, z) \in \Xi \setminus \mathcal{D}$. This ensures that all trajectories starting in $\Xi \setminus \mathcal{D}$ approach $\mathcal{D}$ in a finite time interval.

The time derivative of this artificial potential function along the trajectories of system (4.1) is given by:

$$\dot{\bar{U}}(\bar{r}(x)) = \bar{U}'(\bar{r}(x)) \mathcal{L}_{G_y(x)u} \bar{r}(x). \tag{4.20}$$

Evaluating the right-hand side of the above equation, we get the following expression for this time derivative:

$$\dot{\bar{U}}(x, u) = 2\mu(\bar{r})(y - \bar{y})^{\mathrm{T}} P_0^{-1} G_y(x) u, \tag{4.21}$$

$$\text{where} \quad \mu(\bar{r}) = \bar{U}'(\bar{r}) = (\bar{r} - \varepsilon) + (\bar{r} - 1). \tag{4.22}$$

Note that $\mu(\bar{r})$ given by eq. (4.22) is bounded if $\bar{r}$ is bounded. Therefore, in the compact admissible region Ξ of the state space defined by eq. (4.10), the time derivative given by (4.21) can be unbounded only when the controls u are unbounded, given that $G(\cdot)$ is smooth.

4.2.3 Integral Barrier Function for Control Constraints

To enforce the control constraint given by eq. (4.11), an integral barrier function is designed along with an integral control law. For ease of notation, we use s to denote $s(u)$ defined in (4.12). Define the candidate barrier function:

$$W(s) = s - 1 - U(s), \tag{4.23}$$

where $U(s)$ is the bump function defined by (4.15). Note that the set $\mathcal{C}$ defined by eq. (4.11) is a 0-sublevel set of the barrier function $W(u)$ given by eq. (4.23) because $s \leq 1$ in $\mathcal{C}$.

The time derivative of this barrier function along the system trajectories is given by:

$$\begin{aligned} \dot{W} &= \nu(s)\mathcal{L}_w s = 2\nu(s)u^{\mathrm{T}}Q^{-1}w, \\ \text{where } \nu(s) &= 1 - U'(s), \end{aligned} \tag{4.24}$$

where $U'(s)$ is given by eq. (4.16) and Q is as defined in eq. (4.11). Note that $U(s) \geq 0$ for all s, and therefore $\mathcal{C}$ is a 0-sublevel set of $W(u)$. Also note that $\nu(s) > 0$ for all $s \in \mathbb{R}_0^+$ because $U'(s) \leq 0$. Therefore, $\mathcal{C}$ becomes an invariant set for the control input u if it is in $\mathcal{C}$ at some time instant, and the integral control w is designed to make the right side of eq. (4.24) non-positive. The following statement gives such an integral control law for w.

Proposition 4.2.1. *Let the initial control input $u(0) \in \mathcal{C}$. Then, the integral control law*

$$\begin{aligned} w = w_f &:= -QL(s, \bar{r}, r_i)u, \text{ where} \\ L(1, \bar{r}, r_i) &= L(1, \bar{r}, r_i)^T > 0, \end{aligned} \tag{4.25}$$

makes the admissible control set $\mathcal{C}$ forward invariant.

The proof of this statement follows by substituting w from eq. (4.25) into eq. (4.24), which shows that $\dot{W}(x,u) < 0$ with this integral control law at the boundary of $\mathcal{C}$, where $s(u) = 1$. Therefore, by Nagumo's theorem (Blanchini, 1999), the set $\mathcal{C}$ is forward invariant.

4.2.4 Local Minima Avoidance

Existence of local minima is an issue with artificial potential functions. A function that destabilizes local minima of the barrier function for the ith exclusion zone is:

$$U_s(r_i,\bar{r}) = \begin{cases} \dfrac{k}{\beta+\gamma}\Phi(r_i,\bar{r}) & r_i \in]1, 1+\varepsilon[\\ 0 & \text{otherwise,} \end{cases} \tag{4.26}$$

where

$$\begin{aligned} \Phi(r_i,\bar{r}) &= e^{\left(\frac{-\alpha r_s(x,r_i)}{\beta^2(\beta^2 - r_s(x,r_i))}\right)}, \\ r_s(x,r_i) &= v(x,r_i)^{\mathrm{T}} v(x,r_i), \\ v(x,r_i) &= \nabla U(x) + \nabla \bar{U}(r_i), \\ \nabla U(x) &= \mu(\bar{r}) G_y(x)^{\mathrm{T}} P_0^{-1}(y-\bar{y}), \\ \nabla \bar{U}(r_i) &= U'(r_i) G_y(x)^{\mathrm{T}} P_i^{-1}(y-y_i), \end{aligned} \tag{4.27}$$

and where $k > 0, \alpha > 0, \gamma > 0, \beta > 0$. The time derivative of this potential function along the trajectories of system (4.1) is given by,

$$\begin{aligned}\dot{U}_s(r_i,\bar{r}) &= U_s'(r_i,\bar{r})\mathcal{L}_{G_y(x)u}r_s(x,r_i)\\ &= 2U_s'(r_i,\bar{r})v(x,r_i)^{\mathrm{T}}H(x,r_i)G_y(x)u,\end{aligned} \tag{4.28}$$

where we have compactly represented the above expression by expressing $\dot{v}(x,r_i) = H(x,r_i)G_y(x)u$, which involves the Hessian $H(x,r_i)$ of $U(x)+\bar{U}(r_i)$.

4.2.5 Guidance and Control Scheme

This subsection provides the main result on our integrated guidance and control scheme, whereby the system (4.1) is guided towards the desired target set $\mathcal{D}$ in the state space, while avoiding the exclusion zones $\mathcal{E}_i$ and using admissible control inputs from the constrained control set $\mathcal{C}$. Most of the preliminary results are given in sections 4.2.2, 4.2.1, and 4.2.3. The main result on the control law now follows.

Theorem 4.2.1. *Let $U : \mathbb{R}_0^+ \to \mathbb{R}_0^+$ be defined according to eqs. (4.15). With w_f defined by (4.25), consider the control law for system (4.1), given by:*

$$\begin{aligned}w = w_f - Q\Big[&\mu(\bar{r})G_y^T(x)P_0^{-1}(y-\bar{y})\\ &+\sum_{i=1}^{k}\Big(U'(r_i)G_y^T(x)P_i^{-1}(y-y_i))\\ &+U_s'(r_i,\bar{r})G_y^T(x)H(x,r_i)v(x,r_i)\Big)\Big].\end{aligned} \tag{4.29}$$

For all initial states $x_0 = x(0) \in \Xi$ and initial controls $u_0 = u(0) \in \mathcal{C}$, state trajectories $x(t)$ of the feedback system consisting of (4.1)-(4.2) with the control law (4.29) remain in Ξ, while control trajectories $u(t)$ remain in the set of admissible controls $\mathcal{C}$. Further, $x(t) \cap \mathcal{E}_i = \emptyset$ for any $t \in \mathbb{R}_0^+$, i.e., the exclusion zones $\mathcal{E}_i$ are never entered.

Proof. We start this proof with the observation that the bump function $U(r)$ has a compact support in $\mathbb{R}_0^+$. We define the following barrier functions:

$$U(x) = \bar{U}(\bar{r}(x)) + \sum_{i=1}^{k} (U(r_i(x)) + U_s(r_i, \bar{r})), \tag{4.30}$$

$$V(x,u) = U(x) + W(s(u)), \tag{4.31}$$

noting that they are functions of only the states $y \in \mathbb{R}^\ell$ in the full state vector $x = (y,z) \in \mathbb{R}^n$. Also note that $V(x,u)$ has $\mathcal{D} \times \mathcal{C}$ as a 0-sublevel set, while the union of the (disjoint) exclusion zones $\mathcal{E}$ is a superlevel set where the value of this function is at least as large as k_r. The time derivative of $V(x,u)$ along the trajectories of the feedback system (4.1) and the control law (4.29), is given by:

$$\dot{U}(x,u) = \mathcal{L}_{G_y(x)u} U(x). \tag{4.32}$$

Substituting eqs. (4.21) and (4.18) into the right side of eq. (4.32), it follows that

$$\begin{aligned} \dot{U}(x,u) &= 2\mu(\bar{r}(x))(y-\bar{y})^{\mathrm{T}} P_0^{-1} G_y(x) u \\ &+ 2\sum_{i=1}^{k} \Big(U'(r_i(x))(y-y_i)^{\mathrm{T}} P_i^{-1} G_y(x) u \\ &+ U_s'(r_i,\bar{r}) v(x,r_i)^{\mathrm{T}} H(x,r_i) G_y(x) u \Big). \end{aligned} \tag{4.33}$$

Taking into account eq. (4.24) for the time derivative of $W(u)$, we see that:

$$\begin{aligned}\dot{V}(x,u,w) = 2\Big[&\nu(s)w^{\mathrm{T}}Q^{-1} + \Big(\mu(\bar{r})(y-\bar{y})^{\mathrm{T}}P_0^{-1} \\ &+ \sum_{i=1}^{k}\Big(U'(r_i(x))(y-y_i)^{\mathrm{T}}P_i^{-1} \\ &+ U_s'(r_i,\bar{r})v(x,r_i)^{\mathrm{T}}H(x,r_i)\Big)\Big)G_y(x)\Big]u.\end{aligned} \tag{4.34}$$

Substituting the control law (4.29) and (4.25) into the right hand side of (4.34), we obtain:

$$\dot{V}(x,u,w) = 2w_f^{\mathrm{T}}Q^{-1}u = -2u^{\mathrm{T}}L(s,\bar{r},r_i)u \leq 0. \tag{4.35}$$

This barrier function is positive and increasing in value only when the state x is inside an exclusion zone, and therefore, the state does not go into these zones if $x(0) \in \Xi$. This shows that the set of states and controls given by $\Xi \times \mathcal{C}$ remains invariant in forward time, if the initial state $x(0) \in \Xi$ and initial control $u(0) \in \mathcal{C}$. Moreover, because $V(x,u)$ has $\mathcal{D} \times \mathcal{C}$ as the only 0-sublevel set inside $\Xi \times \mathcal{C}$ with the boundary of this set as the 0-level set, the state-control pair (x,u) converges to this set. This proves the result. □

The above result shows that $\Xi \times \mathcal{C}$ remains a positively invariant set, but it does not show convergence of state trajectories to the desired set $\mathcal{D}$ in the state space. This is shown in the following result, as a corollary of Theorem 4.2.1.

Corollary 4.2.1. *For system (4.1), consider the feedback control law (4.29) with $L(s,\bar{r},r_i)$ positive definite for all $\bar{r} > \varepsilon$. Then state trajectories $x(t)$ of the feedback system converge to the interior of the desired set $\mathcal{D} \subset \Xi$, and $\mathcal{D} \times \mathcal{C}$ is positively invariant.*

Proof. The proof of this result follows immediately from eq. (4.35), which shows that

$\dot{V}(x,u,w) < 0$ unless $u = 0$, because $L(s,\bar{r},r_i)$ is positive definite. This makes the 0-sublevel set $\mathcal{D}\times\mathcal{C}$ attractive as long as the control input is acting. By Nagumo's theorem (Blanchini, 1999), the set of desired states and controls, $\mathcal{D}\times\mathcal{C}$, is positively invariant. Therefore, using LaSalle's invariance principle (Khalil, 2002), the state trajectories $x(t)$ converge to the interior of the desired set $\mathcal{D}\subset\Xi$. □

As an example, a suitable choice of $L(s,\bar{r},r_i)$ is given by:

$$L(s,\bar{r},r_i) = \left(\frac{\bar{r}-\varepsilon}{(s-1)^2+v^2} + \sum_{i=1}^{k} U(r_i)\right) I_m, \tag{4.36}$$

where $0 < v \ll 1$. Note that this choice of $L(s,\bar{r},r_i)$ satisfies the condition of Lemma 4.2.1 only for $r > \varepsilon$ as required by Corollary 4.2.1. which is good enough to transfer the system states to the target set $\mathcal{D}$ while maintaining the control constraint set $\mathcal{C}$.

4.3 Simulation Results

We apply the integrated guidance and control scheme designed in the previous section, to the Heisenberg system given in (Bloch, 2015).

4.3.1 Application of Integrated Guidance and Control to Heisenberg System

The Heisenberg system is given by the equations

$$\begin{aligned}\dot{x}_1 &= u_1,\\ \dot{x}_2 &= u_2,\\ \dot{x}_3 &= x_1 u_1 - x_2 u_2,\end{aligned} \tag{4.37}$$

which is an underactuated control-affine system that is appropriate for scheme developed in Section 4.2. We impose the exclusion zone constraints and target set requirement on the states $y = (x_1, x_2)$, so that:

$$G(x) = \begin{bmatrix} 1 & 0 & x_1 \\ 0 & 1 & -x_2 \end{bmatrix}^{\mathrm{T}} \text{ and } G_y(x) = \begin{bmatrix} 1 & 0 \\ 0 & 1 \end{bmatrix}. \tag{4.38}$$

This state x_3 denotes the yaw and is unconstrained. For the simulation results shown next, we impose two exclusion zones on the states $y \in \mathbb{R}^2$ as follows:

$$\begin{aligned} y_1 &= \begin{bmatrix} 2.5 \\ 0 \end{bmatrix}, \; P_1^{-1} = \begin{bmatrix} 1.1025 & 0 \\ 0 & 1.1025 \end{bmatrix}, \\ y_2 &= \begin{bmatrix} 5.6 \\ -0.5 \end{bmatrix}, \; P_2^{-1} = \begin{bmatrix} 1.5876 & 0.04 \\ 0.04 & 1.96 \end{bmatrix}. \end{aligned} \tag{4.39}$$

The target set of states is given by eqs. (4.4)-(4.5), with its center and size given by:

$$\bar{y} = \begin{bmatrix} 8.5 & 0 \end{bmatrix}^{\mathrm{T}}, \; P_0^{-1} = \mathrm{diag}(0.4, 0.4). \tag{4.40}$$

Finally, the control constraint set is given by eq. (4.11) with:

$$Q = \mathrm{diag}(0.9604, 1.1025) \tag{4.41}$$

4.3.2 Numerical Simulation of the Kinematic Car System

We use the control law (4.29), with w_f defined by eq. (4.25) and control gain $L(s, \bar{r}, r_i)$ given by eq. (4.36). The control gain parameters are selected as follows:

$$\varepsilon = 0.35,\ b = 2.6012,\ v = \varepsilon/5 = 0.07,\ \beta = 25,\ \gamma = 0.1$$

The remaining gain parameter is selected as $k_r = V_0 + 2\varepsilon$, where V_0 is the initial value of the integral control barrier function defined by eq. (4.31). This initial value which is based on initial states and initial control inputs is:

$$x(0) = \begin{bmatrix} 0.05 & 0 & 0 \end{bmatrix}^{\mathrm{T}},\ u(0) = \begin{bmatrix} -0.35 & 0.21 \end{bmatrix}^{\mathrm{T}}.$$

The plot in Fig. 4.1 denotes the time evolution of states $y = (x_1, x_2)$ and the plot in fig. 4.2 shows control input vector components with time for the Heisenberg system with the proposed scheme. While these plots do not show how the state exclusion zones and control constraints are met, these are shown in the trajectories depicted in Fig. 4.3 and 4.4.

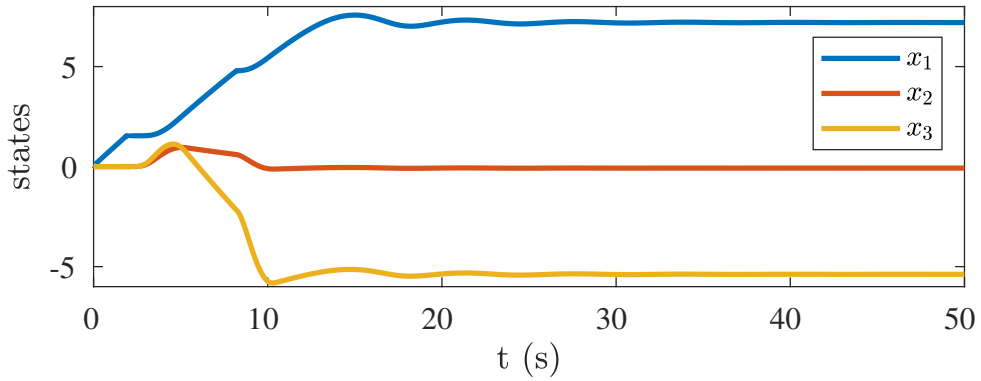

FIGURE 4.1: Plot of states with time

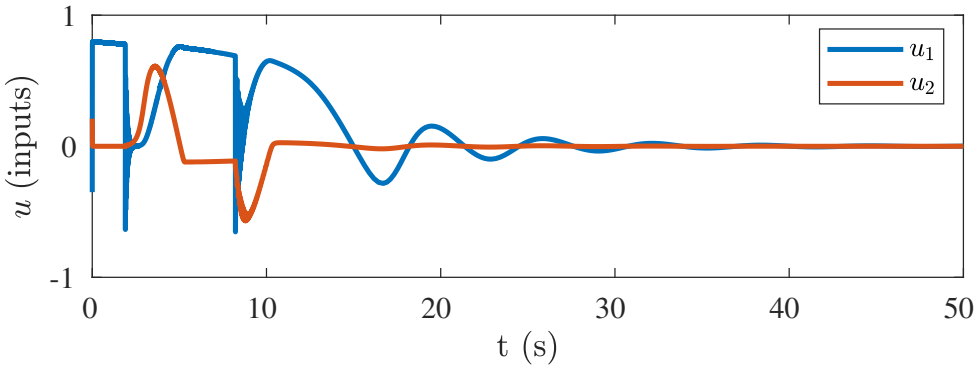

FIGURE 4.2: Control trajectory

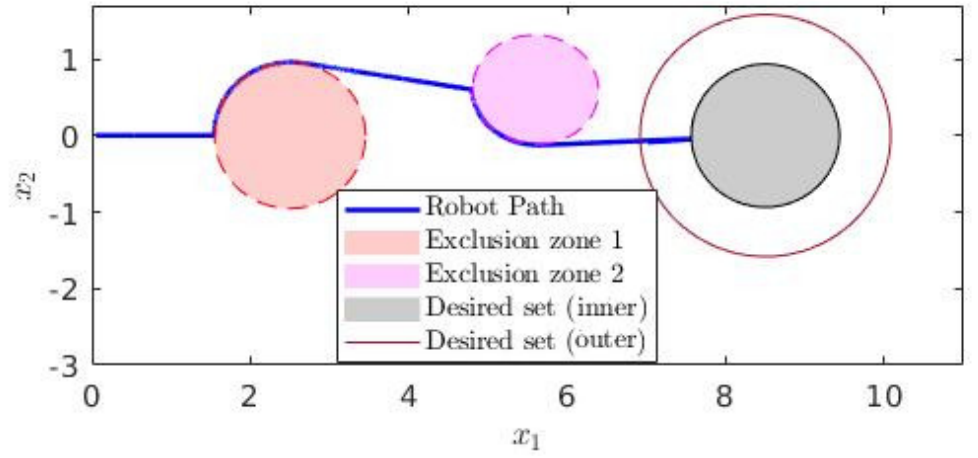

FIGURE 4.3: State trajectory

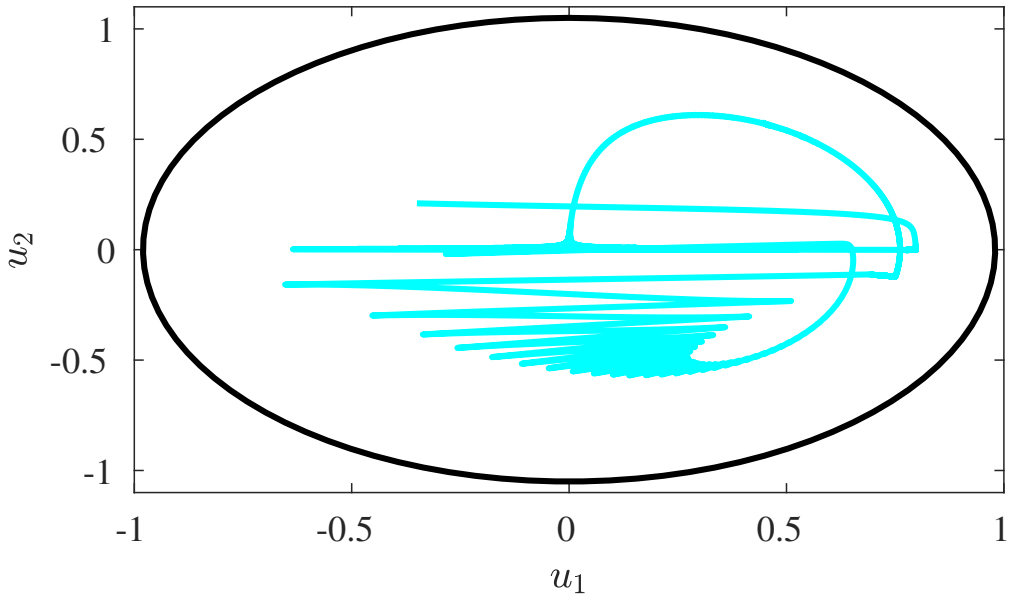

FIGURE 4.4: Control inputs trajectory

As shown in Fig. 4.3 and 4.4, the state exclusion zone constraints and control input constraints are maintained by this integrated guidance and control scheme. Additionally, the local minima destabilization term prevents from settling in local minima. Further, the state trajectory converges to within the inner and outer boundaries of the target set.

4.4 Conclusion

This chapter considered an application of a recently developed method of integral control barrier functions to guide a control-affine system along safe regions to a target zone, while avoiding unsafe regions and satisfying control constraints. We obtained an integrated guidance and control scheme that solves this problem for control-affine systems under certain assumptions. The comparison of the proposed approach with other approaches,

e.g., based on model predictive control and reference governors, will be addressed in future work.

Chapter 5

Discrete-time Control of Nonlinear Control-Affine Systems with Uncertain Dynamics

This chapter presents a novel approach to data-enabled control of discrete nonlinear control-affine systems with uncertain (“gray-box") dynamics.

The section 5.1 formulates our data-enabled control approach by outlining preliminary concepts and assumptions on the discrete-time system model for the data-enabled control approach.

The section 5.2 gives the gray-box ultra-local model representation of the nonlinear control-affine system in discrete time. The gray-box dynamics model accounts for known dynamics and lumps together the effects of disturbance inputs and poorly known dynamics into one time-varying unknown input, which is estimated in real time. This data-enabled approach leads to robust and stable real-time tracking control of desired output trajectories in the presence of model uncertainties. The lumped unknown input is estimated by a Hölder-continuous robustly stable learning scheme, using input-output

data in discrete time. This leads to finite-time convergence of the estimation errors of the unknown input to a bounded neighborhood of the zero vector, provided the system is Lipschitz-continuous with respect to states, inputs, outputs, and time.

The section 5.3 gives the nonlinear tracking control law for tracking a given (desired) output trajectory. The Lyapunov analysis is carried out to show the nonlinear stability and robustness of the uncertainty observer and tracking control law. This results in simultaneous real-time uncertainty estimation and tracking control.

The section 5.4 presents a set of numerical simulation results from the application of this data-enabled control scheme to an inverted pendulum on cart system with uncertain dynamics. This approach is also compared to the system with unknown dynamics.

5.1 Discrete Nonlinear System Description

In this section, we describe the discrete-time nonlinear system, its representation and related notation. Consider a discrete-time nonlinear system with m outputs and l inputs and n unknown (internal) states. The set of all real numbers is represented by $\mathbb{R}$, the set of all positive real numbers by $\mathbb{R}^+$, and the set of all non-negative reals by $\mathbb{R}_0^+$. The value of time-varying quantities at sampling instant $t_k \in \mathbb{R}_0^+$ is denoted by $(\cdot)_k = (\cdot)(t_k)$, with $u_k \in \mathbb{R}^l$ the control input vector, $y_k \in \mathbb{R}^m$ the vector of the measured output variables, and $z_k \in \mathbb{R}^n$ the vector of internal (unmeasured) states. Here, $k \in \mathbb{W} = \{0, 1, 2, \dots\}$, where $\mathbb{W}$ is the index set of whole numbers. The μth order forward difference of the output variable is defined by

$$y_k^\mu = y_{k+1}^{\mu-1} - y_k^{\mu-1} \quad \text{with } y_k^0 = y_k. \tag{5.1}$$

Let ν denote the relative degree of the input-output system. Then, the discrete-time uncertain nonlinear system can be represented by

$$y_{k+\nu} = f(y_k, y_{k+1}, \ldots, y_{k+\nu-1}, z_k, u_k, t_k), \tag{5.2}$$

where $f : (\mathbb{R}^m)^\nu \times \mathbb{R}^n \times \mathbb{R}^l \times \mathbb{R}_0^+ \to \mathbb{R}^m$ is uncertain and possibly time-varying. The control inputs u_k are designed to track the desired output trajectories $y_k^d = y^d(t_k)$. The following assumptions ensure that a given output trajectory can be tracked by the control inputs.

Assumption 5.1.1. *The discrete-time nonlinear system defined in* (5.2) *is Lipschitz continuous such that,*

$$\|y_{k+1} - y_k\| \leq L \|\chi_{k+1} - \chi_k\|, \tag{5.3}$$

where $\chi_k = (\varpi_k, u_k, t_k)$, $\varpi_k = (y_k, y_{k+1}, \ldots, y_{k+\nu-1}, z_k)$ *and* L *is a Lipschitz constant.*

Assumption 5.1.2. *The function* f *on the right side of eq.* (5.2) *can be represented as*

$$\begin{aligned} f(\chi_k) =& F_k + G_k u_k, \text{ where } F_k = F(\varpi_k, t_k) \\ & \text{and } G_k = G(\varpi_k), \end{aligned} \tag{5.4}$$

where $F = (\mathbb{R}^m)^\nu \times \mathbb{R}^n \times \mathbb{R}^l \times \mathbb{R}_0^+ \to \mathbb{R}^m$ *and* $G = (\mathbb{R}^m)^\nu \times \mathbb{R}^n \times \mathbb{R}^l \times \mathbb{R}_0^+ \to \mathbb{R}^{m \times l}$ *are Lipschitz continuous in their arguments.*

Note that the second assumption means that the nonlinear system is control-affine, with a control influence matrix that is not explicitly time-dependent.

5.2 Gray-box model and its estimation

This section describes a discrete-time model that models the nonlinear control-affine system (5.4) by a gray-box ultra-local model (ULM). This gray-box model is based on knowledge of part of the dynamics, while the unknown dynamics is represented as an additive uncertainty in the drift vector F_k. The unknown dynamics is then estimated from input-output data obtained over time. A first-order nonlinear observer is designed to estimate the unknown dynamics in this model.

5.2.1 Ultra-local model for uncertain systems

The concept of an ultra-local model that is local in input, output and time for SISO systems was proposed in Fliess and Join, 2013. This concept was generalized to discrete-time nonlinear systems with n inputs and m outputs with unknown dynamics in Sanyal, 2022. In this work, we further extend this concept to discrete-time nonlinear systems that have uncertainties but are control-affine as in eq. (5.4). The gray-box ULM that is used to model the system, is as follows:

$$y_{k+v} = \mathcal{F}_k + \bar{\mathcal{F}}_k + \bar{\mathcal{G}}_k u_k, \tag{5.5}$$

where $y_k \in \mathbb{R}^m$ is the vector of measured output variables as before, $\bar{\mathcal{F}}_k \in \mathbb{R}^m$ and $\bar{\mathcal{G}}_k \in \mathbb{R}^{m\times l}$ are known from a model that accounts for the known parts of the system dynamics, $\mathcal{F}_k \in \mathbb{R}^m$ represents the uncertainty in the dynamics which lumps together effects of imperfectly known internal parameters or states and external disturbance inputs, and $u_k \in \mathbb{R}^l$ is the control input vector. Note that the right sides of eqs. (5.4) and (6.1) have to be equal, although that does not necessarily mean that $\bar{\mathcal{F}}_k + \mathcal{F}_k = F_k$ or $\bar{\mathcal{G}}_k = G_k$. The latter would be true if the knowledge of the control influence matrix G_k is perfect.

In other words, the ultra-local model (6.1) is an *exact representation* of the discrete-time control-affine system (5.4) with unknown dynamics at each sampling instant; it is not an approximation. The uncertainty in the dynamics modeled by the gray-box ULM (6.1), satisfies the following assumptions.

Assumption 5.2.1. *The control gain matrix $\bar{\mathcal{G}}_k$ is a full-rank matrix with at least as many inputs as outputs ($m \leq l$).*

Assumption 5.2.2. *The known part of the dynamics represented by $\bar{\mathcal{F}}_k$ is Lipschitz-continuous such that,*

$$\left\|\bar{\mathcal{F}}_{k+1} - \bar{\mathcal{F}}_k\right\| \leq L_F \left\|\chi_{k+1} - \chi_k\right\|, \tag{5.6}$$

where L_F is a Lipschitz constant.

Here and in the sequel, $\|\cdot\|$ denotes the 2-norm unless specified otherwise. Note that assumptions 5.1.2 and 6.1.2 together imply that the unknown dynamics $\mathcal{F}_k$ is also Lipschitz continuous.

5.2.2 Estimation of unknowns in ultra-local model

A discrete-time first-order observer for the unknown dynamics $\mathcal{F}_k$ in (6.1) is given in Sanyal, 2022 and used in this work. Let $\hat{\mathcal{F}}_k$ be the estimate of the unknown $\mathcal{F}_k$, which is based on previously estimated values of $\mathcal{F}_i$ obtained from the measured outputs y_i for $i \in \{0, \ldots, k-1\}$. Define the estimation error:

$$e_k^{\mathcal{F}} := \hat{\mathcal{F}}_k - \mathcal{F}_k. \tag{5.7}$$

Based on the assumptions stated earlier, we know that the unknown dynamics $\mathcal{F}_k$ is bounded if the outputs, inputs and states are bounded. Now, we state the following results which are proved in Sanyal, 2022.

Proposition 5.2.1. Let the estimation error $e_k^{\mathcal{F}}$ be as defined in (6.3) and let $r \in]1,2[$ and $\lambda > 0$ be constants. Define the first order finite difference of the unknown dynamics $\mathcal{F}_k$ by

$$\Delta\mathcal{F}_k := \mathcal{F}_{k+1} - \mathcal{F}_k. \tag{5.8}$$

Let the system satisfy assumptions 5.1.1 through 6.1.2. Consider the nonlinear observer given by

$$\begin{aligned} \hat{\mathcal{F}}_{k+1} &= \mathcal{D}(e_k^{\mathcal{F}})e_k^{\mathcal{F}} + \mathcal{F}_k, \\ \text{where } \mathcal{D}(e_k^{\mathcal{F}}) &= \frac{((e_k^{\mathcal{F}})^{\mathrm{T}} e_k^{\mathcal{F}})^{1-1/r} - \lambda}{((e_k^{\mathcal{F}})^{\mathrm{T}} e_k^{\mathcal{F}})^{1-1/r} + \lambda}, \end{aligned} \tag{5.9}$$

and $\mathcal{F}_k = y_{k+v} - \bar{\mathcal{F}}_k - \bar{\mathcal{G}}_k u_k$ from (6.1). Then the estimation error $e_k^{\mathcal{F}}$ converges to a bounded neighborhood of $0 \in \mathbb{R}^n$ in finite time, where bounds on this neighborhood can be determined from bounds on $\Delta\mathcal{F}_k$.

The above result gives the form of the observer and its stability, for the unknown dynamics $\mathcal{F}_k$. The following result proved in Sanyal, 2022, gives the robustness of this observer.

Proposition 5.2.2. Consider the observer design in (6.5) for the unknown $\mathcal{F}_k$ in the ultra-local model (6.1). Let the first order difference $\Delta\mathcal{F}_k$ from (6.4) be bounded according to

$$\|\Delta\mathcal{F}_k\| \leq B^{\mathcal{F}}, \tag{5.10}$$

where $B^{\mathcal{F}} \in \mathbb{R}^+$ is a known constant. Then the observer error $e_k^{\mathcal{F}}$ converges to the neighbourhood given by

$$\mathcal{E} := \{e_k^{\mathcal{F}} \in \mathbb{R}^n \ : \ \sigma(e_k^{\mathcal{F}}) \left\| e_k^{\mathcal{F}} \right\| \leq B^{\mathcal{F}}\}, \tag{5.11}$$

for some finite $k > N$, $N \in \mathbb{W}$, where

$$\sigma(e_k^{\mathcal{F}}) := 1 + \mathcal{D}(e_k^{\mathcal{F}}). \tag{5.12}$$

Note that the above result gives ultimate bounds on the estimation error of the unknown dynamics (or disturbance) $\mathcal{F}_k$, where the bounds depend on its rate of change $\Delta\mathcal{F}_k$.

5.3 Tracking control law

In this section, a nonlinearly stable tracking control input u_k is designed based on the output y_k, a desired output y_k^d, uncertainty estimate $\hat{F}_k$ and known dynamics $\bar{F}_k$.

5.3.1 Output trajectory tracking control

Let $y^d : \mathbb{R} \to \mathbb{R}^m$ be the desired output trajectory which is ν times differentiable and let $y_k^d := y^d(t_k) \ \forall \ t_k \in \mathbb{R}_0^+$. The output trajectory tracking error is defined as:

$$e_k^y = y_k - y_k^d, \text{ where } \ y_k^d = y^d(t_k). \tag{5.13}$$

The following result gives the tracking control law to track the given desired trajectory.

Theorem 5.3.1. Consider the control-affine system (6.1) and the output trajectory tracking error defined by (5.13) for tracking a desired output trajectory. Let the desired output trajectory y_k^d and its first time difference $\Delta y_k^d = y_{k+1}^d - y_k^d$ be bounded. Consider the following tracking control law:

$$\begin{aligned} u_k &= \bar{\mathcal{G}}_k^{\#} w_k \text{ where } \bar{\mathcal{G}}_k^{\#} = \bar{\mathcal{G}}_k^{\mathrm{T}} \left(\bar{\mathcal{G}}_k \bar{\mathcal{G}}_k^{\mathrm{T}}\right)^{-1} \in \mathbb{R}^{l \times m}, \\ w_k &= y_{k+\nu}^d - \hat{\mathcal{F}}_k - \bar{\mathcal{F}}_k + \mathcal{C}(e_{k+\nu-1}^y) e_{k+\nu-1}^y, \\ \mathcal{C}(e_j^y) &= \frac{((e_j^y)^{\mathrm{T}} e_j^y)^{1-1/s} - \mu}{((e_j^y)^{\mathrm{T}} e_j^y)^{1-1/s} + \mu}, \end{aligned} \tag{5.14}$$

$s \in]1,2[$, $\mu > 0$, and $s < r$ and $\mu < \lambda$, where r and λ are as defined in Proposition 5.2.1. The control law (5.14) ensures that the tracking control error e_k^y and disturbance estimation error $e_k^{\mathcal{F}}$ satisfy the following error dynamics:

$$e_{k+\nu}^y + e_k^{\mathcal{F}} = \mathcal{C}(e_{k+\nu-1}^y) e_{k+\nu-1}^y. \tag{5.15}$$

In particular, if the uncertainty estimate $\hat{\mathcal{F}}^k$ is obtained from the observer law (6.5) of Proposition 5.2.1, then $e_{k+\nu}^y$ converges in a stable manner to a bounded neighborhood of $0 \in \mathbb{R}^m$ after finite time (i.e., for finite $k \in \mathbb{W}$).

Proof. Direct substitution of the control law (5.14) in the gray-box ULM (6.1) leads to:

$$\begin{aligned} e_{k+\nu} &= \mathcal{F}_k - \hat{\mathcal{F}}_k + \mathcal{C}(e_{k+\nu-1}^y) e_{k+\nu-1}^y \\ \Rightarrow e_{k+\nu} + e_k^{\mathcal{F}} &= \mathcal{C}(e_{k+\nu-1}^y) e_{k+\nu-1}^y. \end{aligned} \tag{5.16}$$

Now consider the error dynamics given by

$$e^y_{k+\nu} = \mathcal{C}(e^y_{k+\nu-1})e^y_{k+\nu-1}, \tag{5.17}$$

with $\mathcal{C}(e^y_j)$ defined as in eq. (5.14). Using a discrete-time Lyapunov stability analysis based on the Lyapunov function of the output tracking error defined by:

$$V^y_k = (e^y_k)^{\mathrm{T}} e^y_k, \tag{5.18}$$

we can easily show that the error dynamics (5.17) leads to finite-time stable convergence of the output tracking error e^y_k to zero. Therefore the error dynamics (5.16) is a perturbation of the "perfect" error dynamics (5.17) by the disturbance estimation error $e^{\mathcal{F}}_k$. The remainder of the proof of this result follows the proof of Theorem 4.1 and Proposition 4.2 of (Sanyal, 2022), and is omitted here for brevity. □

5.4 Numerical simulation results

This section provides simulation results of the proposed ULM-based data-enabled tracking control framework when it is applied to an inverted pendulum on a cart with nonlinear friction terms affecting the motion of both degrees of freedom. The dynamics model of this system is a "gray-box" (uncertain) dynamics model for the controller, which is described in §5.4.1. Numerical simulation results of this control scheme are given in §5.4.3. Additionally, this gray-box system is compared with the system with "black-box" (unknown) dynamics.

5.4.1 Inverted pendulum on cart system

The inverted pendulum on the cart is a mechanical system with two degrees of freedom. The cart's linear displacement x is considered positive when it is to the right of a fixed origin, while the angular displacement θ of the pendulum is considered positive counter-clockwise from the upward vertical, as shown in Fig. 5.1. The system has two inputs: a horizontal force F applied to the cart and a torque τ applied by the pendulum motor where it is attached to the cart. The states consist of the linear displacement, angular displacement, linear velocity and angular velocity. The outputs are the linear displacement x and the angular displacement θ. Therefore, this is a two-input and two-output system, unlike the usual single-input inverted pendulum on a cart example considered with only the horizontal cart force as an input. The pendulum has mass m, rotational inertia I and length $2l$, while the cart has mass M. Although the dynamics model of the system is an uncertain or gray box system for the purpose of control design, it is used to generate a desired output trajectory, which is then tracked using the proposed data-enabled control scheme.

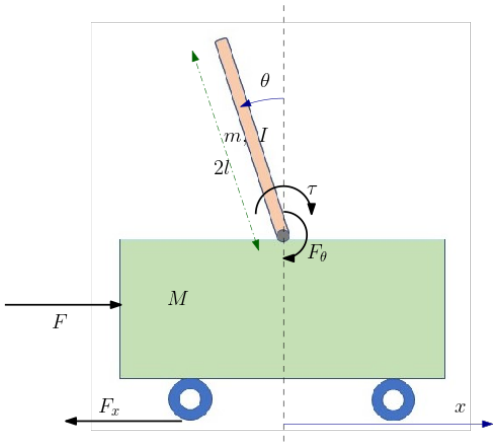

FIGURE 5.1: Inverted pendulum system to which our nonlinear model-free control framework is applied.

As unknown (disturbance) inputs, the inverted pendulum on a cart system is subjected to a nonlinear friction force acting on the cart's motion, and a nonlinear friction-induced torque acting on the pendulum. The friction force acting on the cart is denoted F_x and the friction torque acting on the pendulum is denoted F_θ, and they are given by:

$$\begin{aligned} F_x &= c_x \tanh \dot{x}, \\ F_\theta &= c_\theta \tanh \dot{\theta}. \end{aligned} \tag{5.19}$$

Note that the hyperbolic tangent function ensures that these frictional effects get saturated at high speeds ($\dot{x}$ and $\dot{\theta}$). Therefore, the dynamics model of this system, which is unknown for the purpose of control design, is given by:

$$\begin{aligned} &\mathcal{M}(q)\ddot{q} + \mathcal{D}(q,\dot{q}) = u,\ q = \begin{bmatrix} x \\ \theta \end{bmatrix}, \\ &\mathcal{M}(q) = \begin{bmatrix} M+m & -ml\cos\theta \\ -ml\cos\theta & I+ml^2 \end{bmatrix}, \\ &\mathcal{D}(q,\dot{q}) = \begin{bmatrix} ml\dot{\theta}^2\sin\theta + c_x \tanh\dot{x} \\ c_\theta \tanh\dot{\theta} - mgl\sin\theta \end{bmatrix}. \end{aligned} \tag{5.20}$$

The input and output vectors are:

$$u = \begin{bmatrix} F \\ \tau \end{bmatrix},\ y = q = \begin{bmatrix} x \\ \theta \end{bmatrix}. \tag{5.21}$$

For the purpose of the numerical simulation, the parameter values selected for this system are:

$$\begin{aligned} &M = 1.5\,\text{kg},\ m = 0.5\,\text{kg},\ l = 1.4\,\text{m},\ I = 0.84\,\text{kg}\,\text{m}^2, \\ &g = 9.8\,\text{m/s}^2,\ c_x = 0.028\,\text{N},\ c_\theta = 0.0032\,\text{N}\,\text{m}. \end{aligned} \tag{5.22}$$

The desired trajectory was generated by applying the following model-based control inputs (force and torque) to the cart and pendulum:

$$\begin{aligned} F = {} & ml\dot{\theta}^2 \sin\theta - 2(M + m\sin^2\theta)g\sin\theta \\ & - (M+m)g\sin\theta, \quad \tau = -mgl\sin\theta. \end{aligned} \tag{5.23}$$

This generates an output trajectory $y^d(t) = [x^d(t)\ \theta^d(t)]^{\mathrm{T}}$ that is oscillatory, as depicted in Fig. 5.2 in Section 5.4.3.

5.4.2 Discretization of continuous dynamics model

The dynamics model and control law for the inverted pendulum on cart system are given in Section 5.4.1, are discretized here using forward difference schemes for generalized velocities and accelerations of the two degrees of freedom. Denoting outputs and inputs in discrete time by $y_k := q_k = q(t_k)$ and $u_k := u(t_k)$ as before and the time step size by $\Delta t := t_{k+1} - t_k$, we get the following discretization of the continuous dynamics (5.20),

$$\begin{aligned} \frac{y_{k+2} - 2y_{k+1} + y_k}{\Delta t^2} = {} & \mathcal{M}_k^{-1}\Big(u_k - \mathcal{D}\big(y_k, \frac{y_{k+1} - y_k}{\Delta t}\big)\Big), \\ & \text{where } \mathcal{M}_k = \mathcal{M}(y_k), \end{aligned} \tag{5.24}$$

$\mathcal{M}(\cdot)$ and $\mathcal{D}(\cdot,\cdot)$ are as defined in eq. (5.20). This leads to the following second-order discrete-time system:

$$\begin{aligned} &y_{k+2} = \mathsf{F}_k + \mathsf{G}_k u_k, \text{ where } \mathsf{G}_k = \Delta t^2 \mathcal{M}_k^{-1} \text{ and} \\ &\mathsf{F}_k = 2y_{k+1} - y_k - \Delta t^2 \mathcal{M}_k^{-1} \mathcal{D}\big(y_k, \frac{y_{k+1} - y_k}{\Delta t}\big), \end{aligned} \tag{5.25}$$

where F_k and G_k have the meanings as defined by eq. (5.4). The known part of the dynamics can be represented as:

$$\bar{\mathcal{F}}_k = 2y_{k+1} - y_k - \mathcal{M}_k^{-1} \begin{bmatrix} ml(\theta_{k+1} - \theta_k)^2 \sin\theta_k \\ -mgl\Delta t^2 \sin\theta_k \end{bmatrix}. \tag{5.26}$$

In the numerical simulation results shown in the next subsection, this discrete-time model is used for generating the desired output trajectory starting from a given initial state vector and with the control laws given by eqs. (5.23) sampled at time instants t_k with velocities approximated by forward differencing (i.e., $\dot{y}(t_k) \approx \frac{y_{k+1}-y_k}{\Delta t}$). It is then used to simulate the performance of the data-enabled control approach outlined in Sections 5.2 and 5.3 with the discrete dynamics (5.25), with the friction force and friction torque unknown to the control law.

5.4.3 Simulation results for control scheme

The numerical simulation results for the model-free tracking control scheme applied to the system described by eqs. (5.20)-(5.22) are presented here. A trajectory is generated for this system using the control scheme (5.23) sampled in discrete time, with the initial

states:

$$\begin{bmatrix} q^d(0) \\ \dot{q}^d(0) \end{bmatrix} = \begin{bmatrix} x^d(0) \\ \theta^d(0) \\ \dot{x}^d(0) \\ \dot{\theta}^d(0) \end{bmatrix} = \begin{bmatrix} 0.45\,\text{m} \\ -0.14\,\text{rad} \\ -0.3\,\text{m/s} \\ 0.05\,\text{rad/s} \end{bmatrix}. \tag{5.27}$$

The desired trajectory $y^d(t) = [x(t)^d \;\; \theta^d(t)]^{\mathrm{T}}$ for a time interval of $T = 50$ seconds is plotted in Fig. 5.2.

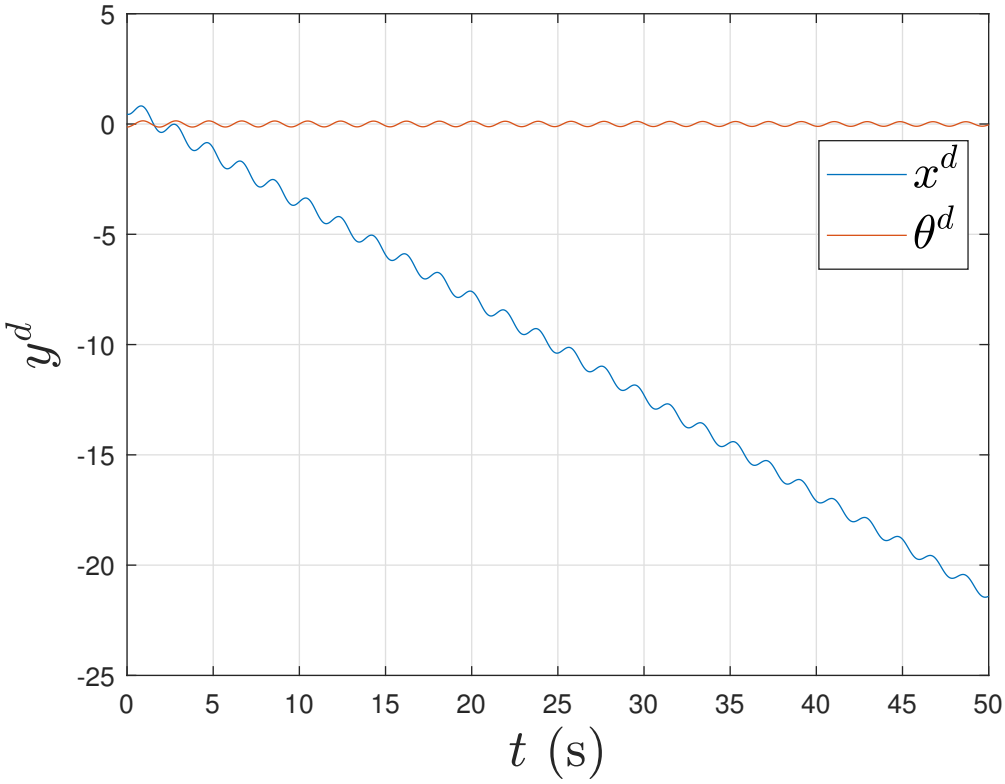

FIGURE 5.2: Desired trajectory generated for $T = 50$ seconds for inverted pendulum on cart system.

The control scheme given by Theorem 5.3.1 is applied to this system to track this desired trajectory. For this simulation, the initial state estimates are selected as follows:

$$\begin{bmatrix} \hat{q}(0) \\ \dot{\hat{q}}(0) \end{bmatrix} = \begin{bmatrix} \hat{x}(0) \\ \hat{\theta}(0) \\ \dot{\hat{x}}(0) \\ \dot{\hat{\theta}}(0) \end{bmatrix} = \begin{bmatrix} 0\,\text{m} \\ 0.102\,\text{rad} \\ 0\,\text{m/s} \\ 0\,\text{rad/s} \end{bmatrix}. \tag{5.28}$$

Output measurements are assumed at a constant rate of 50 Hz, i.e., sampling period $\Delta t = 0.02$ s. In the simulation, the measurements are generated by numerically propagating the true discrete-time dynamics of the inverted pendulum on the cart system given by eqs. (5.25), and adding noise to the true outputs $y_k = q_k$. The additive noise is generated as high frequency and low amplitude sinusoidal signals, where the frequencies are also sinusoidally time-varying. A finite-time stable output observer given by:

$$\begin{aligned} &\hat{y}_{k+1} = y_{k+1} + \mathcal{B}(e_k^o)e_k^o, \text{ where } e_k^o = \hat{y}_k - y_k, \\ &\text{and } \mathcal{B}(e_k^o) = \frac{\left((e_k^o)^{\mathrm{T}} L e_k^o\right)^{1-1/p} - \beta}{\left((e_k^o)^{\mathrm{T}} L e_k^o\right)^{1-1/p} + \beta}. \end{aligned} \tag{5.29}$$

with the observer gains:

$$L = 0.1, \;\; \beta = 2, \;\; \text{and} \;\; p = \frac{13}{11}, \tag{5.30}$$

is used to filter out noise from the measured outputs. The following observer gains for the first order ultra-local model observer defined by Proposition 5.2.1, are used:

$$\lambda = 0.35, \;\; \text{and} \;\; r = \frac{9}{7}. \tag{5.31}$$

The tracking controller of Theorem 5.3.1 with the following gains are used in this simulation:

$$s = \frac{11}{9},\ \mu = 20.935,\ \text{and}\ \mathcal{G}_k = \Delta t \begin{bmatrix} 0.559 & 0.196 \\ 0.196 & 0.657 \end{bmatrix}, \tag{5.32}$$

where $\mathcal{G}_k$ is selected to be symmetric and positive definite, as expected for a mechanical system.

The comparison plot for the estimation error in estimating the uncertainty in the model $\mathcal{F}_k$ according to the observer given by Proposition 5.2.1, is given in Fig. 5.3. The initial transients in the model estimation error for the gray-box system is much less as compared to the black-box system, as the gray-box system benefits from the partial knowledge of the dynamics. In addition, as the model estimation error converges and settles within the bounds given by Proposition 5.2.2, the model estimation error for gray-box system has less oscillations as compared to the black-box system. Simulation results for the output trajectory tracking errors, is given in the 5.4. After brief initial transients, the tracking errors for cart position and pendulum angle settle within 6 mm and 0.003 rad, respectively. The output trajectory tracking performance is greatly improved for the gray-box system as compared to the black-box system.

The plots in Fig. 5.5 shows the comparison of control inputs using the control law in eq. (5.14) between the black-box and gray-box systems. These control input profiles show some oscillations in tracking the desired trajectory, that correlate with the oscillations seen in the ultra-local model observer error in Fig. 5.3. These oscillations are comparatively more for the black-box system.

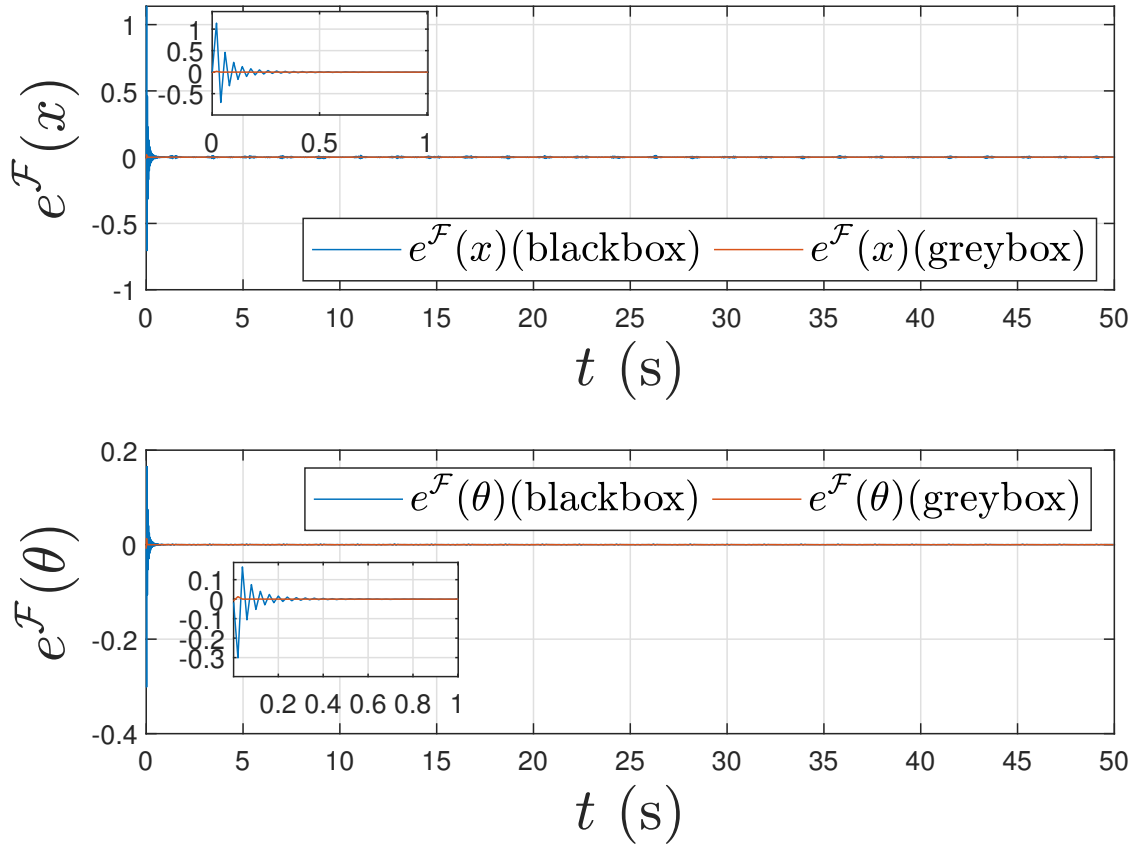

FIGURE 5.3: Comparison of black-box and gray-box systems: estimation errors in the unknown (disturbance) inputs

5.5 Conclusion

This work considers estimation of dynamic uncertain inputs and data-enabled control of a control-affine system for output tracking in discrete time. The dynamics model of the system is partly known, and the uncertain (disturbance) input observer is used to estimate the unknown part of the dynamics. This disturbance observer is designed to be Hölder-continuous and finite-time stable. The data-enabled tracking control scheme uses the

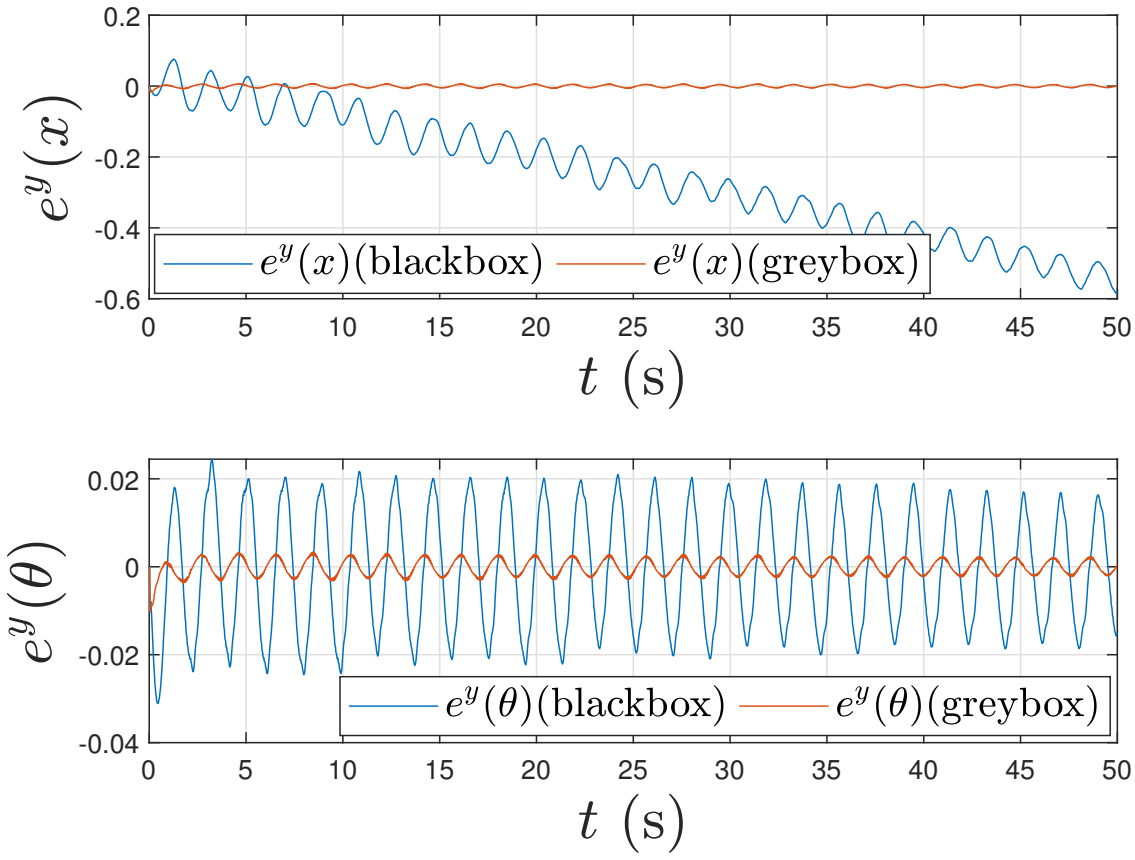

FIGURE 5.4: Comparison of black-box and gray-box systems: output trajectory tracking errors for inverted pendulum on a cart system.

disturbance estimate provided by the disturbance observer, for feedforward cancellation of this disturbance. This control scheme is shown to be finite-time stable in the case of perfect estimation of the disturbance, and robust to this estimation error otherwise. In future work, we plan to account for bounds in control inputs and estimation of the control influence matrix when knowledge of that is not satisfactory.

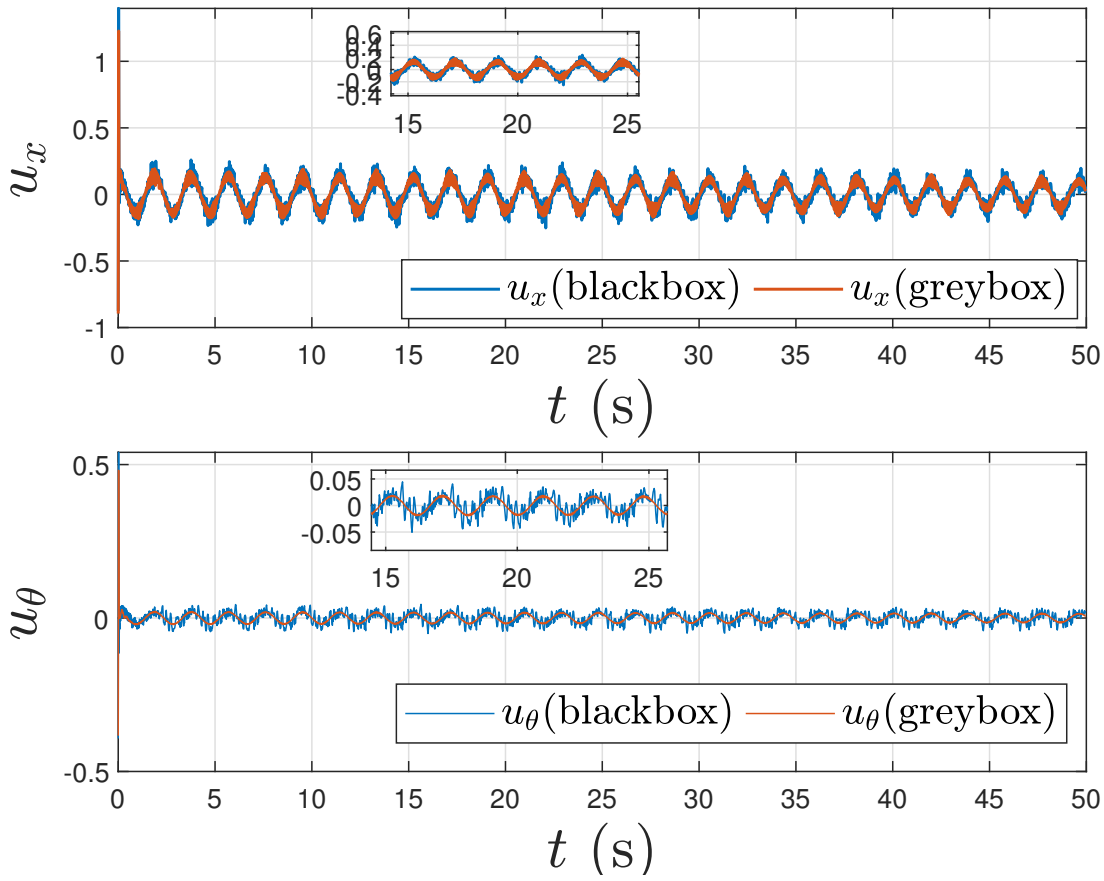

FIGURE 5.5: Comparison of black-box and gray-box systems: control input profiles.

Chapter 6

Reference Governor for Constrained Data-Driven Control of Aerospace Systems with Unknown Input-Output Dynamics

This chapter considers the design of a reference governor to satisfy pointwise-in-time output and control constraints in the setting of data-driven control of aerospace systems with unknown input-output dynamics. This is carried out in the setting of an ultra-local model (ULM), which models the unknown dynamics as described in Sanyal, 2022 and as depicted in Fig. 6.1.

The section 6.1 outlines preliminary concepts and assumptions on the system model for the data-driven control approach. This unknown dynamics lumps together the combined effects of unknown internal (state space) dynamics, disturbance forces and torques, and unknown internal (mass/inertia) parameters. The unknown dynamics are modeled

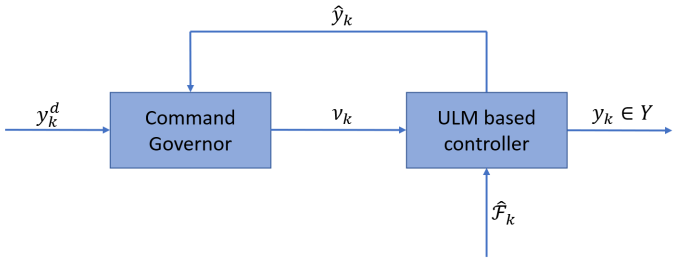

FIGURE 6.1: ULM-based reference governor schematic

by a control-affine ultra-local model (ULM) in discrete time. The robust observer estimates the unknown dynamics that guarantees finite-time stable convergence of observer errors. These estimates compensate for the unknowns in the nonlinearly stable tracking control law.

The section 6.2 illustrates the design of constraint admissible sets and reference governor for data-driven control. A reference governor is an add-on scheme that enforces the output and control constraints by modifying, when required, a reference command to the system with unknown input-output dynamics. The reference command is determined on the basis of constraint admissible sets constructed in a data-driven setting and exploiting our ULM. A Lyapunov analysis is carried out to ensure that the output of the reference governor-based control system converges to a desired output trajectory that meets the constraints.

The section 6.3 presents the numerical simulation results for aircraft longitudinal flight control with the reference governor-based data-driven control scheme. The simulation results demonstrate the performance of the controller and the enforcement of the constraints.

6.1 Problem Formulation

In this section, we describe the concept of a “black box" ultra-local model (ULM) that models the unknown input-output dynamics. This ULM is used to design a finite-time stable observer for unknown dynamics.

6.1.1 Ultra-local model for unknown systems

The ultra-local model representing a system with n inputs and m outputs with unknown internal dynamics in discrete time is given by:

$$y_{k+v} = \mathcal{F}_k + \mathcal{G}_k u_k, \tag{6.1}$$

where $y_k \in \mathbb{R}^n$ is the output vector which denotes the measured output variables, $\mathcal{F}_k \in \mathbb{R}^n$ represents the unknown dynamics which lumps together effects of internal states and parameters, external disturbance and torque, $u_k \in \mathbb{R}^m$ is the control input vector and $\mathcal{G}_k \in \mathbb{R}^{n\times m}$ is a control gain matrix that is part of the controller design. Additionally, the system is sampled in an increasing sequence of time instants t_k, where $k \in \mathbb{W} = \{0, 1, 2, \dots\}$ and $\mathbb{W}$ denotes the index set of whole numbers. The unknown dynamics modeled by the ultra-local model (6.1) satisfies the following assumptions. These assumptions ensure that a given output trajectory can be tracked by the control inputs.

Assumption 6.1.1. *The control gain matrix $\mathcal{G}_k$ is a full-rank matrix with the same number of inputs and outputs $(m = n)$.*

Assumption 6.1.2. *The unknown dynamics represented by $\mathcal{F}_k$ and the control gain matrix $\mathcal{G}_k$ are Lipschitz continuous such that,*

$$\begin{aligned} \|\mathcal{F}_{k+1} - \mathcal{F}_k\| &\leq L_F \|\xi_{k+1} - \xi_k\|, \\ \|\mathcal{G}_{k+1} - \mathcal{G}_k\| &\leq L_G \|\xi_{k+1} - \xi_k\|, \end{aligned} \tag{6.2}$$

where L_F, L_G are Lipschitz constants and $\xi_k = (y_k, y_{k+1}, \ldots, y_{k+v-1}, z_k, u_k, t_k)$ where z_k is a vector of unknown internal states and parameters. Here and in the sequel, $\|\cdot\|$ denotes the 2-norm unless specified otherwise.

6.1.2 First order model-free finite time stable observer

A discrete-time first-order observer for the unknown dynamics $\mathcal{F}_k$ in (6.1) is given in (Sanyal, 2022) and used in this work. Let $\hat{\mathcal{F}}_k$ be the estimate of the unknown $\mathcal{F}_k$, which is based on previously estimated values of $\mathcal{F}_i$ obtained from the measured outputs y_i for $i \in \{0, \ldots, k-1\}$. Define the estimation error:

$$e_k^{\mathcal{F}} := \hat{\mathcal{F}}_k - \mathcal{F}_k. \tag{6.3}$$

Assumption 6.1.3. *The unknown dynamics $\mathcal{F}_k$ and its estimate $\hat{\mathcal{F}}_k$ are bounded.*

Now, we state the following results which are proved in (Sanyal, 2022).

Proposition 6.1.1. Consider the estimation error $e_k^{\mathcal{F}}$ as defined in (6.3) and let $r \in]1, 2[$ and $\lambda > 0$ be the constants. Let the first order finite difference of the unknown dynamics $\mathcal{F}_k$, given by

$$\Delta\mathcal{F}_k := \mathcal{F}_{k+1} - \mathcal{F}_k \tag{6.4}$$

be bounded as defined in (6.2). Let the control influence matrix $\mathcal{G}_k$ be bounded as defined in (6.2). Let the nonlinear observer be given by

$$\begin{aligned} \hat{\mathcal{F}}_{k+1} &= \mathcal{D}(e_k^{\mathcal{F}})e_k^{\mathcal{F}} + \mathcal{F}_k, \\ \text{where } \mathcal{D}(e_k^{\mathcal{F}}) &= \frac{((e_k^{\mathcal{F}})^{\mathrm{T}} e_k^{\mathcal{F}})^{1-1/r} - \lambda}{((e_k^{\mathcal{F}})^{\mathrm{T}} e_k^{\mathcal{F}})^{1-1/r} + \lambda}, \end{aligned} \tag{6.5}$$

and $\mathcal{F}_k = y_{k+v} - \mathcal{G}_k u_k$ from (6.1). Then the estimation error $e_k^{\mathcal{F}}$ converges to a bounded neighborhood of $0 \in \mathbb{R}^n$ in finite time, where bounds on this neighborhood can be determined from bounds on $\Delta\mathcal{F}_k$.

The above result proves the stability of the observer for the unknown dynamics $\mathcal{F}_k$. The following result proved in (Sanyal, 2022), gives the robustness of this observer.

Proposition 6.1.2. Consider the observer design in (6.5) for the unknown $\mathcal{F}_k$ in the ultra-local model (6.1). Let the first order difference $\Delta\mathcal{F}_k$ from (6.4) be bounded according to

$$\|\Delta\mathcal{F}_k\| \leq B^{\mathcal{F}}, \tag{6.6}$$

where $B^{\mathcal{F}} \in \mathbb{R}^+$ is a known constant. Then the observer error $e_k^{\mathcal{F}}$ converges to the neighbourhood given by

$$\mathcal{E} := \{e_k^{\mathcal{F}} \in \mathbb{R}^n \ : \ \sigma(e_k^{\mathcal{F}}) \left\| e_k^{\mathcal{F}} \right\| \leq B^{\mathcal{F}}\}, \tag{6.7}$$

for some finite $k > N$, $N \in \mathbb{W}$, where

$$\sigma(e_k^{\mathcal{F}}) := 1 + \mathcal{D}(e_k^{\mathcal{F}}). \tag{6.8}$$

Note that the above result gives ultimate bounds on the estimation error of the unknown (or disturbance) dynamics $\mathcal{F}_k$, where the bounds depend on its rate of change $\Delta\mathcal{F}_k$.

6.2 Reference Governor

In this section, we enhance the model-free control approach based on ULM with a reference governor to enforce constraints without delay ($v = 1$). The modified reference command, which is subjected to a constraint admissible set, is designed by this reference governor.

6.2.1 Nominal controller

Consider the ultra-local model defined in (6.1), with the following nominal controller:

$$\mathcal{G}_k u_k = -\hat{\mathcal{F}}_k + \Phi y_k + \Lambda \nu_k, \tag{6.9}$$

where $\nu_k := \nu(t_k)$ is the modified reference command, $\Phi, \Lambda \in \mathbb{R}^{m\times m}$ are tuning matrices, Φ is Schur (all eigenvalues are located in the interior of the unit disk) and the estimate $\hat{\mathcal{F}}_k$ acts as a feed-forward cancellation term. Substituting the nominal controller in the ultra-local model (6.1) leads to the following closed-loop model:

$$y_{k+1} = \Phi y_k + \Lambda \nu_k - e_k^{\mathcal{F}} \tag{6.10}$$

Output constraints, which may arise from state constraints, are described by:

$$y_k \in Y \tag{6.11}$$

where $Y \subset \mathbb{R}^n$ is a known constraint set. We make the following assumption about this constraint set.

Assumption 6.2.1. *The set Y is compact, convex, and symmetric about the origin, which is in its interior.*

6.2.2 Constraint admissible set

The constraint admissible set O_∞ is defined as a set of all initial conditions such that the predicted response of (6.10) corresponding to the initial state and constant command ν satisfies constraints defined in (6.11). More formally,

$$O_\infty = \{(y_0, \nu) \ : \ y_k(y_0, \nu, \{e_k^{\mathcal{F}}\}) \in Y, \ \forall \{e_k^{\mathcal{F}}\} \in \mathcal{E}\}, \tag{6.12}$$

where $y_k(y_o, \nu, e_k^{\mathcal{F}})$ is the solution of system (6.1) given by

$$y_{k+1} = \Phi^{k+1} y_0 + \sum_{i=0}^{k} \left(\Phi^{k-i}\Lambda\nu + \Phi^{k-i} e_i^{\mathcal{F}}\right), \tag{6.13}$$

and $\mathcal{E}$ and Y are defined in (6.7) and (6.11), respectively. Note that our reference governor design will assume that the observer error has converged to the set given in (6.7). To obtain the constraint admissible set, the concept of the Pontryagin difference is used here.

For U and $V \subset \mathbb{R}^n$ the Pontryagin difference $U \sim V$ is given by the set,

$$U \sim V := \{x \in \mathbb{R}^n : x + v \in U,\ \forall\, v \in V\}. \tag{6.14}$$

Consider,

$$\begin{aligned} \Upsilon_0 &= \Upsilon, \\ \Upsilon_1 &= \Upsilon \sim \mathcal{E}, \\ &\vdots \\ \Upsilon_{k+1} &= \Upsilon \sim \mathcal{E} \sim \cdots \sim \Phi^k \mathcal{E}. \end{aligned} \tag{6.15}$$

Then, from (Kolmanovsky and Gilbert, 1998) we get,

$$O_k = \left\{(y_0, \nu) \in \mathbb{R}^n \times \mathbb{R}^n :\ \Phi^i y_0 + \sum_{i=0}^{k} \Phi^{k-i} \Lambda \nu \in \Upsilon_i,\ i = 0, \ldots, k \right\}. \tag{6.16}$$

Using (6.15) and (6.16), we can obtain the following recursions:

$$\Upsilon_{k+1} = \Upsilon_k \sim \Phi^k \mathcal{E} \ \text{ where } \Upsilon_0 = \Upsilon, \tag{6.17}$$

$$\begin{aligned} O_0 &= \{(y_0, \nu) \in \mathbb{R}^n \times \mathbb{R}^n : y_0 \in \Upsilon\}, \\ O_{k+1} &= O_k \cap \{(y_0, \nu) \in \mathbb{R}^n \times \mathbb{R}^n : \Phi^{k+1} y_0 + \Phi^k \Lambda \nu \in \Upsilon_{k+1}\}. \end{aligned} \tag{6.18}$$

where $k \in Z^+$. Therefore, from (6.12), we obtain the constraint admissible set as

$$O_\infty = \bigcap_{k \in Z^+} O_k. \tag{6.19}$$

To ensure finite-termination of the set sequence, typically a strict feasibility constraint on ν is added; see (Gilbert and Kolmanovsky, 1999) for details. This constraint has not been used in the present work; instead O_k was computed up to a sufficiently large index k and used as an approximation to O_∞. The design of the reference governor is given in the following subsection.

6.2.3 Reference governor design

The reference governor considers the modified reference input ν_k as an optimization variable which is obtained at each sampling instant k by solving an optimization problem. It is obtained as the solution to the following minimization problem:

$$\begin{aligned} \nu_k^* = \arg \min_{\nu} \quad & \|\nu - r_k\|_R^2 \\ \text{s.t.} \quad & (y_k, \nu) \in O_\infty, \end{aligned} \tag{6.20}$$

where R is a positive definite matrix, $\|x\|_R^2 = x^{\mathrm{T}} R x$ and O_∞ is given in (6.12).

6.2.4 Control constraints

We define the control constraints in the following form:

$$\|u_k\| \leq \mu, \tag{6.21}$$

where μ is the upper bound on control inputs. Multiplying both sides of the above equation by the control gain matrix $\mathcal{G}_k$ results in

$$\|\mathcal{G}_k u_k\| \leq \|\mathcal{G}_k\| \|u_k\| \leq \|\mathcal{G}_k\| \mu. \tag{6.22}$$

The control constraint can be satisfied through an appropriate design of the control gain matrix $\mathcal{G}_k$. From (6.9), we define

$$\omega_k := -\hat{\mathcal{F}}_k + \Phi y_k + \Lambda v_k. \tag{6.23}$$

Then, using (6.9), (6.22), and (6.23) we obtain the following inequality:

$$\|\omega_k\| = \left\|\Phi y_k + \Lambda v_k - \hat{\mathcal{F}}_k\right\| \leq \|\mathcal{G}_k\| \mu, \tag{6.24}$$

which can be written as

$$\|\mathcal{G}_k\| \geq \frac{1}{\mu} \|\omega_k\|. \tag{6.25}$$

This leads to the following condition for the control gain $\mathcal{G}_k$:

$$\|\mathcal{G}_k\| \geq \frac{1}{\mu} \left\|\Phi y_k + \Lambda v_k - \hat{\mathcal{F}}_k\right\|. \tag{6.26}$$

The control gain matrix $\mathcal{G}_k$ is then designed as

$$\mathcal{G}_k := \alpha_k \check{\mathcal{G}}, \tag{6.27}$$

where α_k is a tuning parameter and $\check{\mathcal{G}}$ is a positive diagonal matrix. This tuning parameter can be designed as

$$\alpha_k = \frac{1}{\mu \check{g}^i} \left\| \Phi y_k + \Lambda \nu_k - \hat{\mathcal{F}}_k \right\|, \tag{6.28}$$

where $\check{g}^i$ denotes as the smallest diagonal element in $\check{\mathcal{G}}$.

6.2.5 Stability Analysis

The stability and robustness analysis of the disturbance (unknown dynamics) observer and control law is presented in (Sanyal, 2022). Here we characterize the ultimate bound on the tracking error for a constant ν. Such a bound is useful in verifying conditions for the convergence of the reference governor with constrained inputs (Gilbert and Kolmanovsky, 1999).

With the control law given in §6.2.1, we define the output trajectory tracking error as

$$e_k^y = \nu - y_k. \tag{6.29}$$

Subtracting ν from both sides of (6.10), we get

$$\nu - y_{k+1} = \nu - \Phi y_k - \Lambda \nu + e_k^{\mathcal{F}}. \tag{6.30}$$

The gain matrices Φ, and Λ are defined in §6.2.1 and can be designed such that

$$\Lambda = I - \Phi, \tag{6.31}$$

where I is the $n \times n$ identity matrix. Using this design of gain matrices we obtain

$$\nu - y_{k+1} = \nu - \Phi(y_k - \nu) - \nu + e_k^{\mathcal{F}}. \tag{6.32}$$

Finally, substituting (6.29) in the above equation leads to the following error dynamics:

$$e_{k+1}^{y} = \Phi e_k^{y} + e_k^{\mathcal{F}}. \tag{6.33}$$

Theorem 6.2.1. Consider the closed-loop model for the unknown system (6.10), the control law (6.9) and the observer law (6.5). Let the estimation error in (6.3) be bounded according to

$$\left\| e_k^{\mathcal{F}} \right\| \leq B \quad \text{for } k > N, \tag{6.34}$$

where bound $B \in \mathbb{R}^+$ and $N \in \mathbb{W}$ are known. Then the output trajectory tracking error e_k^{y} will converge to the neighborhood given by

$$N^{y} := \left\{ e_k^{y} \in \mathbb{R}^n \ : \ \rho(\|\Phi\|) \left\| e_k^{y} \right\| \leq B \right\}, \tag{6.35}$$

for $k > N' > N$ where $N, N' \in \mathbb{W}$, and

$$\rho(\|\Phi\|) := 1 - \|\Phi\|. \tag{6.36}$$

Proof. Consider the following discrete Lyapunov function for output tracking error,

$$V_k^{y} = \frac{1}{2} (e_k^{y})^{\mathrm{T}} e_k^{y}. \tag{6.37}$$

The first difference of the Lyapunov function is given by,

$$V_{k+1}^{y} - V_{k}^{y} = (e_{k+1}^{y} + e_{k}^{y})^{\mathrm{T}}(e_{k+1}^{y} - e_{k}^{y}). \tag{6.38}$$

Substituting the error dynamics (6.33) in above expression, we obtain

$$\begin{aligned} V_{k+1}^{y} - V_{k}^{y} &= (\Phi e_{k}^{y} + e_{k}^{\mathcal{F}} + e_{k}^{y})^{\mathrm{T}}(\Phi e_{k}^{y} + e_{k}^{\mathcal{F}} - e_{k}^{y}) \\ &= ((\Phi + I)e_{k}^{y} + e_{k}^{\mathcal{F}})^{\mathrm{T}}((\Phi - I)e_{k}^{y} + e_{k}^{\mathcal{F}}). \end{aligned}$$

After some algebraic manipulations, the following equation is obtained:

$$\begin{aligned} V_{k+1}^{y} - V_{k}^{y} = (\Phi e_{k}^{y})^{\mathrm{T}}(\Phi e_{k}^{y}) - (e_{k}^{y})^{\mathrm{T}} e_{k}^{y} \\ + 2(e_{k}^{\mathcal{F}})^{\mathrm{T}}(\Phi e_{k}^{y}) + (e_{k}^{\mathcal{F}})^{\mathrm{T}} e_{k}^{\mathcal{F}}. \end{aligned} \tag{6.39}$$

Using the bounds defined on $e_{k}^{\mathcal{F}}$ given in (6.34), the first difference of the Lyapunov function can be upper bounded as follows:

$$\begin{aligned} V_{k+1}^{y} - V_{k}^{y} &\leq \left\|\Phi e_{k}^{y}\right\|^{2} - \left\|e_{k}^{y}\right\|^{2} + 2B \left\|\Phi\right\| \left\|e_{k}^{y}\right\| + B^{2} \\ &= \left\|\Phi\right\|^{2} \left\|e_{k}^{y}\right\|^{2} - \left\|e_{k}^{y}\right\|^{2} + 2B \left\|\Phi\right\| \left\|e_{k}^{y}\right\| + B^{2}, \end{aligned}$$

and will be simplified as

$$V_{k+1}^{y} - V_{k}^{y} \leq -\left(1 - \left\|\Phi\right\|^{2}\right) \left\|e_{k}^{y}\right\|^{2} + 2B \left\|\Phi\right\| \left\|e_{k}^{y}\right\| + B^{2}. \tag{6.40}$$

The right-hand side of the inequality (6.40) will be negative for large initial transients in e_k^y, and can be expressed as a quadratic inequality expression in $\left\|e_k^y\right\|$ as follows,

$$(1 - \|\Phi\|^2) \left\|e_k^y\right\|^2 - 2B \|\Phi\| \left\|e_k^y\right\| - B^2 > 0. \tag{6.41}$$

Then, the condition

$$\left\|e_k^y\right\| > \frac{B}{1 - \|\Phi\|}, \tag{6.42}$$

for positive real roots of $\left\|e_k^y\right\|$ ensures that $V_{k+1}^y - V_k^y < 0$. This implies that the discrete Lyapunov function V_k^y is monotonically decreasing when the tracking error $\left\|e_k^y\right\|$ is large enough to satisfy the inequality condition (7.73) for some finite $k > N'$, where $N' > N$. Therefore, the output trajectory tracking error e_k^y will converge to the neighbourhood N^y of $0 \in \mathbb{R}^n$ given by (6.35). □

It is worth noting that, in absence of a reference governor we have $\Phi = 0$. From (Sanyal, 2022), this leads to convergence of e_k^y to the bounded neighborhood of $0 \in \mathbb{R}^n$ in finite time, where the bounds are the same as that of estimation error $e_k^{\mathcal{F}}$.

6.3 Numerical simulation results

This section presents some numerical simulation results of the proposed reference governor design for the constrained ULM-based control. These simulations are carried out using the proposed scheme to control the pitch angle of an aircraft as a SISO system, of which the dynamics is unknown to the controller.

6.3.1 Aircraft model

The dynamics model for the aircraft flying at constant velocity and altitude is given by (Polóni et al., 2014):

$$\begin{bmatrix} \dot{\alpha} \\ \dot{q} \\ \dot{\theta} \end{bmatrix} = \begin{bmatrix} -0.313 & 56.7 & 0 \\ -0.0139 & -0.426 & 0 \\ 0 & 56.7 & 0 \end{bmatrix} \begin{bmatrix} \alpha \\ q \\ \theta \end{bmatrix} + \begin{bmatrix} 0.232 \\ 0.0203 \\ 0 \end{bmatrix} \delta \tag{6.43}$$

$$y = \begin{bmatrix} 0 & 0 & 1 \end{bmatrix} \begin{bmatrix} \alpha \\ q \\ \theta \end{bmatrix}, \tag{6.44}$$

where α is the angle of attack, q is the pitch rate and θ is the pitch angle. This model, which is unknown to the tracking control law, is used to generate an initial reference (or desired) output trajectory for tracking.4

For this SISO system, the input is the elevator deflection angle δ and the output is the pitch angle θ. The pitch angle output is subjected to the constraint $|\theta| \leq 5^\circ$ and the control input is subjected to the constraint $|\delta| \leq 0.1^\circ$.

We apply the nominal controller designed in (6.9), which leads to the closed-loop form of ULM as described in (6.10). The constraint admissible set O_∞ for this model is designed according to 6.2.2 and is shown in Fig. 6.2. The constraint admissible set satisfies the output constraint requirements as expected. In addition, this set is also symmetrical with zero in the interior.

The output trajectories are illustrated in Fig. 6.3. It is shown that the nominal output trajectory violates the output constraint, whereas the actual output trajectory tracks the

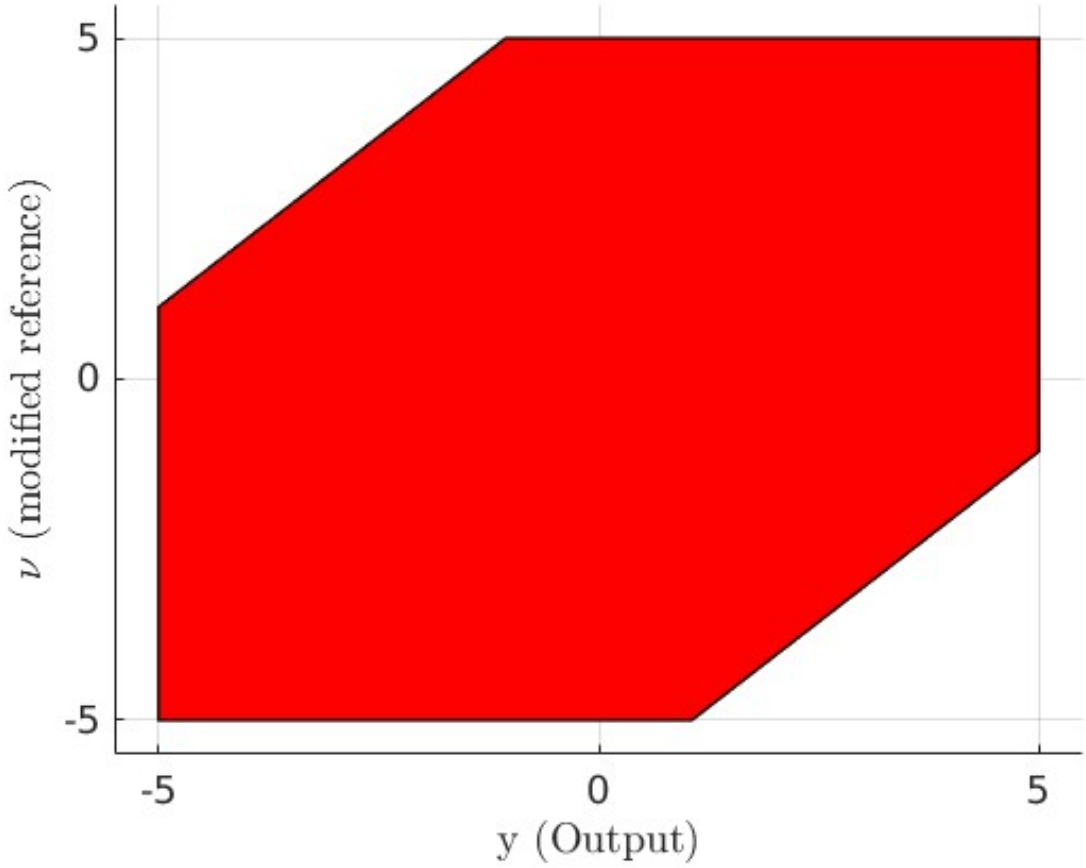

FIGURE 6.2: Constraint admissible set O_∞

modified reference trajectory while satisfying the output constraint.

Simulation results for the control input are shown in Fig. 6.4. Note that the control input constraints are satisfied within the defined limits. Fig. 6.5 illustrates the error in the estimation of the unknown dynamics $\mathcal{F}$ for the ultra-local model according to the observer design from section 6.1.2. Fig. 6.6 plots the output trajectory tracking error between modified reference command ν and the actual output trajectory, along with the error between the nominal output and actual output trajectory. Finally, Fig 6.7 illustrated the norm of control gain matrix $\mathcal{G}_k$. The change in the norm corresponds to the control

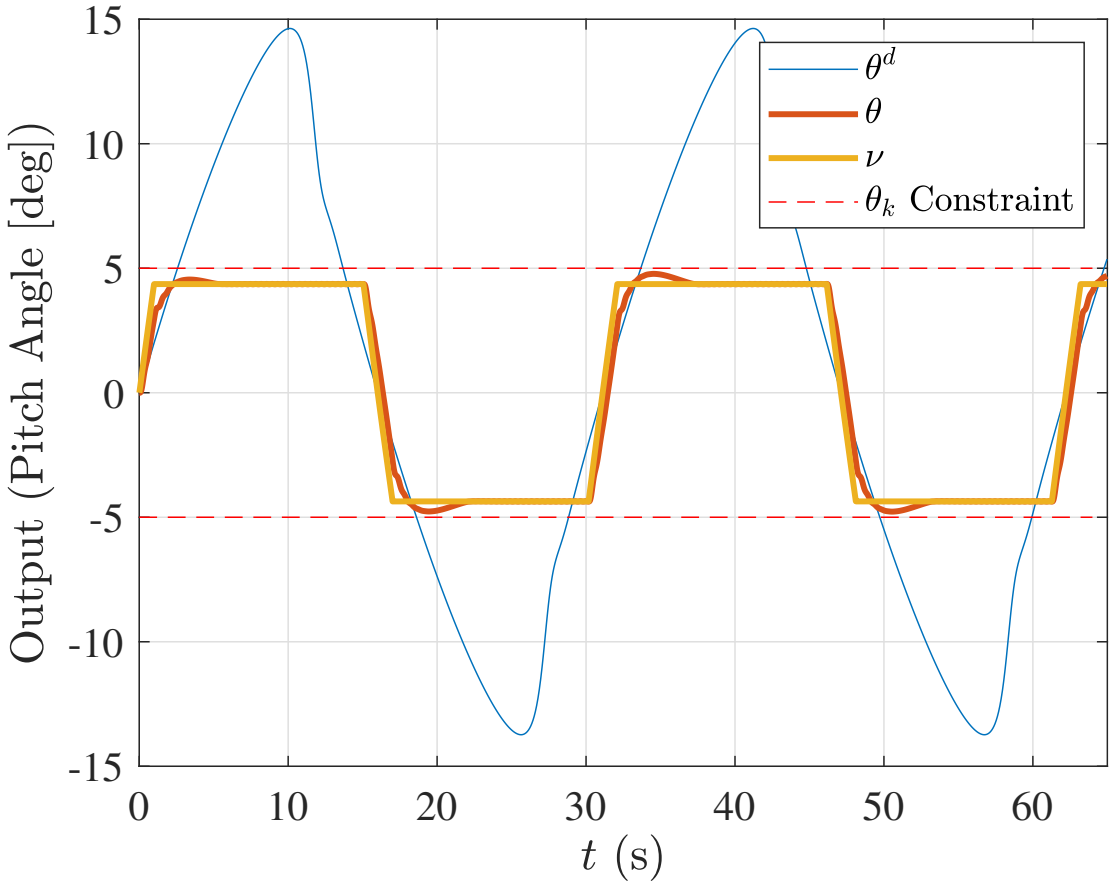

FIGURE 6.3: Desired, modified, and actual output trajectories

constraint satisfaction.

6.3.2 Effect of initial selections of $\hat{\mathcal{F}}$ and $\mathcal{G}$

Here, we study the effects of initial selections for the estimate of the unknown model, $\hat{\mathcal{F}}_0$, and the control gain matrix, $\mathcal{G}_0$, on the control input and the output trajectories.

The plots in Fig 6.8 illustrate the control inputs obtained for different initial selections. This figure shows that a decrease in the value of $\mathcal{G}_0$ leads to higher transients in the control

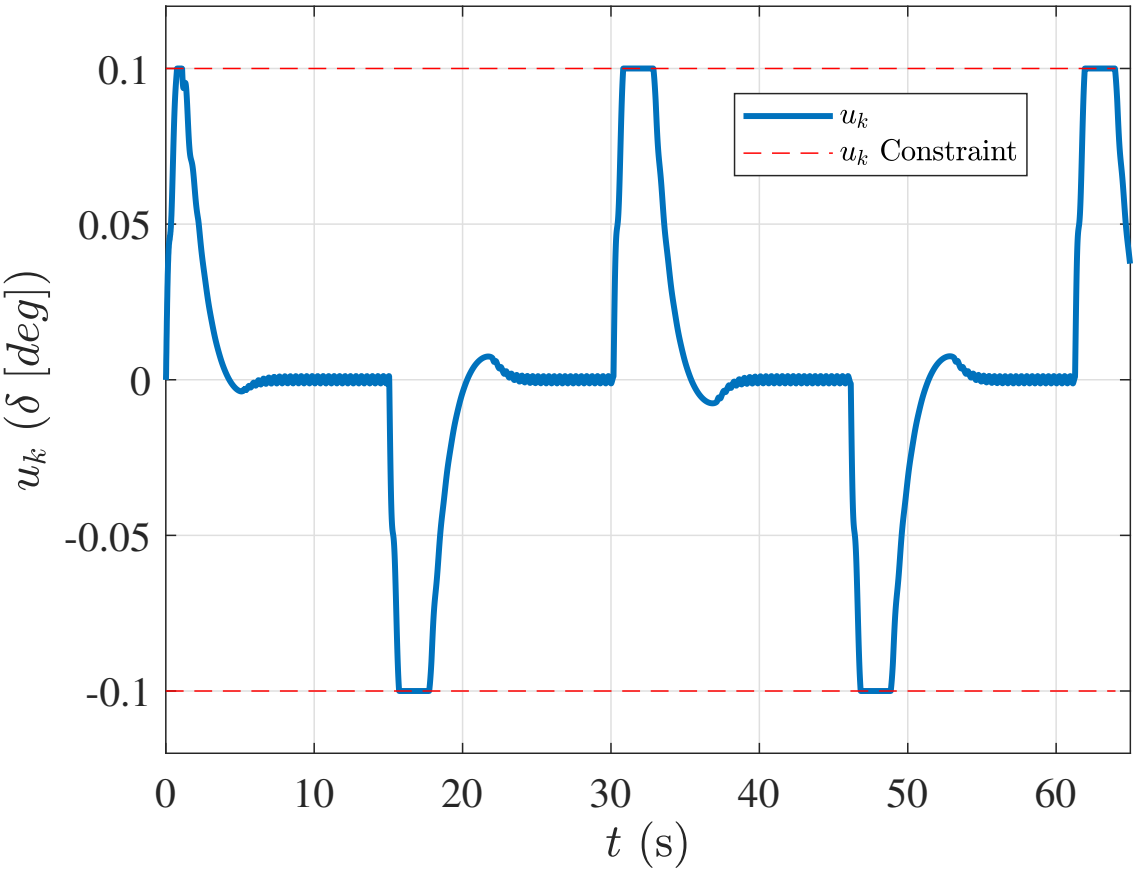

FIGURE 6.4: Control input with constraints

input and an increase in the value of $\hat{\mathcal{F}}_0$ generally causes high initial transients in the control input. It is also shown that the control constraints are satisfied in both cases.

The output trajectories in Fig 6.9 illustrate the effect of different initial values, primarily for $\hat{\mathcal{F}}_0$. As is shown in this figure, higher values of $\hat{\mathcal{F}}_0$ tend to delay the convergence of output trajectories y_k to the modified reference ν.

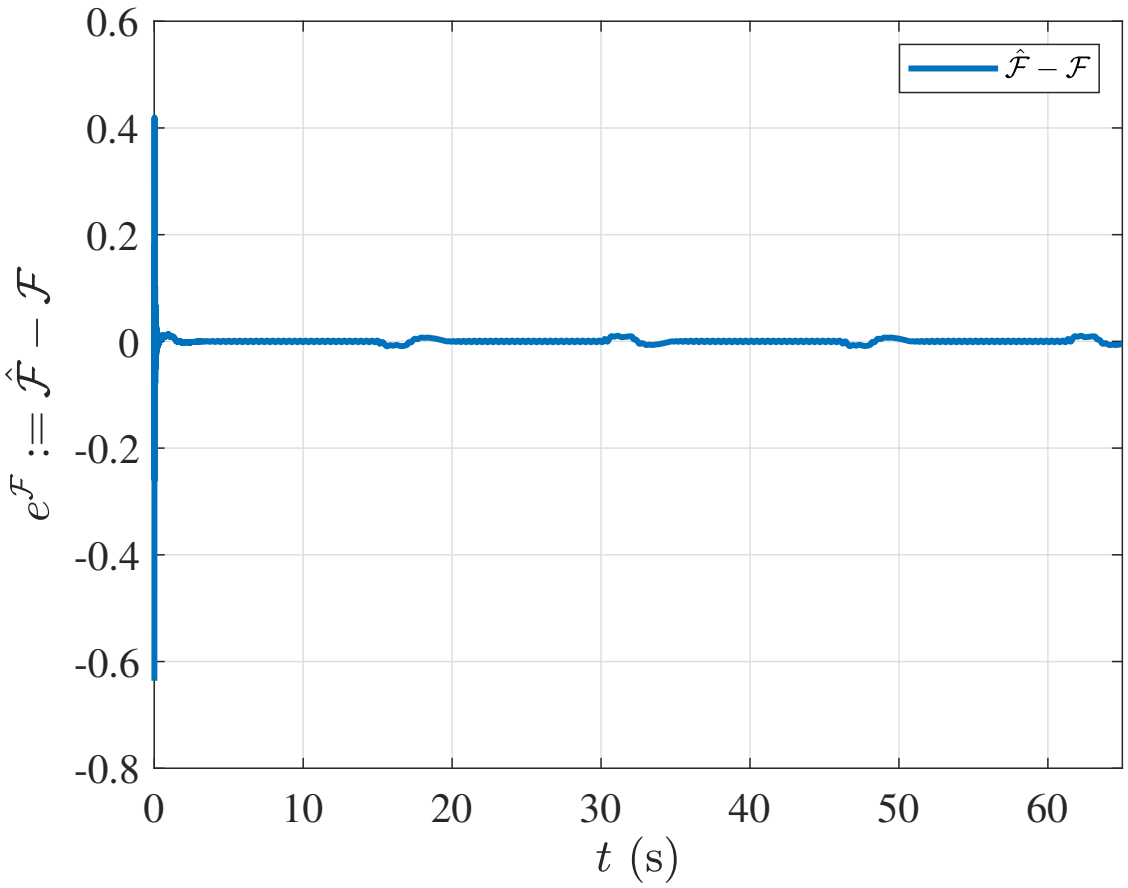

FIGURE 6.5: Model estimation error $e^{\mathcal{F}}$

6.4 Conclusion

This work considers the design of a reference governor to enforce pointwise-in-time output and control constraints for a system with unknown input-output dynamics modeled by an ULM. At each time instant, a modified command is generated that minimizes the constrained cost function. This command is determined on the basis of a constraint admissible set that is designed to enforce output constraints. The control gain matrix is

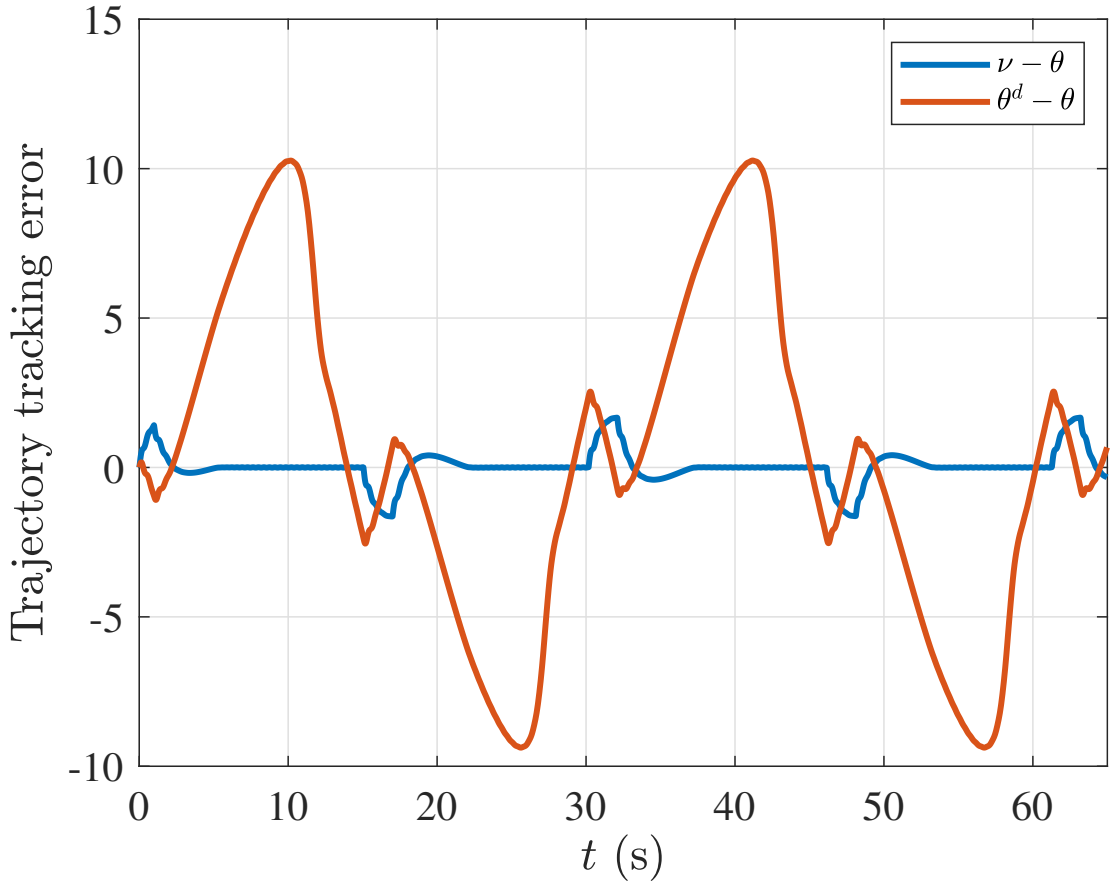

FIGURE 6.6: Output trajectory tracking error

designed to satisfy the control constraints. A Lyapunov stability analysis shows the convergence of the tracking error and the observer error to bounded neighborhoods of zero error. A numerical simulation is performed for an aircraft pitch control system, subjected to output and control constraints. The simulation results demonstrate the tracking of a reference output trajectory while satisfying the output and control constraints. In the current framework, the output constraint satisfaction for the output trajectory is conservative. This issue will be looked at in planned future work. In addition, the effect of initial

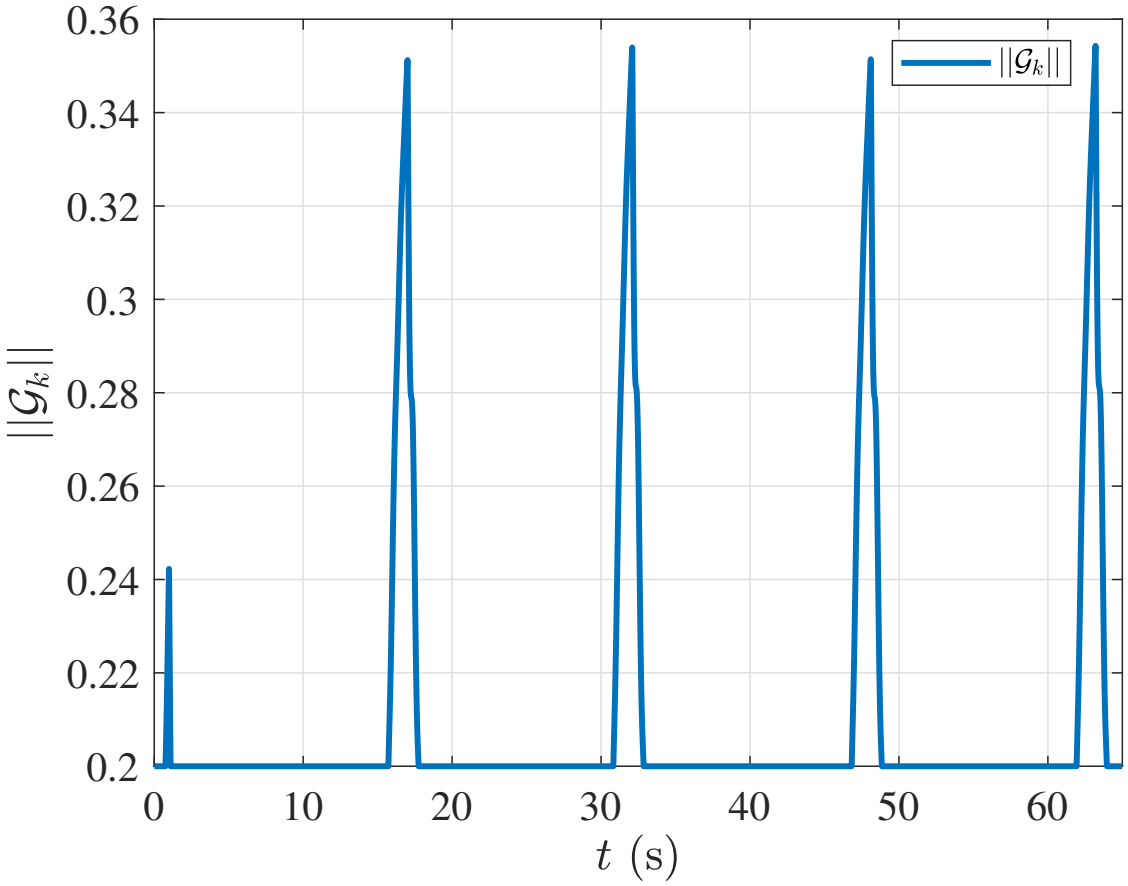

FIGURE 6.7: Norm of control gain matrix $\mathcal{G}_k$

selections of the estimate of the unknown model and the control gain matrix on the control input and output response is also illustrated through a numerical simulation study. Other topics we will explore in the future include the design of reference governors for systems with uncertainty (“gray box" models), monotonically non-increasing set bounds for the observer error, and systems with delay.

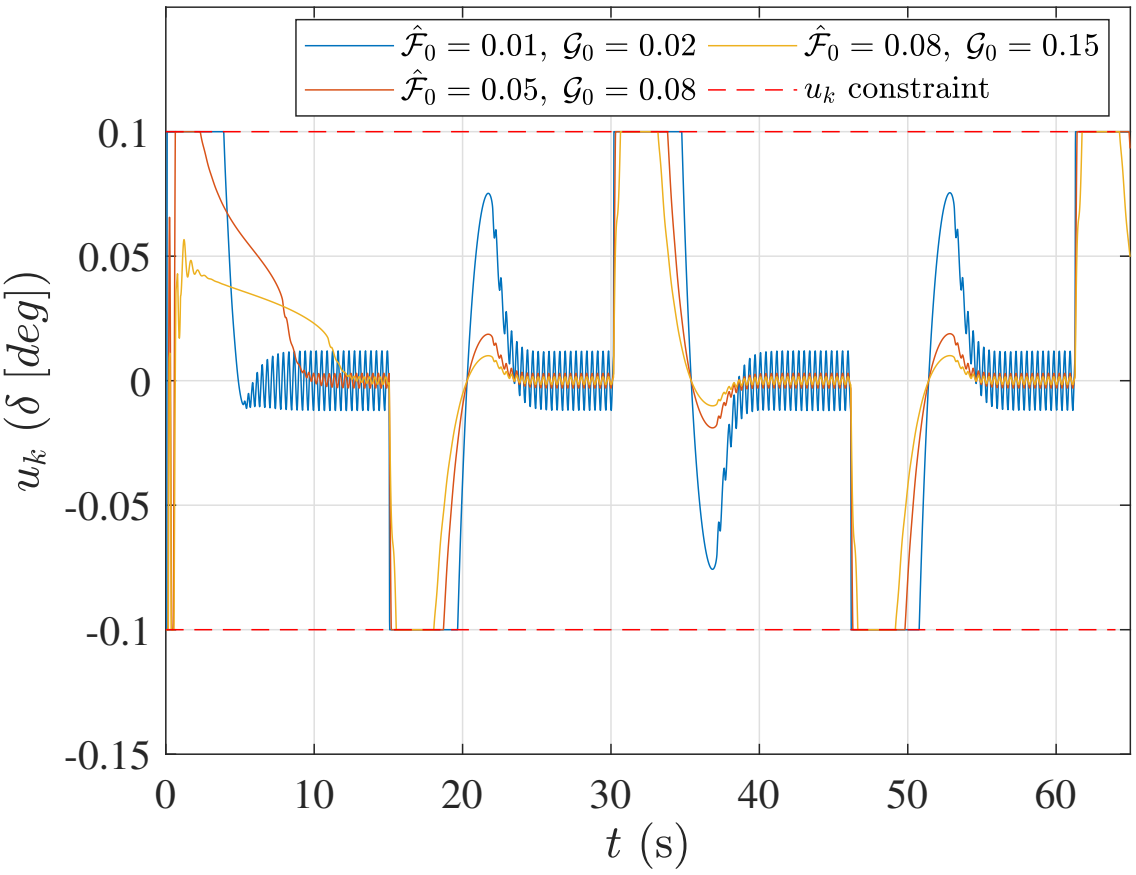

FIGURE 6.8: Control input for different initial conditions

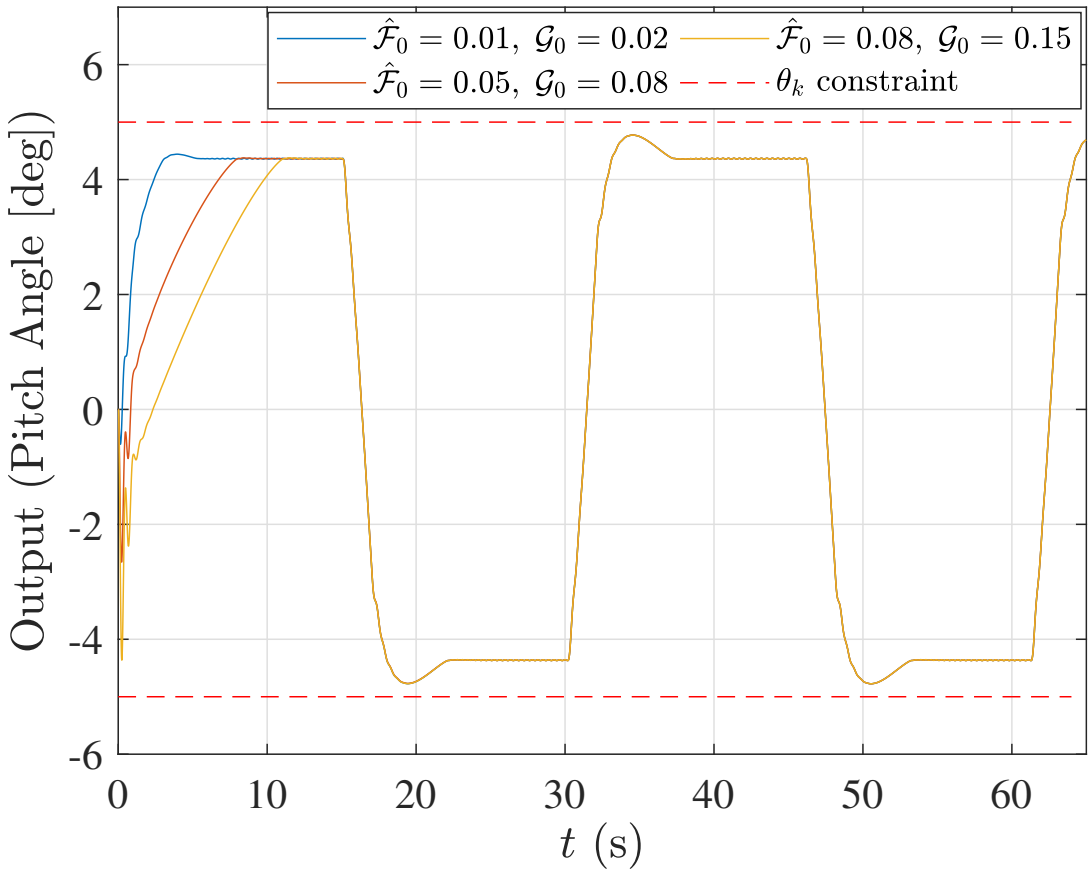

FIGURE 6.9: Output trajectory for different initial conditions

Chapter 7

Finite-time Stable Pose Estimation on $\mathrm{SE}(3)$ using Onboard Optical Sensors

This chapter presents a finite-time stable pose estimation scheme for autonomous vehicles undergoing rotational and translational motion in three dimensions, using measurements from onboard optical sensors.

The section 7.1 presents the mathematical notations and concepts used in this chapter.

In section 7.2, we introduce the formulation for the problem of pose determination from vector measure- ments obtained from optical sensors.

The section 7.3 discusses the estimation error dynamics and kinematics. We then generalize Wahbas cost function by choosing a symmetric weight matrix and show that the resulting cost function is a Morse function on the Lie group of rigid-body rotations under some easily satisfied conditions on the weight matrix. This cost function is taken as the potential function for rotational motion, and we also provide some useful lemmas associated with the potential functions for rotations and translations.

In Section 7.4, we present the problem of finite-time stable pose estimation in real-time, present the pose estimation scheme, and prove the finite-time stability of the scheme in

the absence of measurement errors, using nonlinear stability analysis. Moreover, this observer is designed directly on the Lie group of rigid body motions, SE(3), and does not require a dynamics model for the vehicle to update the state estimates. These features enable it to estimate arbitrary rotational and translational motions without encountering singularities or the unwinding phenomenon and be readily applied to a vehicle with any sensor-actuator configuration without requiring extensive re-tuning. Additionally, section 7.5 presents an in-depth analysis of the robustness of the FTS pose estimation scheme to measurement errors.

7.1 Mathematical Preliminaries

In this section, the set of real numbers is denoted by $\mathbb{R}$. Similarly, $\mathbb{R}^n$ and $\mathbb{R}^{n\times m}$ denote the set of real n-dimensional column vectors and real $n \times m$ matrices, respectively. $\mathbb{N}$ denotes the set of natural numbers. The set of all possible attitudes of a rigid body is the special orthogonal group $\mathrm{SO}(3)$ ((Murray, 2017)), which is defined by:

$$\mathrm{SO}(3) = \left\{ R \in \mathbb{R}^{3\times 3} | R^{\mathrm{T}} R = R R^{\mathrm{T}} = I,\, \det(R) = 1 \right\}.$$

This is a matrix Lie group under matrix multiplication. The Lie algebra (tangent space at identity) of $\mathrm{SO}(3)$ is denoted $\mathfrak{so}(3)$ and identified with the set of 3×3 skew-symmetric matrices:

$$\mathfrak{so}(3) = \left\{ \mathrm{S} \in \mathbb{R}^{3\times 3} \mid \mathrm{S} = -\mathrm{S}^{\mathrm{T}} \right\},\ \mathrm{S} = \begin{bmatrix} 0 & -\mathrm{s}_3 & \mathrm{s}_2 \\ \mathrm{s}_3 & 0 & -\mathrm{s}_1 \\ -\mathrm{s}_2 & \mathrm{s}_1 & 0 \end{bmatrix}.$$

Let $(\cdot)^\times : \mathbb{R}^3 \to \mathfrak{so}(3)$ denote the bijective map from three-dimensional real Euclidean space $\mathbb{R}^3$ to $\mathfrak{so}(3)$. For a vector $\mathrm{s} = [\mathrm{s}_1\ \mathrm{s}_2\ \mathrm{s}_3]^\mathrm{T} \in \mathbb{R}^3$, the matrix $\mathrm{s}^\times$ represents the vector cross product operator, that is $\mathrm{s} \times r = \mathrm{s}^\times r$, where $r \in \mathbb{R}^3$; this makes $(\cdot)^\times$ a vector space isomorphism. The inverse of $(\cdot)^\times$ is denoted by $\mathrm{vex}(\cdot) : \mathfrak{so}(3) \to \mathbb{R}^3$, such that $\mathrm{vex}(\mathrm{s}^\times) = \mathrm{s}$, for all $\mathrm{s}^\times \in \mathfrak{so}(3)$.

We define the trace inner product on $\mathbb{R}^{m\times n}$ $\langle \cdot, \cdot \rangle$ as,

$$\langle A_1, A_2 \rangle = \mathrm{tr}(A_1^\mathrm{T} A_2).$$

Any square matrix $A \in \mathbb{R}^{n\times n}$ can be written as the sum of unique symmetric and skew-symmetric matrices as given below:

$$A = \mathrm{sym}(A) + \mathrm{skew}(A), \tag{7.1}$$

where the symmetric and skew-symmetric components are defined as:

$$\mathrm{sym}(A) = \frac{1}{2}(A + A^\mathrm{T}), \mathrm{skew}(A) = \frac{1}{2}(A - A^\mathrm{T}). \tag{7.2}$$

Additionally, if $A_1 \in \mathbb{R}^{n\times n}$ is a symmetric matrix and $A_2 \in \mathbb{R}^{n\times n}$ is a skew-symmetric matrix, then,

$$\langle A_1, A_2 \rangle = 0. \tag{7.3}$$

Thus, the symmetric and skew matrices are orthogonal under the trace inner product. For all $a_1, a_2 \in \mathbb{R}^3$,

$$\left\langle a_1^\times, a_2^\times \right\rangle = 2a_1^\mathrm{T} a_2. \tag{7.4}$$

The Lie group of rigid body motions in three spatial dimensions is the special Euclidean group, denoted $\mathrm{SE}(3)$. It is the semi-direct product of $\mathrm{SO}(3)$ with $\mathbb{R}^3$, with $\mathbb{R}^3$ as the normal subgroup, i.e., $\mathrm{SE}(3) = \mathrm{SO}(3) \ltimes \mathbb{R}^3$ ((Varadarajan, 1984)). If $R \in \mathrm{SO}(3)$ and $b \in \mathbb{R}^3$, the corresponding element in $\mathrm{SE}(3)$ is represented by:

$$\mathrm{g} = \begin{bmatrix} R & b \\ 0 & 1 \end{bmatrix} \in \mathrm{SE}(3). \tag{7.5}$$

The action of $\mathrm{SE}(3)$ on $\mathbb{R}^3$ is to rotate and translate vectors in $\mathbb{R}^3$, and is represented as follows:

$$\mathrm{g} \cdot \mathrm{v} = \begin{bmatrix} R & b \\ 0 & 1 \end{bmatrix} \begin{bmatrix} v \\ 1 \end{bmatrix} = \begin{bmatrix} Rv + b \\ 1 \end{bmatrix}, \ \forall\, v \in \mathbb{R}^3,$$
$$\text{where } \mathrm{v} = \begin{bmatrix} v \\ 1 \end{bmatrix}.$$

With these definitions and identities, we formulate the pose estimation problem next.

7.2 Real-time Navigation using 3D Point Cloud Data

This section introduces a formulation for the problem of pose determination from vector measurements in the vehicle body-fixed frame $\mathcal{B}$, along with a velocity measurement model. Our FTS pose estimation scheme using 3D point clouds is based on this formulation, which will be presented in detail in Section 7.4.

7.2.1 Pose Measurement Model

Let $\mathcal{I}$ denote an inertial frame that is spatially fixed and $\mathcal{B}$ denote the body-fixed frame. The attitude of the rigid body is denoted by $R \in \mathrm{SO}(3)$, which transforms vectors in the body frame $\mathcal{B}$ to their counterparts in the inertial frame $\mathcal{I}$. The position of the origin of frame $\mathcal{B}$ expressed in frame $\mathcal{I}$ gives the position of the body, denoted as $b \in \mathbb{R}^3$. The pose is given by the frame transformation from frame $\mathcal{B}$ to frame $\mathcal{I}$, as given by eq. (7.5).

Consider optical measurements of j points at time t with known and fixed positions in frame $\mathcal{I}$, denoted as q_j. These j points generate $\binom{j}{2}$ unique relative position vectors, which are the vectors connecting any two of these observed points.

Let a_i be the relative position of the i-th stationary point in frame $\mathcal{B}$. In the absence of measurement noise, we obtain the position in frame $\mathcal{I}$ as

$$q_i = Ra_i + b. \tag{7.6}$$

The measured vectors in the presence of additive noise can be expressed as:

$$\bar{a}^m = R^{\mathrm{T}}(\bar{q} - b) + \bar{\wp}, \tag{7.7}$$

where $\bar{q}$ and $\bar{a}^m$ are defined as follows:

$$\bar{q} = \frac{1}{j}\sum_{i=1}^{j} q_i,\ \bar{a}^m = \frac{1}{j}\sum_{i=1}^{j} a_i^m, \tag{7.8}$$

and $\bar{\wp}$ is the additive measurement noise obtained by averaging the measurement noise vectors for each a_i.

Now, consider the $\binom{j}{2}$ relative position vectors for j measured points from optical sensor measurements, denoted as $d_j = q_\lambda - q_\ell$ in frame $\mathcal{I}$ and the corresponding vectors in frame $\mathcal{B}$ as $e_j = a_\lambda - a_\ell$, where λ, ℓ are any two measured points such that, $\lambda \neq \ell$. If the total number of measured vectors, $\binom{j}{2} = 2$, then $e_3 = e_1 \times e_2$ is considered a third measured direction in frame $\mathcal{B}$ with corresponding vector $d_3 = d_1 \times d_2$ in frame $\mathcal{I}$. Therefore,

$$d_j = Re_j \Rightarrow D = RE, \tag{7.9}$$

where $D = [d_1\ \ldots\ d_n],\ E = [e_1\ \ldots\ e_n] \in \mathbb{R}^{3\times n}$ with $n = 3$ if $\binom{j}{2} = 2$ and $n = \binom{j}{2}$ if $\binom{j}{2} > 2$. In the presence of measurement noise, the measured value of matrix E is given by,

$$E^m = R^{\mathrm{T}}D + \mathfrak{L}, \tag{7.10}$$

where the columns of matrix $\mathfrak{L} \in \mathbb{R}^{3\times n}$ are additive noise vectors in the vector measurements made in frame $\mathcal{B}$.

7.2.2 Velocities Measurement Model

Denote the angular and translational velocity of the rigid body expressed in frame $\mathcal{B}$ by Ω and ν, respectively. Therefore, the kinematics of the rigid body is

$$\dot{R} = R\Omega^{\times}, \quad \dot{b} = R\nu \;\Rightarrow \dot{\mathrm{g}} = \mathrm{g}\xi^{\vee}, \tag{7.11}$$

where $\xi = \begin{bmatrix} \Omega \\ \nu \end{bmatrix} \in \mathbb{R}^6$, $\xi^{\vee} = \begin{bmatrix} \Omega^{\times} & \nu \\ 0 & 0 \end{bmatrix}$. In the presence of measurement noise, the measured translational and angular velocities vector, denoted by ξ^m, is given by

$$\xi^m = \begin{bmatrix} \Omega^m \\ \nu^m \end{bmatrix} = \xi + \delta, \tag{7.12}$$

where $\delta \in \mathbb{R}^6$ is the vector of additive noise in translational and angular velocities components and is given by

$$\delta = \begin{bmatrix} \delta_\Omega \\ \delta_\nu \end{bmatrix}. \tag{7.13}$$

In the following section, we explore the dynamics and kinematics of estimation errors and present preliminary results that contribute to the design of our FTS pose estimation scheme.

7.3 Preliminary Concepts for Pose Estimation on $\mathrm{SE}(3)$

The estimated pose and its kinematics are given by

$$\widehat{\mathrm{g}} = \begin{bmatrix} \widehat{R} & \widehat{b} \\ 0 & 1 \end{bmatrix} \in \mathrm{SE}(3), \quad \dot{\widehat{\mathrm{g}}} = \widehat{\mathrm{g}}\widehat{\xi}^{\vee}, \tag{7.14}$$

where $\widehat{b}$ is the position estimate, $\widehat{R}$ is the attitude estimate, and $\widehat{\xi}$ is the rigid body velocities estimate, with $\widehat{\mathrm{g}}_0$ as the initial pose estimate. The pose estimation error is defined as

$$h = \mathrm{g}\widehat{\mathrm{g}}^{-1} = \begin{bmatrix} Q & b - Q\widehat{b} \\ 0 & 1 \end{bmatrix} = \begin{bmatrix} Q & \chi \\ 0 & 1 \end{bmatrix} \in \mathrm{SE}(3), \tag{7.15}$$

where $Q = R\widehat{R}^{\mathrm{T}}$ is the attitude estimation error, and $\chi = b - Q\widehat{b}$. In the absence of measurement noise, we have

$$\dot{h} = h\varphi^{\vee}, \text{ where } \varphi(\widehat{\mathrm{g}}, \xi^m, \widehat{\xi}) = \begin{bmatrix} \omega \\ v \end{bmatrix} = \mathrm{Ad}_{\widehat{\mathrm{g}}}(\xi - \widehat{\xi}), \tag{7.16}$$

where $\xi^m = \xi \in \mathbb{R}^6$ is the measured rigid body velocities defined as in (7.12), v and ω are translational and angular velocity estimation errors respectively, and $\mathrm{Ad}_{\mathfrak{g}} = \begin{bmatrix} \mathfrak{R} & 0 \\ \mathfrak{b}^{\times}\mathfrak{R} & \mathfrak{R} \end{bmatrix}$

for $\mathfrak{g} = \begin{bmatrix} \mathfrak{R} & \mathfrak{b} \\ 0 & 1 \end{bmatrix}$. The position and attitude estimation error kinematics are:

$$\begin{aligned} \dot{\chi} = Qv, \quad \dot{Q} = Q\omega^{\times}, \\ \text{where } \omega = \widehat{R}(\Omega - \widehat{\Omega}),\ v = \widehat{R}(\nu - \widehat{\nu}) - \omega^{\times}\widehat{b}. \end{aligned} \tag{7.17}$$

The position and the attitude $(\widehat{b}, \widehat{R})$ estimates are obtained in real time, using the matrices which consist of known inertial vectors D defined in (7.9), the corresponding vector measured vectors in the body-fixed frame E^m, and the translational and angular velocities measurements ζ^m. The mass, moment of inertia, and other parameters that occur in the dynamics of the rigid body are unknown. The number of vector measurements can be varying over time, provided that there are at least two non-collinear vectors measured optically at all times, for unique attitude determination. The design of the FTS pose estimator given in Section 7.4 is shown to provide almost global finite-time stable (AGFTS) estimates of the pose, where these estimates converge to the respective true values b and R in finite time, in the absence of measurement noise. Additionally, the robustness of this estimator in the presence of measurement noise is demonstrated in section 7.5.

7.3.1 Potential Functions for Pose Estimation Errors

Consider the following potential function for the position estimation error:

$$\mathcal{U}_t(\widehat{g}, \bar{a}^m, \bar{q}) = \frac{1}{2}\kappa\, y^{\mathrm{T}} y = \frac{1}{2}\kappa \left\| \bar{q} - \widehat{R}\bar{a}^m - \widehat{b} \right\|^2, \tag{7.18}$$

where $y \equiv \bar{q} - \widehat{R}\bar{a}^m - \widehat{b}$ and κ is a positive scalar.

Now, consider the potential function for attitude estimation error. The objective is to obtain an estimate of the attitude denoted by $\widehat{R} \in \mathrm{SO}(3)$ from n known inertial vectors $d_1, \ldots, d_n$ and corresponding measured vectors $e_1^m, \ldots, e_n^m$, where n is as defined after eq. (7.9). The attitude determination formulated as an optimization problem as follows,

$$\mathrm{Min}_{\widehat{R}} \mathcal{U}_r(\widehat{g}, D, E^m) = \frac{1}{2} \sum_{i}^{n} w_i (d_i - \widehat{R} e_i^m)^{\mathrm{T}} (d_i - \widehat{R} e_i^m), \tag{7.19}$$

where $w_i > 0$ are weight factors. This is referred to as Wahba's problem as in (Wahba, 1965). The cost function is re-expressed as,

$$\mathcal{U}_r(\widehat{g}, D, E^m) = \frac{1}{2} \left\langle D - \widehat{R} E^m, (D - \widehat{R} E^m) W \right\rangle, \tag{7.20}$$

where $W = \mathrm{diag}([w_1, \ w_2, \ \ldots, \ w_n]) \in \mathbb{R}^{n \times n}$. The cost function can be generalized such that W is a symmetric positive semi-definite matrix satisfying conditions which is described in the following lemmas. Therefore, the total potential function is obtained as a sum of the translational and rotational potential functions and is given by:

$$\begin{aligned} \mathcal{U}(\widehat{g}, \bar{a}^m, \bar{q}, D, E^m) &= \mathcal{U}_t(\widehat{g}, \bar{a}^m, \bar{q}) + \mathcal{U}_r(\widehat{g}, D, E^m) \\ &= \frac{1}{2} \kappa \, y^{\mathrm{T}} y \\ &+ \frac{1}{2} \left\langle D - \widehat{R} E^m, (D - \widehat{R} E^m) W \right\rangle, \end{aligned} \tag{7.21}$$

where $\mathcal{U}_t(\widehat{g}, \bar{a}^m, \bar{q})$ and $\mathcal{U}_r(\widehat{g}, D, E^m)$ are defined in equations (7.18) and (7.20) respectively. The following lemma gives the generalized cost function in the absence of measurement errors.

Lemma 1. *Define $Q = R\widehat{R}^T$ as the attitude estimation error. Let $D \in \mathbb{R}^{3 \times n}$ be as defined as in*

(7.9) *with* $rank(D) = 3$. *Let the gain matrix* W *of the generalized Wahba cost function be given by,*

$$W = D^T\left(DD^T\right)^{-1}K\left(DD^T\right)^{-1}D, \tag{7.22}$$

where $K = \text{diag}([k_1, k_2, k_3])$ *and* $k_1 > k_2 > k_3 \geq 1$. *Then, in the absence of measurement errors,*

$$\mathcal{U}_r(h, D) = \frac{1}{2}\left\langle D - \widehat{R}E^m, (D - \widehat{R}E^m)W\right\rangle = \langle K, I - Q\rangle\,, \tag{7.23}$$

which is a Morse function on $\text{SO}(3)$ *whose critical points are given by the set,*

$$\begin{aligned}\mathcal{C} = \{&I, \text{diag}([-1, -1, 1]), \text{diag}([1, -1, -1]),\\ &\text{diag}([-1, 1, -1])\}.\end{aligned} \tag{7.24}$$

In addition, $\mathcal{U}_r$ *has a global minimum at* $Q = I$.

The proof for this result has been provided in (Hamrah, Warier, and Sanyal, 2021) and is not repeated here.

The instantaneous attitude determination problem can be solved by determining $\widehat{R}$ that minimizes the $\mathcal{U}_r$ at any given instant. Substituting (7.23) in (7.21), the total potential function in the absence of measurement errors is expressed as follows:

$$\begin{aligned}\mathcal{U}(h, D, \bar{q}) &= \mathcal{U}_t(h, \bar{q}) + \mathcal{U}_r(h, D)\\ &= \frac{1}{2}\kappa\, y^{\mathrm{T}}y + \langle K, I - Q\rangle\,,\end{aligned} \tag{7.25}$$

where

$$\begin{aligned} y \equiv y(h, \bar{q}) &= \bar{q} - \widehat{R}\bar{a} - \widehat{b} \\ &= Q^{\mathrm{T}}\chi + (I - Q^{\mathrm{T}})\bar{q}, \end{aligned} \tag{7.26}$$

as $\widehat{b} = Q^{\mathrm{T}}(b - \chi)$.

The following lemma, which relates the error in the attitude estimation to the error in angular velocity estimation, is used in section 7.4 to prove the main result.

Lemma 2. *Let K be as defined in Lemma 1. Then, in the absence of measurement errors, the time derivative of $\mathcal{U}_r$ along the trajectories satisfying the kinematic equations (7.11),(7.12) and (7.14) is given by*

$$\frac{\mathrm{d}}{\mathrm{d}t}\mathcal{U}_r(h, D) = \frac{\mathrm{d}}{\mathrm{d}t}\langle K, I - Q\rangle = s_K(Q) \cdot \omega \tag{7.27}$$

$$= \frac{\mathrm{d}}{\mathrm{d}t}\mathrm{tr}(K - L^T\widehat{R}) = -s_L(\widehat{R}) \cdot \widetilde{\Omega}, \tag{7.28}$$

where $L = DW(E^m)^T$, $\widetilde{\Omega} = \Omega - \widehat{\Omega}$, $s_K(Q)$ is given by

$$s_K(Q) = \mathrm{vex}(KQ - Q^TK), \tag{7.29}$$

and

$$s_L(\widehat{R}) = \mathrm{vex}(L^T\widehat{R} - \widehat{R}^TL). \tag{7.30}$$

The proof of this lemma is given in (Hamrah, Warier, and Sanyal, 2021) and is omitted here for brevity.

Therefore, from equations (7.17) and (7.27), the time derivative of the total potential function $\mathcal{U}$ is obtained as

$$\frac{\mathrm{d}}{\mathrm{d}t}\mathcal{U}(h, D, \bar{q}) = \kappa\, y^{\mathrm{T}}(v + \omega^{\times}\bar{q}) + s_K(Q)\cdot\omega, \tag{7.31}$$

which will be used in the next section to prove the main result. Henceforth, for the sake of notational convenience, the total potential function will be denoted as $\mathcal{U}$ in the subsequent sections.

7.3.2 Useful Prior Results

The lemmas given here are essential to prove the main result on finite time stable pose estimation scheme given in Section 7.4.

Lemma 3. *Let x and y be non-negative real numbers and let $p \in (1,2)$. Then*

$$x^{(1/p)} + y^{(1/p)} \geq (x+y)^{(1/p)}. \tag{7.32}$$

Moreover, the above inequality is a strict inequality if both x and y are non-zero.

The interested reader can find detailed proof of this result in (Bohn and Sanyal, 2014; Bohn and Sanyal, 2016). For brevity, we omit the proof in this chapter.

Lemma 4. *Let K be as defined in Lemma 1 and $s_K(Q)$ be as given in the equation (7.29). Let $\mathcal{S} \subset \mathrm{SO}(3)$ be a closed subset containing the identity in its interior, defined by*

$$\begin{aligned}\mathcal{S} = \big\{ Q \in \mathrm{SO}(3) \;:\; & Q_{ii} \geq 0 \text{ and } Q_{ij}Q_{ji} \leq 0 \\ & \forall i,\, j \in \{1,2,3\},\, i \neq j\big\}.\end{aligned} \tag{7.33}$$

If $Q \in \mathcal{S}$, then it satisfies

$$s_K(Q)^T s_K(Q) \geq \text{tr}(K - KQ). \tag{7.34}$$

The proof of this result is given in (Bohn and Sanyal, 2016) and is omitted here for brevity.

Lemma 5. *Let $s_L(\widehat{R})$ and $s_K(Q)$ be as defined earlier. Then the following holds:*

$$s_L(\widehat{R})^T s_L(\widehat{R}) = s_K(Q)^T s_K(Q). \tag{7.35}$$

The proof for this result is provided in (Hamrah, Warier, and Sanyal, 2021) and is omitted here for brevity.

The design and stability result of the finite-time stable estimator is given in the following section. Note that the pose estimation error $h = g\widehat{g}^{-1}$ is defined on the special Euclidean group of rigid body motion, $\text{SE}(3)$, which is not a vector space. Therefore, for Lyapunov stability analysis of the observer designed on $\text{SE}(3)$, a suitable Lyapunov function is required. This comes in the form of a Morse-Lyapunov function, as defined later in Theorem 1 in Section 7.4, where the Morse function $\mathcal{U}_r = \langle K, I - Q \rangle$ on $\text{SO}(3)$ is used as the component of the Morse-Lyapunov function that depends on the attitude component of the full state. This Morse-Lyapunov function is subsequently designed and shown to guarantee convergence of state estimation errors (h, φ) to $(I, 0)$ in finite time.

7.4 Finite-time Stable Pose Estimation

The main result for the proposed finite-time stable pose observer for estimation of rigid body position and orientation is presented here. The finite-time stability of the resulting

closed-loop system is shown by utilizing the Hölder-continuous Morse-Lyapunov function.

Theorem 1. *Consider the pose kinematics, position vectors obtained from the optical measurements bounded and velocity measurements given by equations (7.11), (7.12) and (7.14) in the absence of measurement noise. Let $p \in]1,2[$ and κ, k_p, k_ω, k_v, α_1, α_2 be scalar observer gains, L and $s_L(\widehat{R})$ be as defined in Lemma 2, and define the following quantities:*

$$z_1(\widehat{R}) = \frac{s_L(\widehat{R})}{\left(s_L(\widehat{R})^T s_L(\widehat{R})\right)^{1-1/p}}, \tag{7.36}$$

$$z_2(\widehat{b}, \widehat{R}, \bar{a}^m) = \frac{y}{(y^T y)^{1-1/p}}, \tag{7.37}$$

$$\Psi(\widehat{R}, \omega) = \omega - \alpha_1 \, z_1(\widehat{R}), \tag{7.38}$$

$$\Phi(\widehat{b}, \widehat{R}, \bar{a}^m, v) = v + \alpha_2 \, z_2(\widehat{b}, \widehat{R}, \bar{a}^m), \tag{7.39}$$

$$w_L(\widehat{R}, \widehat{\Omega}) = \frac{\mathrm{d}}{\mathrm{d}t} s_L(\widehat{R}) = \mathrm{vex}(L^T \widehat{R} \widehat{\Omega}^\times + \widehat{\Omega}^\times \widehat{R} L) - \mathrm{vex}\left(\widehat{R}^T L \Omega^\times + \Omega^\times L^T \widehat{R}\right) \tag{7.40}$$

$$v_y = \frac{\mathrm{d}}{\mathrm{d}t} y = v + \omega^\times (\bar{q} - y). \tag{7.41}$$

Now, consider the following observer equations:

$$\begin{aligned} \dot{\omega} = {} & k_p s_L - k_p \, \kappa (\bar{q}^\times y) - k_\omega \frac{\Psi}{\left(\Psi^T \Psi\right)^{1-1/p}} \\ & + \frac{\alpha_1}{\left({s_L}^T s_L\right)^{1-1/p}} H(s_L) w_L \\ & - k_p \, \kappa \, \alpha_1 \frac{\Psi}{\Psi^T \Psi} ((\bar{q}^\times y)^T z_1), \end{aligned} \tag{7.42}$$

$$\dot{v} = -k_p \, \kappa \, y - k_v \frac{\Phi}{\left(\Phi^T \Phi\right)^{1-1/p}} - \frac{\alpha_2}{\left(y^T y\right)^{1-1/p}} H(y) v_y, \tag{7.43}$$

$$\widehat{\xi} = \xi^m - \mathrm{Ad}_{\widehat{g}^{-1}}\varphi, \tag{7.44}$$

$$\dot{\widehat{g}} = \widehat{g}\widehat{\xi}^{\vee}, \tag{7.45}$$

where ξ^m and φ are defined as in (7.12) and (7.16), respectively, and the functional dependencies of s_L, w_L, v_y, z_1, z_2, Ψ and Φ have been suppressed for notational convenience, and $H : \mathbb{R}^3 \to Sym(3)$, the space of symmetric 3×3 real matrices, is defined by

$$H(x) = I - \frac{2(1 - 1/p)}{x^T x} x x^T. \tag{7.46}$$

Then the pose and velocities estimation errors (h, φ) converge to $(I, 0) \in \mathrm{SE}(3) \times \mathbb{R}^6$ in a finite time stable manner, from almost all initial conditions except those in a set of measure zero.

Proof. This result gives the observer equations to estimate the pose and velocities in real time, from the measured quantities E^m and ξ^m in a finite-time stable manner.

Consider the following Morse-Lyapunov function:

$$\mathcal{V} = k_p\, \mathcal{U} + \frac{1}{2}\Psi^{\mathrm{T}}\Psi + \frac{1}{2}\Phi^{\mathrm{T}}\Phi, \tag{7.47}$$

where $\mathcal{U}$ is as defined by eq. (7.21). Taking the time derivative along the error state trajectories, we get

$$\dot{\mathcal{V}} = k_p\, \dot{\mathcal{U}} + \Psi^{\mathrm{T}}\dot{\Psi} + \Phi^{\mathrm{T}}\dot{\Phi} \tag{7.48}$$

$$= k_p \left(-s_L(\widehat{R})^{\mathrm{T}}\omega + \kappa\, y^{\mathrm{T}} v + \kappa(\bar{q}^{\times} y)^{\mathrm{T}}\omega \right)$$

$$+ \Psi^{\mathrm{T}}(\dot{\omega} - \alpha_1 \dot{z}_1) + \Phi^{\mathrm{T}}(\dot{v} + \alpha_2 \dot{z}_2), \tag{7.49}$$

where $\dot{z}_1$ and $\dot{z}_2$ are obtained from time derivative of (7.36) and (7.37), respectively, and simplified using (7.40) and (7.46) as

$$\dot{z}_1 = \frac{\mathrm{d}}{\mathrm{d}t} z_1 = \frac{1}{\left(s_L{}^{\mathrm{T}} s_L\right)^{1-1/p}} H(s_L) w_L, \tag{7.50}$$

and

$$\dot{z}_2 = \frac{\mathrm{d}}{\mathrm{d}t} z_2 = \frac{1}{\left(y^{\mathrm{T}} y\right)^{1-1/p}} H(y) v_y. \tag{7.51}$$

Additionally, v_y in (7.51) is given by (7.41) and obtained as follows:

$$\begin{aligned} v_y = \frac{\mathrm{d}}{\mathrm{d}t} y &= \dot{Q}^{\mathrm{T}} \chi + Q^{\mathrm{T}} \dot{\chi} - \dot{Q}^{\mathrm{T}} \bar{q} \\ &= v + \omega^{\times} (Q^{\mathrm{T}} \bar{q} - Q^{\mathrm{T}} \chi) \\ &= v + \omega^{\times} (\bar{q} - y), \end{aligned}$$

using the definitions of $\dot{Q}$, $\dot{\chi}$ in (7.17), and y as given in (7.26). Moreover, w_L in (7.50) is given by (7.40) and obtained using the time derivative of $s_L(\widehat{R})$ as follows:

$$\begin{aligned} w_L = \frac{\mathrm{d}}{\mathrm{d}t} s_L(\widehat{R}) &= \frac{\mathrm{d}}{\mathrm{d}t} \Big(\mathrm{vex}(L^{\mathrm{T}} \widehat{R} - \widehat{R}^{\mathrm{T}} L) \Big) \\ &= \mathrm{vex}\big(\dot{L}^{\mathrm{T}} \widehat{R} + L^{\mathrm{T}} \dot{\widehat{R}} - \dot{\widehat{R}}^{\mathrm{T}} L - \widehat{R}^{\mathrm{T}} \dot{L} \big) \\ &= \mathrm{vex}\Big((L\Omega^{\times})^{\mathrm{T}} \widehat{R} + L^{\mathrm{T}} \widehat{R} \widehat{\Omega}^{\times} - (\widehat{R}\widehat{\Omega}^{\times})^{\mathrm{T}} L - \widehat{R}^{\mathrm{T}} (L\Omega^{\times}) \Big) \\ &= \mathrm{vex}\big(-\Omega^{\times} L^{\mathrm{T}} \widehat{R} + L^{\mathrm{T}} \widehat{R} \widehat{\Omega}^{\times} + \widehat{\Omega}^{\times} \widehat{R}^{\mathrm{T}} L - \widehat{R}^{\mathrm{T}} L \Omega^{\times} \big) \\ &= \mathrm{vex}\big(L^{\mathrm{T}} \widehat{R} \widehat{\Omega}^{\times} + \widehat{\Omega}^{\times} \widehat{R}^{\mathrm{T}} L \big) - \mathrm{vex}\big(\widehat{R}^{\mathrm{T}} L \Omega^{\times} + \Omega^{\times} L^{\mathrm{T}} \widehat{R} \big), \end{aligned}$$

where $L = DWE^{\mathrm{T}}$ and $E = R^{\mathrm{T}}D$, which are true in the absence of measurement noise, and the time derivative of L is obtained as

$$\dot{L} = DW\dot{E}^{\mathrm{T}} = DWE^{\mathrm{T}}\Omega^{\times} = L\Omega^{\times}. \tag{7.52}$$

Now, substituting the equations (7.42) - (7.44), (7.50) and (7.51) into equation (7.49) we get

$$\begin{aligned}
\dot{\mathcal{V}} &= k_p \left(-s_L(\widehat{R})^{\mathrm{T}}\omega + \kappa\, y^{\mathrm{T}}v + \kappa(\bar{q}^{\times}y)^{\mathrm{T}}\omega\right) \\
&\quad + \Psi^{\mathrm{T}}\Bigg(k_p s_L - k_p\,\kappa(\bar{q}^{\times}y) - k_\omega \frac{\Psi}{\left(\Psi^{\mathrm{T}}\Psi\right)^{1-1/p}} \\
&\quad - k_p\,\kappa\,\alpha_1 \frac{\Psi}{\Psi^{\mathrm{T}}\Psi}\left((\bar{q}^{\times}y)^{\mathrm{T}}z_1\right)\Bigg) \qquad (7.53) \\
&\quad + \Phi^{\mathrm{T}}\left(-k_p\,\kappa\,y - k_v \frac{\Phi}{\left(\Phi^{\mathrm{T}}\Phi\right)^{1-1/p}}\right) \\
&= \left(k_p s_L - k_p\,\kappa(\bar{q}^{\times}y)\right)^{\mathrm{T}}(\Psi - \omega) - k_p\,\kappa\,y^{\mathrm{T}}(\Phi - v) \\
&\quad - k_\omega\left(\Psi^{\mathrm{T}}\Psi\right)^{1/p} - k_v\left(\Phi^{\mathrm{T}}\Phi\right)^{1/p} - k_p\,\kappa\,\alpha_1\left((\bar{q}^{\times}y)^{\mathrm{T}}z_1\right) \qquad (7.54) \\
&= -k_p\,\alpha_1\, {s_L}^{\mathrm{T}}z_1 - k_p\,\kappa\,\alpha_2\, y^{\mathrm{T}}z_2 \\
&\quad - k_\omega\left(\Psi^{\mathrm{T}}\Psi\right)^{1/p} - k_v\left(\Phi^{\mathrm{T}}\Phi\right)^{1/p} \qquad (7.55) \\
&= -k_p\left(\alpha_1({s_L}^{\mathrm{T}}s_L)^{1/p} + \kappa\,\alpha_2(y^{\mathrm{T}}y)^{1/p}\right) \\
&\quad - k_\omega\left(\Psi^{\mathrm{T}}\Psi\right)^{1/p} - k_v\left(\Phi^{\mathrm{T}}\Phi\right)^{1/p}. \qquad (7.56)
\end{aligned}$$

Using Lemmas 4 and 5, in the neighborhood of $I \in \mathrm{SO}(3)$, we obtain

$$-{s_L}^{\mathrm{T}}s_L \leq -\mathcal{U}_r\left(\widehat{g}, D, E^m\right) = -\left\langle K, I - Q\right\rangle. \tag{7.57}$$

Substituting (7.57) and (7.18) in (7.56), we get the following inequality for $\dot{\mathcal{V}}$ in terms of $\mathcal{U}_r$, $\mathcal{U}_t$, and $\mathcal{U}$:

$$\begin{aligned}\dot{\mathcal{V}} &\leq -k_p^{1-1/p}\alpha_1(k_p\,\mathcal{U}_r)^{1/p} - 2^{1/p}\alpha_2(k_p\,\kappa)^{1-1/p}(k_p\,\mathcal{U}_t)^{1/p} \\ &\qquad - k_v\left(\Phi^{\mathrm{T}}\Phi\right)^{1/p} - k_\omega\left(\Psi^{\mathrm{T}}\Psi\right)^{1/p} \qquad (7.58)\\ &\leq -k_0\left\{(k_p\,\mathcal{U})^{1/p} + \left(\frac{1}{2}\Phi^{\mathrm{T}}\Phi\right)^{1/p} + \left(\frac{1}{2}\Psi^{\mathrm{T}}\Psi\right)^{1/p}\right\}, \qquad (7.59)\end{aligned}$$

where

$$k_0 = \min\left(k_p^{1-1/p}\alpha_1,\, 2^{1/p}\alpha_2(k_p\,\kappa)^{1-1/p},\, 2^{1/p}k_v,\, 2^{1/p}k_\omega\right),$$

and $\mathcal{U}$ is defined in (7.21) as the total potential function. After applying Lemma 3 to the above inequality, we obtain:

$$\begin{aligned}\dot{\mathcal{V}} &\leq -k_0\left(k_p\,\mathcal{U} + \frac{1}{2}\Phi^{\mathrm{T}}\Phi + \frac{1}{2}\Psi^{\mathrm{T}}\Psi\right)^{1/p} \qquad (7.60)\\ &\leq -k_0\mathcal{V}^{1/p}. \qquad (7.61)\end{aligned}$$

From equation (7.60), the set where $\dot{\mathcal{V}} = 0$ is as

$$\begin{aligned}\dot{\mathcal{V}}(0) &= \{(h,\varphi)\ :\ s_K(Q) = 0,\, Q^{\mathrm{T}}\chi = 0,\, \Phi = 0,\, \text{and } \Psi = 0\}\\ &= \{(h,\varphi)\ :\ s_K(Q) = 0,\, Q^{\mathrm{T}}\chi = 0,\, v = 0,\, \text{and } \omega = 0\}\\ &= \{(h,\varphi)\ :\ s_K(Q) = 0,\, Q^{\mathrm{T}}\chi = 0,\ \text{and } \varphi = 0\}. \qquad (7.62)\end{aligned}$$

From Lemma 1, $s_K(Q) = 0$ when $Q \in \mathcal{C}$, where $\mathcal{C}$ is the set of critical points defined in (7.24). Using the invariance-like result of theorem 8.4 in (Khalil, 2001), we can conclude

that as $t \to \infty$, (h, φ) converges to the set:

$$S = \{(h, \varphi) \ : \ s_K(Q) = 0,\ Q^{\mathrm{T}}\chi = 0,\ \varphi = 0\}, \tag{7.63}$$

where the set S is the largest invariant. In the absence of measurement errors, the attitude estimation error converges to set $\mathcal{C}$ and the position estimation error converges to zero.

The resulting closed-loop system with the pose estimation errors leads to a Hölder-continuous feedback with exponent less than one ($1/p < 1$), while in the limiting case of $1/p = 1$, the feedback system is Lipschitz continuous. Based on the analysis carried out in (Bohn and Sanyal, 2014; Sanyal, Bohn, and Bloch, 2013), it can be inferred that the equilibria and regions of attraction of the Hölder-continuous finite-time stable (FTS) pose observer with $p \in (1, 2)$ are equivalent to those of the corresponding Lipschitz-continuous asymptotically stable observer with $p = 1$. As a result, the observer given by equations (7.42)-(7.45) makes $(h, \varphi) = (I, 0)$ an almost globally finite-time stable (AGFTS) equilibrium for the state estimation errors. □

Note: A more readily implementable version of this FTS pose estimator is given by Proposition 2. This proposition considers the case that translational velocities are not measured directly and filtered versions of the point cloud and angular velocity vector measurements are used.

7.5 Robustness and Pose Estimation without Translational Velocity Measurements

7.5.1 Robustness Analysis

The convergence of almost any initial estimation errors (h, φ) to $(I, 0)$ in an almost globally finite time stable manner in the absence of measurement noise, is shown in Theorem 1. In the presence of a bounded measurement noise $\delta = [\delta_\Omega,\ \delta_v]^{\mathrm{T}}$ in the measurement of angular and translational velocities, the estimation errors will converge to the bounded neighborhood of $(h, \varphi) = (I, 0)$. The following result shows the robustness of the proposed FTS pose estimator to bounded measurement noise. Given the definition of φ in (7.16), the estimation error of velocities in the presence of measurement noise can be expressed as follows:

$$\begin{aligned}\widetilde{\varphi}(\widehat{\mathrm{g}}, \xi^m, \widehat{\xi}) = \begin{bmatrix}\widetilde{\omega}\\ \widetilde{v}\end{bmatrix} &= \mathrm{Ad}_{\widehat{\mathrm{g}}}(\xi^m - \widehat{\xi})\\ &= \mathrm{Ad}_{\widehat{\mathrm{g}}}(\xi + \delta - \widehat{\xi})\\ &= \varphi(\widehat{\mathrm{g}}, \xi, \widehat{\xi}) + \zeta(\widehat{\mathrm{g}}, \delta),\end{aligned} \tag{7.64}$$

where $\widetilde{\omega}$ and $\widetilde{v}$ are angular and translational velocity estimation errors, respectively, ξ^m is given by (7.12), and

$$\zeta(\widehat{\mathrm{g}}, \delta) = \begin{bmatrix}\zeta_\omega\\ \zeta_v\end{bmatrix} \in \mathbb{R}^6, \tag{7.65}$$

where $\zeta(\widehat{\mathrm{g}}, \delta)$ represents the effect of noises. The following result shows the robustness property of the pose estimator to the bounded measurement noise.

Corollary 1. *Consider the pose observer given by equations* (7.42)-(7.45) *and the measured angular and translational velocities given by* (7.12). *Let* $\mathcal{N} \subset \mathcal{H} \times \mathbb{R}^6$ *be the closed neighborhood of* $(I, 0) \in \mathrm{TSE}(3)$ *of pose and velocity estimation errors, defined by*

$$\mathcal{N} = \{(h, \varphi) \in \mathrm{TSE}(3) : \|s_L\| \leq s_{L_{\max}}, \|y\| \leq y_{\max}, \\ \|\bar{q}\| \leq \bar{q}_{\max}, \|\Phi\| \leq \Phi_{\max} \text{ and } \|\Psi\| \leq \Psi_{\max}\}, \quad (7.66)$$

where $\mathcal{H} = \{h \in \mathrm{SE}(3) : Q \in \mathcal{S}, \chi \in \mathbb{R}^3\}$ *and* $\mathcal{S}$ *is defined in* (7.33). *Let the observer gains be selected such that they satisfy the following inequality:*

$$\frac{k_p}{k_{\min}} \leq \frac{s_{L_{\max}}^{2/p} + y_{\max}^{2/p} + \Phi_{\max}^{2/p} + \Psi_{\max}^{2/p}}{\epsilon_{\max}\left(s_{L_{\max}} + \kappa\, y_{\max} + \kappa\, y_{\max}\, \bar{q}_{\max}\right)}, \quad (7.67)$$

where $k_{\min} = \min\{k_v, k_\omega\}$, $\|\zeta_v\| \leq \epsilon_v$, $\|\zeta_\omega\| \leq \epsilon_\omega$, *and* $\epsilon_{\max} = \max\{\epsilon_\omega, \epsilon_v\}$. *Then the estimation errors* (h, φ) *converge to the bounded neighborhood of* $(I, 0)$ *given by* $\mathcal{N}$.

Proof. The robustness analysis for this corollary is based on the Lyapunov analysis in Theorem 1. Consider the measured velocities and velocities estimation error in the presence of measurement noise given in (7.12) and (7.64), respectively. Substituting, φ from (7.16) into (7.64), we obtain

$$\widetilde{\omega} = \omega + \zeta_\omega, \text{ and } \widetilde{v} = v + \zeta_v. \quad (7.68)$$

In the presence of measurement noise, equation (7.49) becomes

$$
\begin{aligned}
\dot{\mathcal{V}} &= k_p \left(-s_L(\widehat{R})^{\mathrm{T}} \widetilde{\omega} + \kappa \, y^{\mathrm{T}} \widetilde{v} + \kappa (\bar{q}^{\times} y)^{\mathrm{T}} \widetilde{\omega} \right) \\
&\quad + \Psi^{\mathrm{T}} (\dot{\omega} - \alpha_1 \dot{z}_1) + \Phi^{\mathrm{T}} (\dot{v} + \alpha_2 \dot{z}_2) \\
&= k_p \left(-s_L(\widehat{R})^{\mathrm{T}} \omega + \kappa \, y^{\mathrm{T}} v + \kappa (\bar{q}^{\times} y)^{\mathrm{T}} \omega \right) \\
&\quad + \Psi^{\mathrm{T}} (\dot{\omega} - \alpha_1 \dot{z}_1) + \Phi^{\mathrm{T}} (\dot{v} + \alpha_2 \dot{z}_2) \\
&\quad + k_p \left(-s_L(\widehat{R})^{\mathrm{T}} \zeta_\omega + \kappa \, y^{\mathrm{T}} \zeta_v + \kappa (\bar{q}^{\times} y)^{\mathrm{T}} \zeta_\omega \right) \\
&= k_p \left(-s_L(\widehat{R})^{\mathrm{T}} \omega + \kappa \, y^{\mathrm{T}} v + \kappa (\bar{q}^{\times} y)^{\mathrm{T}} \omega \right) \\
&\quad + \Phi^{\mathrm{T}} \left(-k_v \frac{\Phi}{\left(\Phi^{\mathrm{T}} \Phi \right)^{1-1/p}} - k_p \, \kappa \, y \right) \\
&\quad + \Psi^{\mathrm{T}} \Bigg(-k_\omega \frac{\Psi}{\left(\Psi^{\mathrm{T}} \Psi \right)^{1-1/p}} + k_p s_L - k_p \, \kappa (\bar{q}^{\times} y) \\
&\quad - k_p \, \kappa \, \alpha_1 \frac{\Psi}{\Psi^{\mathrm{T}} \Psi} \left((\bar{q}^{\times} y)^{\mathrm{T}} z_1 \right) \Bigg) \\
&\quad + k_p \left(-s_L(\widehat{R})^{\mathrm{T}} \zeta_\omega + \kappa \, y^{\mathrm{T}} \zeta_v + \kappa (\bar{q}^{\times} y)^{\mathrm{T}} \zeta_\omega \right) \\
&= -k_p \left(\alpha_1 ({s_L}^{\mathrm{T}} s_L)^{1/p} + \kappa \, \alpha_2 (y^{\mathrm{T}} y)^{1/p} \right) \\
&\quad - k_v \left(\Phi^{\mathrm{T}} \Phi \right)^{1/p} - k_\omega \left(\Psi^{\mathrm{T}} \Psi \right)^{1/p} \\
&\quad + k_p \left(-s_L^{\mathrm{T}} \zeta_\omega + \kappa \, y^{\mathrm{T}} \zeta_v + \kappa (\bar{q}^{\times} y)^{\mathrm{T}} \zeta_\omega \right),
\end{aligned} \tag{7.69}
$$

where we expressed $s_L(\widehat{R}) = s_L$ in the last step above for notational ease. The additional terms in (7.69) when compared to (7.56) are due to measurement noise. Now, considering

the upper bound on the magnitude of these terms, we obtain

$$\begin{aligned}
&\left\| -k_p s_L^{\mathrm{T}} \zeta_\omega + k_p\, \kappa\, y^{\mathrm{T}} \zeta_v + k_p\, \kappa (\bar{q}^{\times} y)^{\mathrm{T}} \zeta_\omega \right\| \leq \left\| -k_p s_L^{\mathrm{T}} \zeta_\omega \right\| \\
&+ \left\| k_p\, \kappa\, y^{\mathrm{T}} \zeta_v \right\| + \left\| k_p\, \kappa (\bar{q}^{\times} y)^{\mathrm{T}} \zeta_\omega \right\| \\
&\leq \left\| k_p \right\| \left(\| s_L \|\, \| \zeta_\omega \| + \| \kappa \|\, \| y \|\, \| \zeta_v \| + \| \kappa \|\, \left\| \bar{q}^{\times} y \right\|\, \| \zeta_\omega \| \right) \\
&\leq k_p \left(s_{L_{\max}} \epsilon_\omega + \kappa\, y_{\max} \epsilon_v + \kappa\, y_{\max}\, \bar{q}_{\max} \epsilon_\omega \right). \qquad (7.70)
\end{aligned}$$

Therefore, $\dot{\mathcal{V}}$ can be upper bounded as

$$\begin{aligned}
\dot{\mathcal{V}} \leq\ & -k_p \left(\alpha_1 ({s_L}^{\mathrm{T}} s_L)^{1/p} + \kappa\, \alpha_2 (y^{\mathrm{T}} y)^{1/p} \right) \\
& - k_v \left(\Phi^{\mathrm{T}} \Phi \right)^{1/p} - k_\omega \left(\Psi^{\mathrm{T}} \Psi \right)^{1/p} \\
& + k_p \left(s_{L_{\max}} \epsilon_\omega + \kappa\, y_{\max} \epsilon_v + \kappa\, y_{\max}\, \bar{q}_{\max} \epsilon_\omega \right). \qquad (7.71)
\end{aligned}$$

The upper bound on $\dot{\mathcal{V}}$ along the boundary of the neighborhood of $\mathcal{N}$ as defined in (7.66) is given by

$$\begin{aligned}
\dot{\mathcal{V}} \leq\ & -k_{\min} \left(s_{L_{\max}}^{2/p} + y_{\max}^{2/p} + \Phi_{\max}^{2/p} + \Psi_{\max}^{2/p} \right) \\
& + k_p \left(s_{L_{\max}} \epsilon_\omega + \kappa\, y_{\max} \epsilon_v + \kappa\, y_{\max}\, \bar{q}_{\max} \epsilon_\omega \right). \qquad (7.72)
\end{aligned}$$

Therefore, the sufficient condition for the convergence of all trajectories starting outside of the neighborhood of $(I, 0)$ to this neighborhood is given by

$$\begin{aligned}
& - k_{\min} \left(s_{L_{\max}}^{2/p} + y_{\max}^{2/p} + \Phi_{\max}^{2/p} + \Psi_{\max}^{2/p} \right) \\
& + k_p \left(s_{L_{\max}} \epsilon_\omega + \kappa\, y_{\max} \epsilon_v + \kappa\, y_{\max}\, \bar{q}_{\max} \epsilon_\omega \right) \leq 0. \qquad (7.73)
\end{aligned}$$

The expression in (7.73) can be also rewritten in terms of a ratio of observer gains as

$$\frac{k_p}{k_{\min}} \leq \frac{s_{L_{\max}}^{2/p} + y_{\max}^{2/p} + \Phi_{\max}^{2/p} + \Psi_{\max}^{2/p}}{s_{L_{\max}}\epsilon_\omega + \kappa\, y_{\max}\epsilon_v + \kappa\, y_{\max}\, \bar{q}_{\max}\epsilon_\omega}. \tag{7.74}$$

Inequality (7.74) relates the ratio $k_p/k_{\min}$ and bounds on the norms of measurement noises (ζ_v, ζ_ω) with bounds on the neighborhood $\mathcal{N}$. Its satisfaction guarantees the convergence of the estimation errors (h, φ) to the neighborhood of $(I, 0)$ given by $\mathcal{N}$. □

7.5.2 FTS Pose Estimator Implementation without Translational Velocity Measurements

The FTS pose estimator is implemented for the case when only angular velocity measurements are available along with position measurements of the feature points. This is a common case of practical interest because rate gyros in inertial measurement units can directly measure angular velocity but translational velocity is not directly measured by sensors onboard aerial vehicles. To implement the FTS pose estimator in this case, a finite-time stable filter is used to obtain filtered values of the measured feature points and measured angular velocity. The filtered feature points are used to construct a filtered estimate of the translational velocity. The filtered versions of the translational and angular velocity vectors are used in this implementation of the FTS pose estimator, as given in the following proposition.

Proposition 2. *Consider the case where only the angular velocity and feature points are directly measured by onboard sensors, but translational velocity is not measured. Let* $c = z^f - z^m$, *where* z^f *is the filtered value of the measured quantity* z^m *at time* t (z^m *could stand for* Ω^m *or* a_i^m).

Consider the continuous-time second-order finite-time stable filter given by:

$$\ddot{z}^f + \left(\frac{\mu}{(c^T c)^{1-1/r}} H(c) + \frac{\gamma}{(l^T l)^{1-1/r}} \right) \dot{z}^f + \frac{\mu}{(c^T c)^{1-1/r}} \frac{\gamma}{(l^T l)^{1-1/r}} c = 0, \tag{7.75}$$

where $r \in]1, 2[$, γ *and* μ *are positive constants,* $H(c)$ *is given by* (7.46)*, and*

$$l := l(c) = \dot{z}^f + \frac{\mu c}{(c^T c)^{1-1/r}}. \tag{7.76}$$

Construct the filtered translational velocity and filtered mean of the measured feature points, as follows:

$$\nu^f = \frac{1}{j} \sum_{i=1}^{j} \left((a_i^f)^\times \Omega^f - v_i^f \right), \text{ where } v_i^f = \dot{a}_i^f, \tag{7.77}$$

$$\bar{a}^f = \frac{1}{j} \sum_{i=1}^{j} a_i^f, \dot{\bar{a}}^f = \frac{1}{j} \sum_{i=1}^{j} \dot{a}_i^f, \text{ and } \xi^f = \begin{bmatrix} \Omega^f \\ \nu^f \end{bmatrix}. \tag{7.78}$$

Thereafter, replace the measured quantities $\bar{a}^m$ *and* ξ^m *in equations* (7.37)*,* (7.39)*, and* (7.44) *in Theorem 1 by the filtered quantities* $\bar{a}^f$ *and* ξ^f*, respectively. This gives the implementation of the FTS pose estimator when translational velocity is not directly measured.*

Proof. Consider the following Lyapunov function:

$$V_f = \frac{1}{2} l^{\mathrm{T}} l. \tag{7.79}$$

Taking the time derivative of V_f and using equations (7.75) and (7.76), we get

$$\dot{V}_f = -\gamma (l^{\mathrm{T}} l)^{1/r} = -\gamma V_f^{1/r}, \tag{7.80}$$

which implies that V_f converges to zero in finite time when z^m is constant and $r \in]1,2[$. Therefore, the quantity $c = z^f - z^m$ will converge to zero in finite time.

Now, consider cases where translational velocity measurements are unavailable or imprecise. Rigid body velocities can be computed using inertial and optical measurements. To achieve this, one can differentiate equation (7.6) to obtain the following:

$$\dot{q}_i = \dot{R}a_i + R\dot{a}_i + \dot{b} = R(\Omega^{\times}a_i + \dot{a}_i + \nu) = 0, \tag{7.81}$$

because the q_i are inertially fixed vectors. This leads to

$$v_i = \dot{a}_i = [a_i^{\times} \ -I]\xi, \tag{7.82}$$

where $[a_i^{\times} \ -I]$ has full row rank and ξ is defined in (7.11). For the case when angular velocity and point cloud measurements are available, the translational velocity of the rigid body can be obtained by filtering the measured points and their velocities and rewriting (7.82) as

$$\nu^f = \frac{1}{j}\sum_{i=1}^{j}\left((a_i^f)^{\times}\Omega^f - v_i^f\right), \tag{7.83}$$

averaging over the i measured points. Therefore, rigid body's filtered velocities ξ^f can be expressed as

$$\xi^f = \begin{bmatrix} \Omega^f \\ \frac{1}{j}\sum_{i=1}^{j}\left((a_i^f)^{\times}\Omega^f - v_i^f\right) \end{bmatrix}. \tag{7.84}$$

This concludes the proof. □

Chapter 8

Simulation and Experimental Results for Pose Estimation Scheme

This chapter presents the simulation and experimental results for pose estimation schemes.

The section 8.1 gives the simulation results for the proposed FTS pose estimator in the absence and presence of noise.

In section 8.2, the proposed FTS pose estimation scheme is compared with two other pose estimation schemes: the variational pose estimator (VPE) and dual quaternion multiplicative extended Kalman filter (DQ-MEKF).

The section 8.3 gives the experimental results for variational pose estimation scheme using vision-based sensors.

8.1 Simulation Results for FTS Pose Observer

This section provides numerical simulation results for the proposed finite-time stable pose observer scheme to demonstrate its performance and the convergence of estimation errors. The proposed FTS pose estimation scheme has been discretized to enable onboard

computer implementation, and the discretization is based on a geometric integration scheme. Geometric variational integration schemes, in contrast to commonly used numerical integration methods such as (unstructured) Runge-Kutta, preserve the geometry of the state space, which in this case is the tangent bundle $\mathrm{TSE}(3)$, without requiring any projection or parametrization. Furthermore, they maintain energy-momentum properties for (corresponding continuous-time) conservative and dissipative systems. Let $\dot{\omega} = \gamma$ and $\dot{v} = \eta$, where γ, η are the right sides of (7.42), (7.43) respectively. Let $\Delta t = t_{i+1} - t_i$ be the time step size and subscript i denote a quantity evaluated at time t_i. Then the discretized equations are obtained as follows:

$$\omega_{i+1} = \omega_i + \Delta t \gamma_i, \tag{8.1}$$

$$v_{i+1} = v_i + \Delta t \eta_i, \tag{8.2}$$

$$\widehat{\xi}_i = \xi_i^m - \mathrm{Ad}_{\widehat{g}_i^{-1}} \varphi_i, \tag{8.3}$$

$$\widehat{g}_{i+1} = \widehat{g}_i \exp(\Delta t \widehat{\xi}_i^{\vee}), \tag{8.4}$$

where

$$\begin{aligned}\gamma_i = {} & k_p s_{L_i} - k_p \, \kappa (\bar{q}^{\times} y_i) - k_\omega \frac{\Psi_i}{\left(\Psi_i{}^{\mathrm{T}} \Psi_i\right)^{1-1/p}} \\ & + \frac{\alpha_1}{\left(s_{L_i}{}^{\mathrm{T}} s_{L_i}\right)^{1-1/p}} H(s_{L_i}) w_{L_i} \\ & - k_p \, \kappa \, \alpha_1 \frac{\Psi_i}{\Psi_i{}^{\mathrm{T}} \Psi_i} ((\bar{q}^{\times} y_i)^{\mathrm{T}} z_{1_i}),\end{aligned} \tag{8.5}$$

$$\eta_i = -k_p \, \kappa \, y_i - k_v \frac{\Phi_i}{\left(\Phi_i{}^{\mathrm{T}} \Phi_i\right)^{1-1/p}} - \frac{\alpha_2}{\left(y_i{}^{\mathrm{T}} y_i\right)^{1-1/p}} H(y_i) v_{y_i}, \tag{8.6}$$

and

$$\varphi_i = \begin{bmatrix} \omega_i \\ v_i \end{bmatrix}. \tag{8.7}$$

Remark 1. *In the absence of linear velocity measurements, the expression for the continuous-time finite-time stable filter (7.75) is discretized by (Sanyal, 2021) as follows:*

$$z^f_{i+1} = z^m_i + \mathcal{D}(c_i)c_i + (\mathcal{D}(z^f_i - z^f_{i-1}))(z^f_i - z^f_{i-1}), \tag{8.8}$$

$$\dot{z}^f_i = \frac{(z^f_{i+1} - z^f_i)}{\Delta t}, \tag{8.9}$$

$$\text{where } \mathcal{D}(c_i) = \frac{(c_i^T c_i)^{1-1/r} - \lambda_c}{(c_i^T c_i)^{1-1/r} + \lambda_c}, \tag{8.10}$$

and $r \in]1,2[$, $\lambda_c > 0$ are constants, $z^f_i = z^f t(i)$ and $z^m_i = z^m t(i)$, respectively. Thereafter, z^m_i is replaced with z^f_i in eq. (8.3) of the discrete-time observer.

The matrix exponential map in (8.4) ensures that the pose at each instant is in $\mathrm{SE}(3)$ provided the initial estimate is in $\mathrm{SE}(3)$. The proposed estimation scheme is simulated with a time step size of $\Delta t = 0.01$s for a duration of $T = 30s$. The initial attitude and position of the rigid body are

$$R_0 = I,\ b_0 = [0\ 0\ 0]^{\mathrm{T}}\mathrm{m}. \tag{8.11}$$

The initial angular and translational velocities of the rigid body, respectively, are

$$\Omega_0 = [0\ 0.15\ 0]^{\mathrm{T}}\ \ \mathrm{rad/s}\ \text{ and }\ \nu_0 = [0.65\ 0\ 0.1]^{\mathrm{T}}\ \mathrm{m/s}. \tag{8.12}$$

The optical measurements are obtained from the vision sensor for j points at time t whose

inertial positions are known. In addition, angular velocities measurements are obtained from rate gyros. The filtered position measurements and velocities are then obtained using the FTS filter given in Proposition 2.

The initial state estimates are selected to be:

$$\begin{aligned}
&\widehat{R}_0 = \exp_{SO(3)}\left(0.9\pi\left([1\ 0\ 0]^{\mathrm{T}}\right)^{\times}\right),\ \widehat{b}_0 = [1.5\ 1\ 1]^{\mathrm{T}},\\
&\widehat{\Omega}_0 = [-0.67\ \ -0.25\ \ -0.09]^{\mathrm{T}}\ \text{rad/s}\ \text{ and}\\
&\widehat{v}_0 = [0.76\ \ -2.63\ 2.83]^{\mathrm{T}}\ \text{m/s}.
\end{aligned} \tag{8.13}$$

The observer gains selected are $k_p = 10.1,\ k_v = 10.02,\ k_\omega = 11.01,\ p = 13/11,\ \kappa = 1.1,\ \alpha_1 = 88.65,\ \alpha_2 = 0.9609$. The proposed FTS pose estimation scheme is simulated for the following two different cases.

8.1.1 CASE 1: Simulation results of FTS pose estimator in the absence of noise

This case exhibits the results of the FTS-PE in the absence of measurement noise but with initial estimation errors, revealing the finite-time convergence of all estimation errors to zero. The true and estimated trajectories over the time interval are depicted in Fig. 8.1. The attitude estimation error is parameterized by the principal rotation angle ϕ of the attitude estimation error matrix Q as $\phi = \cos^{-1}(\frac{1}{2}(\mathrm{tr}(Q) - 1))$. The principal angle ϕ and position estimation error χ are displayed in Fig. 8.2, which show the finite-time convergence of the estimation errors for both attitude and position. Fig. 8.3 demonstrates the finite-time convergence of the angular and translational velocities estimation errors,

agreeing with the finite-time stability of the pose estimation scheme without measurement noise as given by Theorem 1.

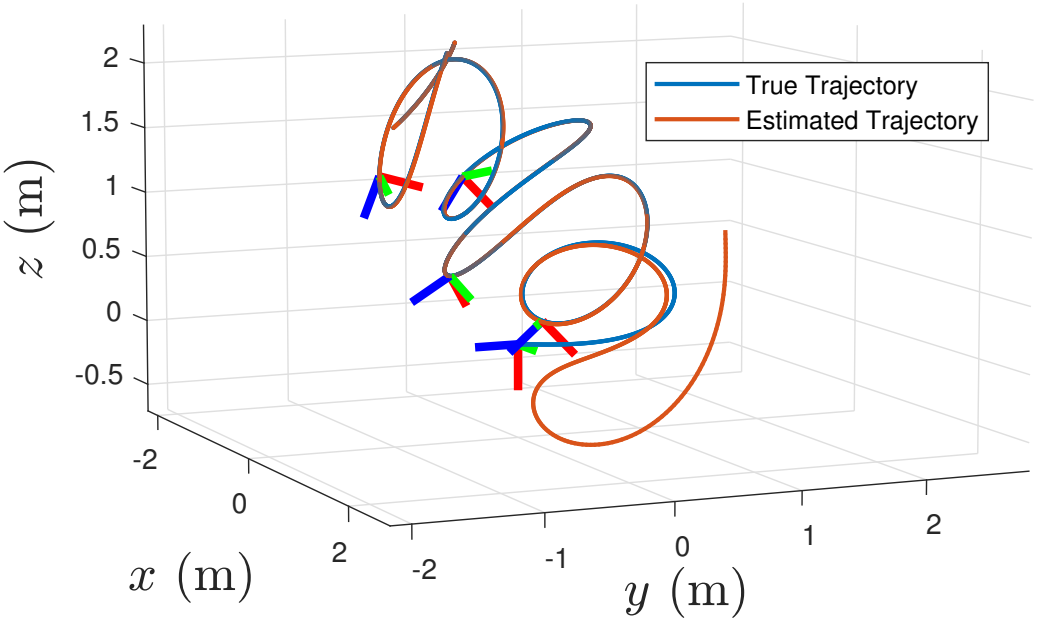

FIGURE 8.1: True and Estimated Trajectories.

8.1.2 CASE 2: Simulation results of FTS pose estimator in the presence of measurement noise in angular and translational velocities

In this case, we consider the effects of measurement noise in angular and translational velocities, using the same initial estimated states as in CASE 1. We assume that both angular and translational velocity measurements are corrupted by Gaussian noise with

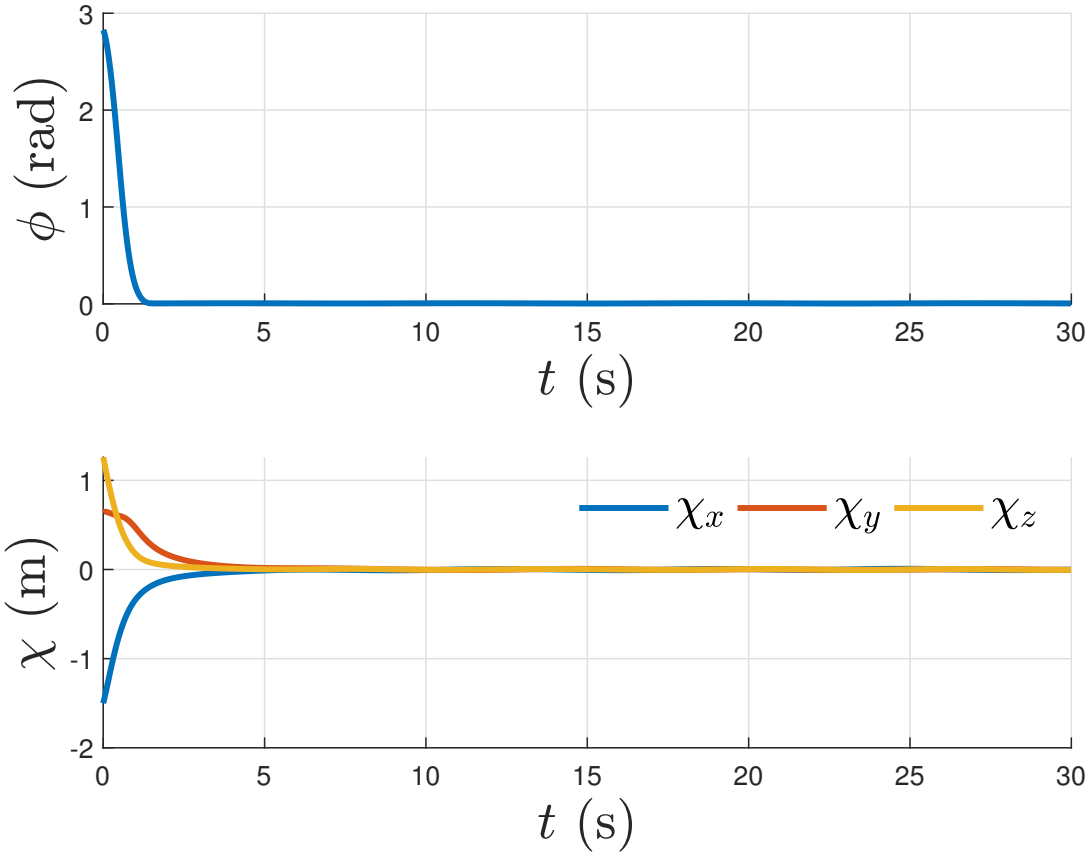

FIGURE 8.2: CASE 1: Plots of attitude and position estimation errors in the absence of measurement noise.

zero mean and standard deviation of $9.1^o/s$ and 0.02 m/s, respectively. The angular and linear velocity estimation errors for CASE 2 are shown in Fig. 8.5, while Fig. 8.4 displays the position error and the principal angle of the attitude estimation error. The simulation results depicted in these figures demonstrate the stability of the proposed FTS pose estimation scheme and the convergence of estimation errors to a neighborhood of $(h, \varphi) = (I, 0)$ despite persistent measurement noise at these relatively high noise levels. The size of this neighborhood depends on the bounds of the measurement noise and the

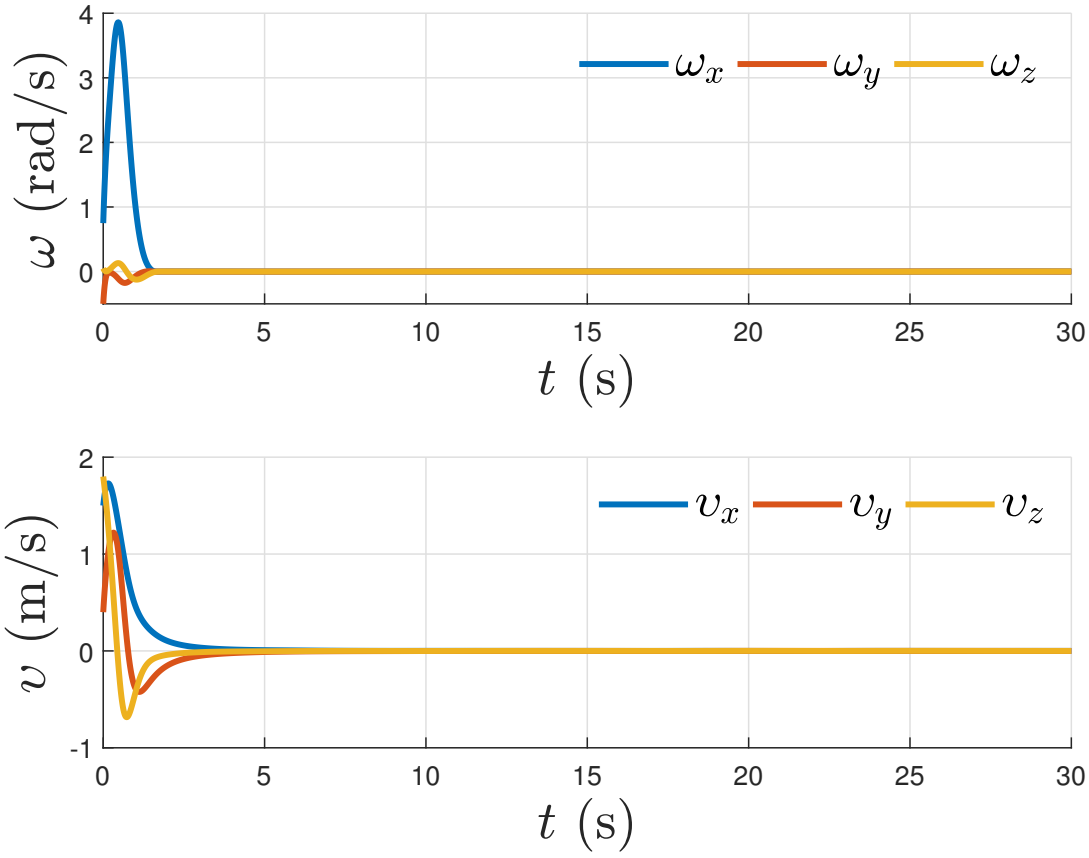

FIGURE 8.3: CASE 1: Plots of estimation errors in velocities in the absence of measurement noise.

observer gains selected, according to Corollary 1. In Fig. 8.6, the plots depict the bounded values of ζ_ω and ζ_v, along with the bounds determined by inequality (7.67) in Corollary 1.

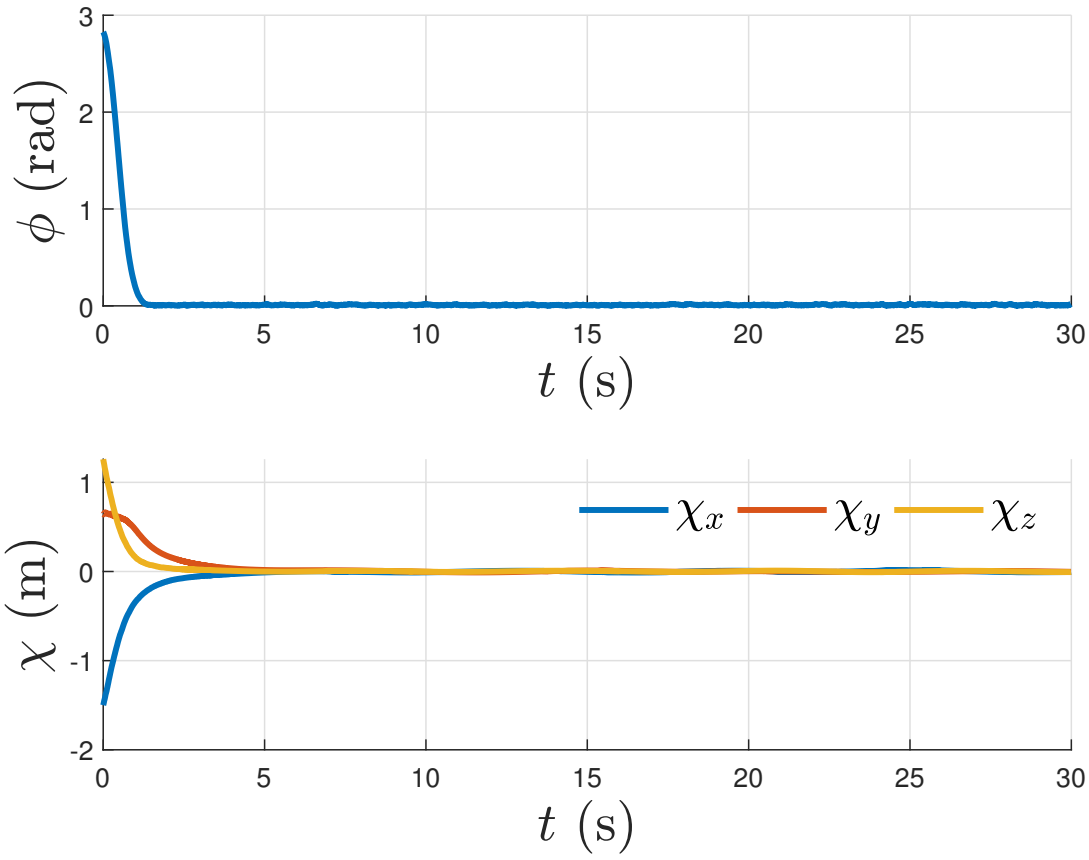

FIGURE 8.4: CASE 2: Plots of attitude and position estimation errors in the presence of measurement noise in velocities.

8.2 Comparison of the state-of-the-art pose estimation schemes

In this section, the proposed FTS pose estimator is compared with the other state-of-the-art pose estimation schemes like variational pose estimatior (VPE) and dual quaternion multiplicative extended Kalman filter (DQ-MEKF).

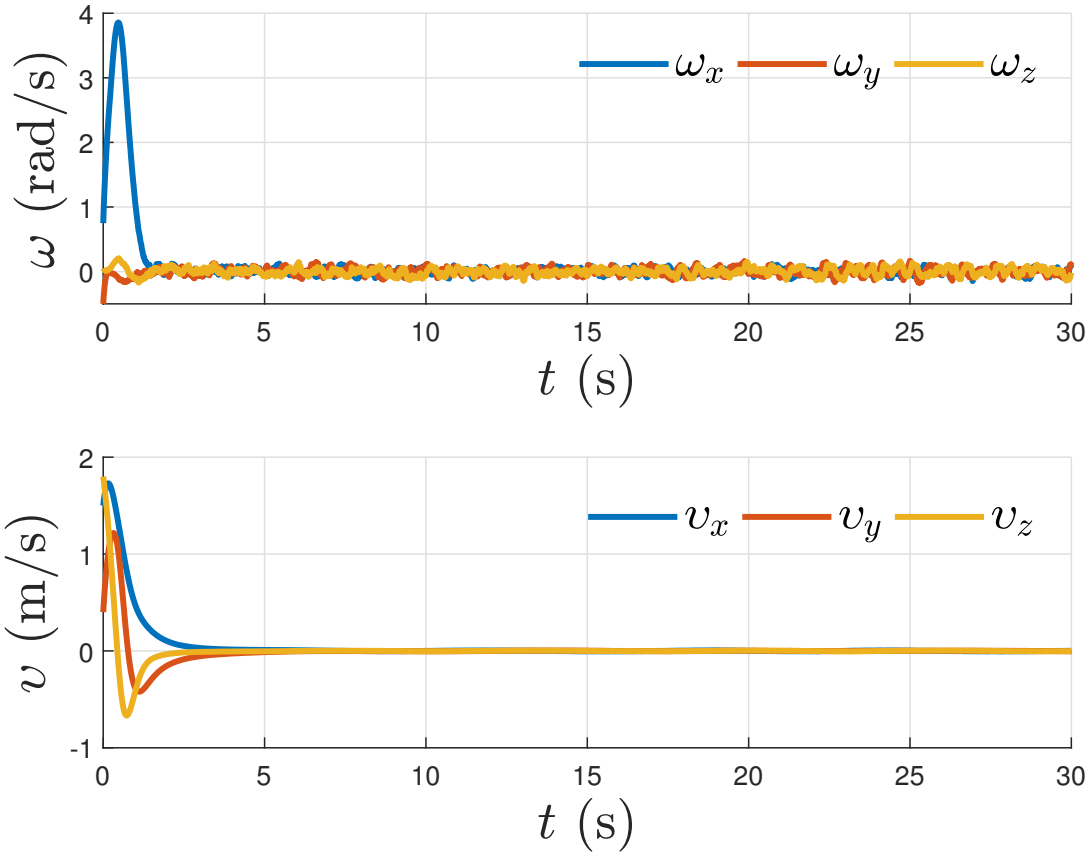

FIGURE 8.5: CASE 2: Plots of estimation errors in velocities in the presence of measurement noise in velocities.

8.2.1 Variational Pose Estimatior

This variational pose estimator in Izadi and Sanyal, 2016 is obtained by applying the LagrangedAlembert principle from variational mechanics to the Lagrangian obtained from measurement residuals along with a Rayleigh dissipation term linear in the velocity measurement residuals. The discretized variational pose estimator is given by:

$$(J\omega_i)^\times = \frac{1}{\Delta t}(F_i\mathcal{J} - \mathcal{J}F_i^{\mathrm{T}}), \tag{8.14}$$

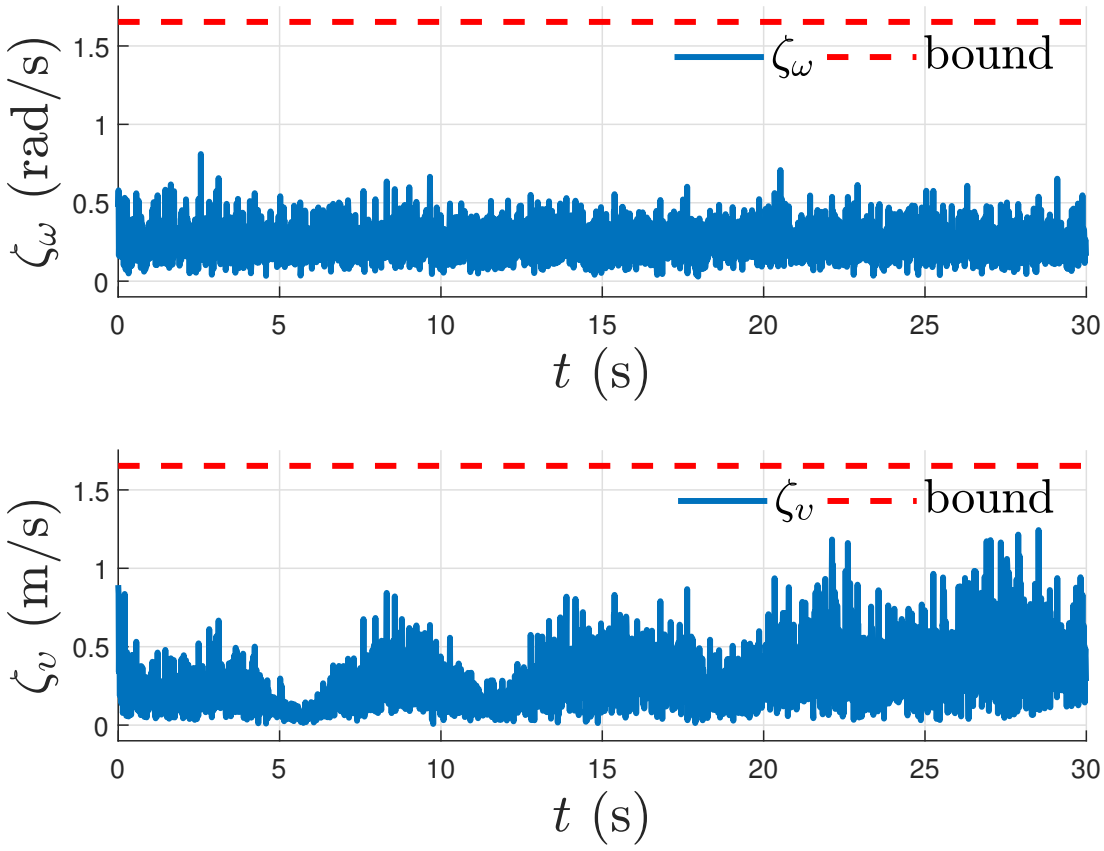

FIGURE 8.6: CASE 2: Plots of bounded measurement noise in velocities.

$$
\begin{aligned}
(M + \Delta t \mathbb{D}_t) v_{i+1} &= F_i^{\mathrm{T}} M v_i \\
&\quad + \Delta t\ \kappa(\hat{b}_{i+1} + \hat{R}_{i+1} \bar{a}^m_{i+1} - \bar{q}_{i+1}), \qquad (8.15) \\
(J + \Delta t \mathbb{D}_r) \omega_{i+1} &= F_i^{\mathrm{T}} J \omega_i + \Delta t M v_{i+1} \times v_{i+1} \\
&\quad + \Delta t\ \kappa\ \bar{q}^{\times}_{i+1} (\hat{b}_{i+1} + \hat{R}_{i+1} \bar{a}^m_{i+1}) \\
&\quad - \Delta t \Phi' \Big(\mathcal{U}^0_r (\hat{\mathrm{g}}_{i+1}, E^m_{i+1}, D_{i+1}) \Big) S_{\Gamma_{i+1}} (\hat{R}_{i+1}), \qquad (8.16) \\
\hat{\xi}_i &= \xi^m_i - \mathrm{Ad}_{\hat{\mathrm{g}}_i^{-1}} \varphi_i, \qquad (8.17) \\
\hat{\mathrm{g}}_{i+1} &= \hat{\mathrm{g}}_i \exp(\Delta t \hat{\xi}^{\vee}_i), \qquad (8.18)
\end{aligned}
$$

where $F_i \in \mathrm{SO}(3)$, Δt is the time step, $J, M, \mathbb{D}_t, \mathbb{D}_r \in \mathbb{R}^{3\times 3}$ are positive definite matrices, $\mathcal{J} = \frac{1}{2}\mathrm{trace}[J]I - J$, $(\hat{\mathrm{g}}(t_0), \hat{\xi}(t_0)) = (\hat{\mathrm{g}}_0, \hat{\xi}_0)$, $\varphi_i = [\omega_i^{\mathrm{T}}\ v_i^{\mathrm{T}}]^{\mathrm{T}}$. The variables $\xi_i^m, \bar{a}_i^m, \bar{q}_i, E_i^m, D_i$ are the discrete-time values of the quantities defined in Section 7.2. Like the FTS pose estimator (FTS-PE) of Theorem 1, it maintains the geometry of the state space of rigid body motions.

8.2.2 DQ-MEKF estimator

The dual quaternion multiplicative extended Kalman filter (DQ-MEKF) is proposed in Filipe, Kontitsis, and Tsiotras, 2015. This filter in the absence of bias is given by:

$$\frac{\mathrm{d}}{\mathrm{d}t}(\hat{\boldsymbol{q}}_{B/I}) \approx \hat{\boldsymbol{q}}^*_{B/I}\boldsymbol{q}_{B/I}, \tag{8.19}$$

$$\hat{\boldsymbol{\omega}}^B_{B/I} = \boldsymbol{\omega}^B_{B/I,m}, \tag{8.20}$$

where $\boldsymbol{q}_{B/I}$ is the unit dual quaternion of a body frame with respect to an inertial frame and is represented by

$$\boldsymbol{q}_{B/I} = q_{B/I,r} + \epsilon q_{B/I,d}, \tag{8.21}$$

and $\boldsymbol{\omega}^B_{B/I}$ is the dual velocity of the body frame with respect to the inertial frame expressed in the body frame. The following constraints are enforced to avoid numerical

errors in the propagation of $\widehat{\boldsymbol{q}}_{B/I}$:

$$
\begin{aligned}
[q_{B/I,r}] &= \frac{[q_{B/I,r}]}{\|[q_{B/I,r}]\|} \qquad \text{and} \\
[q_{B/I,d}] &= \left(I_{4\times 4} - \frac{[q_{B/I,r}][q_{B/I,r}]^{\mathrm{T}}}{\|[q_{B/I,r}]\|^2} \right) [q_{B/I,d}].
\end{aligned} \tag{8.22}
$$

The first equation above is a normalization of the rotation part of the dual quaternion that forces it to be a unit quaternion, and the second is a projection of $[q_{B/I,d}]$ on the orthogonal subspace of $[q_{B/I,r}]$. Together, these steps ensure that the dual quaternion maps to a pose on $\mathrm{SE}(3)$, and they add to the numerical costs of this DQ-MEKF scheme. Thereafter, the covariance matrix $P_{6\times 6}$ of the state satisfies the Riccati equation and is propagated as follows

$$
\begin{aligned}
\dot{P}_{6\times 6}(t) = F_{6\times 6}(t) P_{6\times 6}(t) + P_{6\times 6}(t) F_{6\times 6}^{\mathrm{T}}(t), \\
G_{6\times 6}(t) Q_{6\times 6}(t) G_{6\times 6}^{\mathrm{T}}(t).
\end{aligned} \tag{8.23}
$$

The state estimate at time t_k is then calculated as

$$
\hat{\boldsymbol{q}}_{B/I}^{+}(t_k) = \hat{\boldsymbol{q}}_{B/I}^{-}(t_k) \Delta^{\star} \delta\hat{\boldsymbol{q}}_{B/I}(t_k), \tag{8.24}
$$

where

$$
\begin{aligned}
\boldsymbol{q}_{B/I} &= q_{B/I,r} + \epsilon q_{B/I,d}, \\
\Delta^{\star} \delta\hat{\boldsymbol{q}}_{B/I} &= \left(\sqrt{1 - \left\| \Delta^{\star} \overline{\delta\hat{q}_{B/I,r}} \right\|^2}, \Delta^{\star} \overline{\delta\hat{q}_{B/I,r}} \right)
\end{aligned} \tag{8.25}
$$

$$+\epsilon\left(\frac{-\Delta^{\star}\overline{\delta\hat{q}_{B/I,r}}^{\mathrm{T}}\Delta^{\star}\overline{\delta\hat{q}_{B/I,d}}}{\sqrt{1-\left\|\Delta^{\star}\overline{\delta\hat{q}_{B/I,r}}\right\|^{2}}},\Delta^{\star}\overline{\delta\hat{q}_{B/I,d}}\right), \tag{8.26}$$

when the attitude error between the true and estimated attitude is less than 180 deg. If the attitude error is greater than 180 deg then,

$$\begin{aligned}\Delta^{\star}\delta\hat{\boldsymbol{q}}_{B/I} = &\left(\frac{1}{\sqrt{1+\left\|\Delta^{\star}\overline{\delta\hat{q}_{B/I,r}}\right\|^{2}}},\frac{\Delta^{\star}\overline{\delta\hat{q}_{B/I,r}}}{\sqrt{1+\left\|\Delta^{\star}\overline{\delta\hat{q}_{B/I,r}}\right\|^{2}}}\right)\\ &+\epsilon\left(\frac{-\Delta^{\star}\overline{\delta\hat{q}_{B/I,r}}^{\mathrm{T}}\Delta^{\star}\overline{\delta\hat{q}_{B/I,d}}}{1/\sqrt{1+\left\|\Delta^{\star}\overline{\delta\hat{q}_{B/I,r}}\right\|^{2}}},\Delta^{\star}\overline{\delta\hat{q}_{B/I,d}}\right).\end{aligned} \tag{8.27}$$

Unlike the VPE and FTS-PE, the DQ-MEKF does not maintain the geometry of the state space $\mathrm{TSE}(3)$ and it avoids unwinding, as given in (Bhat and Bernstein, 2000), by using the discontinuous update law given by equations (8.26)-(8.27).

8.2.3 Comparison Results

In this case, the effects of optical vector measurement errors are considered in addition to angular and translational velocities measurement noises. The performance of the FTS pose estimator is compared to the two pose estimators outlined in section 8.2, by utilizing the same initial estimated states used in CASE 1. The time step size for this simulation is $\Delta t = 0.1$s. The optical measurements are obtained at this constant rate by body-fixed sensors with an additive uniform random noise with zero mean and standard deviation of 0.15m. The noise in angular and translational velocity measurements is similar to CASE 2. For a fair comparison, the same measurements are used for all three pose estimation schemes. The tuned gain parameters for both DQ-MEKF and VPE are unchanged and are

as given in (Filipe, Kontitsis, and Tsiotras, 2015) and (Izadi and Sanyal, 2016), respectively. Fig. 8.7 displays the position estimation error and the principal angle of the attitude estimation error. The results from the simulations presented in these plots showcase the stability and performance of FTS-PE and VPE in effectively filtering out noises, unlike DQMEKF. Additionally, FTS-PE ensures the convergence of estimation errors to a neighborhood of $(h, \varphi) = (I, 0)$ in finite time, even when faced with additional noise in optical measurements.

The simulation run-times for all three pose estimators are given in Table 8.1. From this table, one can see that the FTS-PE is the fastest of all the three pose estimators. The simulation run-time values in Table 8.1 are reported for a simulated duration of 30s, using the initial conditions and estimator gains mentioned earlier. In addition, the root-mean-square (RMS) values of attitude and position estimation errors over the simulated time of 30s for the three pose estimators are given in Table 8.2. These RMS values show that the attitude and position estimation errors for the FTS-PE are the lowest. These pose estimators were implemented on a computer with a 3.30 GHz, AMD Ryzen 9 5900HS CPU, and 16 GB of RAM.

Estimator	FTS-PE	DQMEKF	VPE
Run-times	0.0469 s	0.1250 s	0.1094 s

TABLE 8.1: Simulation times for FTS-PE, DQMEKF, and VPE.

Estimator	FTS-PE	DQMEKF	VPE
Attitude error ϕ(rad)	0.3544	0.6806	0.5780
Position error χ(m)	0.2769	0.4336	0.4102

TABLE 8.2: RMS values of attitude and position estimation errors for FTS-PE, DQMEKF, and VPE.

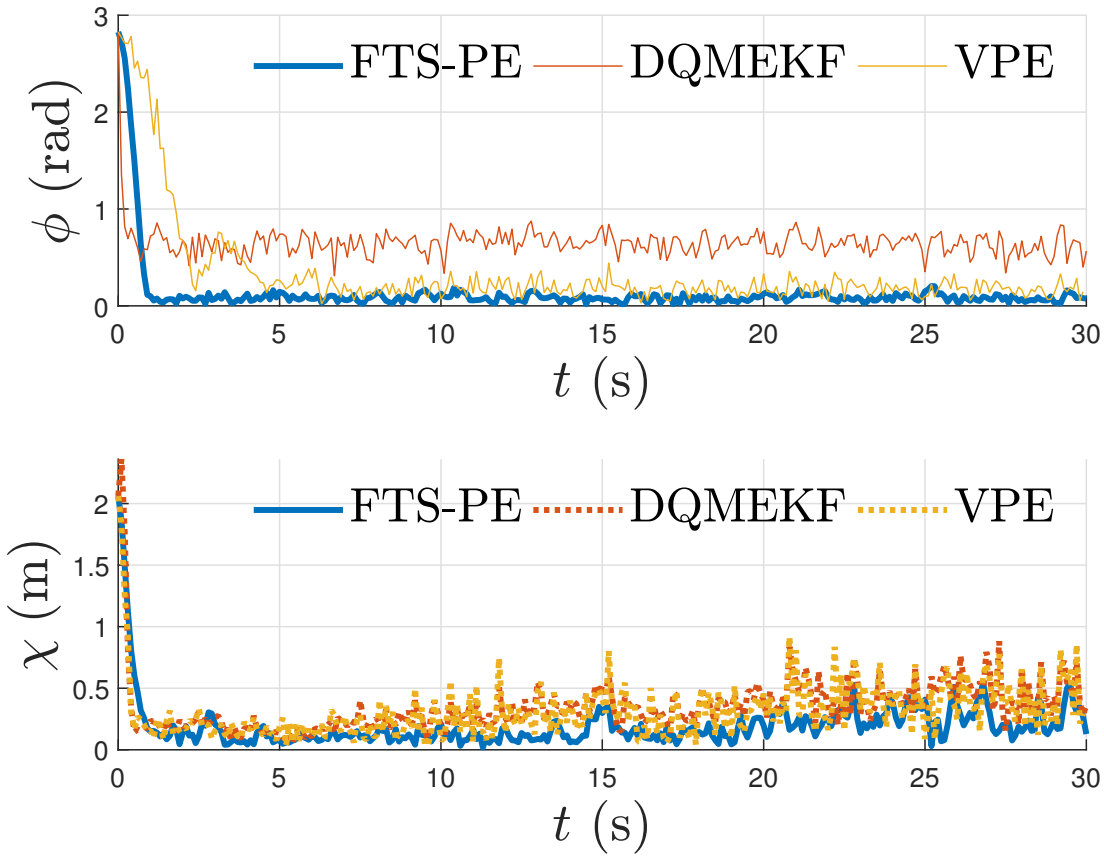

FIGURE 8.7: CASE 3: Plots of attitude and position estimation errors in the presence of measurement noise in all states.

8.3 Experimental Results for Variational Pose Estimation Scheme

In this section, we present the experimental results for VPE from an onboard ZED2i stereo depth camera.

8.3.1 UAV Setup

The experiments were conducted using a hexacopter unmanned aerial vehicle (UAV) developed at the Autonomous Unmanned Systems Laboratory (AUSLab) at the Syracuse Center of Excellence, as illustrated in Fig. This platform is equipped with a Pixhawk 4 autopilot, an advanced control system developed in collaboration with Holybro® and the PX4 team. The autopilot is optimized to run the PX4 control stack PX4 Autopilot Development Team, 2022, making it a suitable option for both academic and commercial developers. The onboard computer of the UAV is an Nvidia Jetson TX2, which is connected to the Pixhawk through the Robot Operating System (ROS) and communicates with a desktop computer via WiFi. The external VICON Motion Capture System is also used to track the UAV for ground truth.

8.3.2 ZED2i Stereo Camera

The ZED2i camera is a stereo camera device designed for depth sensing. It uses a combination of lenses to provide high-precision RGB and depth data. This stereo camera is mounted on the top front of the UAV platform to provide the required color and depth data.

FIGURE 8.8: ZED2i camera used for the experiment.

8.3.3 VICON Motion Capture System

A Vicon system is used as both a reference ground truth and a backup sensor in situations where camera measurements are lost. The Vicon cameras use proprietary algorithms to track reflective markers on the objects being captured and can provide real-time data on position, orientation, and velocity. For our indoor flight tests, we used eight Bonita cameras installed on the ceiling to track the UAV's 6DoF by capturing five markers affixed to the UAV's body. This enabled us to continuously and accurately determine the UAV's pose at each time instant, serving as the ground truth data.

8.3.4 Software Setup

The UAV software packages are designed to run on ROS Melodic, developed for Ubuntu 18.04 LTS. To experimentally validate the efficacy of our proposed VPE scheme, we have tailored the navigation module of the PX4 to run a custom code stack that integrates our estimation algorithm. We also developed a path-planning ROS node to enable communication between the Pixhawk autopilot and the TX2 onboard computer and provide the UAV with the desired pose at any given moment. This node replaced the guidance module of PX4 and publishes the acquired odometry data to the autopilot via Mavlink/Mavros protocols.

8.3.5 Results and Observations

The experimental results for VPE described in 8.2 using the setup described in §8.3.1 - §8.3.4 are given here.

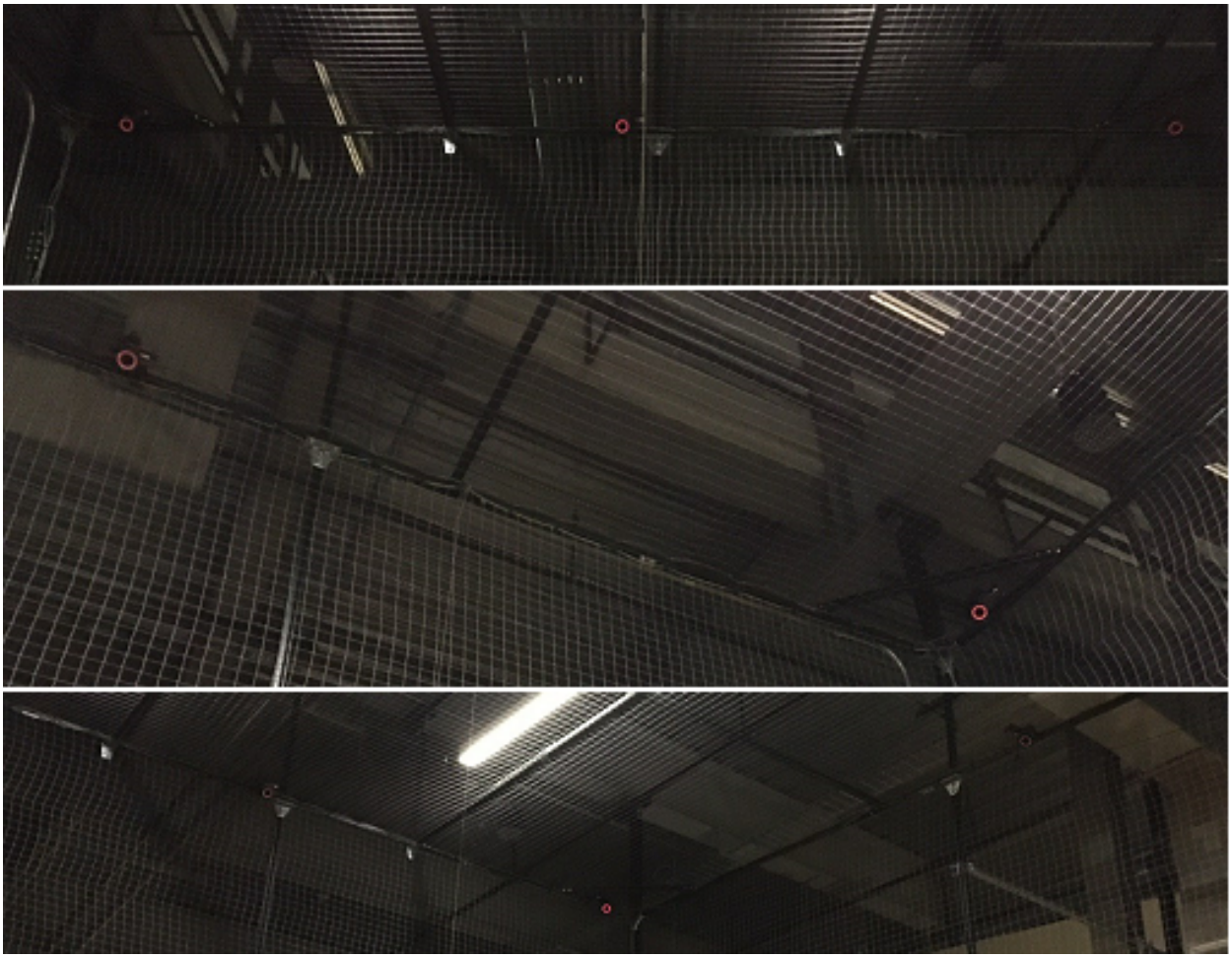

FIGURE 8.9: Vicon motion capture system in the lab

The initial state estimates of the UAV that initialize the VPE are selected as $\hat{R}_0 = I$, $\hat{b}_0 = [0,\ 0,\ 0]^{\mathrm{T}}$m, $\hat{\Omega}_0 = [0,\ 0,\ 0]^{\mathrm{T}}$rad/s, and $\hat{v}_0 = [0,\ 0,\ 0]^{\mathrm{T}}$m/s. The estimator gain matrices are also selected as $J = \mathrm{diag}[2,\ 1,\ 0.6]$, $M = \mathrm{diag}[0.05,\ 0.042,\ 0.03]$, $\mathbb{D}_r = \mathrm{diag}[19.67,\ 18.62,\ 14.2]$, and $\mathbb{D}_t = \mathrm{diag}[0.15,\ 0.15,\ 0.005]$. The estimator's ability to maintain accurate estimates for the two sets of experiments is analyzed and plotted here. These results provide insight into the estimator's performance in comparison to each vicon's measurements. The attitude and position estimation error for the two sets of

experiments is plotted in Fig. 8.10 and Fig. 8.11.

In the first experiment in Fig. 8.10, the VPE is subjected to the noise in the measurements from the ZED2i camera. The attitude and position estimation error remains within the bound. The attitude error, which is given in terms of principal angle, is less than 0.1 rad. The position error for all the three axes is upper-bounded and lower-bounded by 0.2 m.

For the second experiment, in addition to the measurement noise the setup was subjected to more adverse environmental conditions like low-lighting condition, plain walls etc. In this case, the error in both the attitude and position estimation is slightly larger as compared to the attitude and position estimation error in experiment 1. Even with more adverse condition both error remain within the bounds. The attitude error like the previous case is less than 0.1 rad. The position error is slightly more than the previous case due to more adverse conditions, but is less 0.3 m bound.

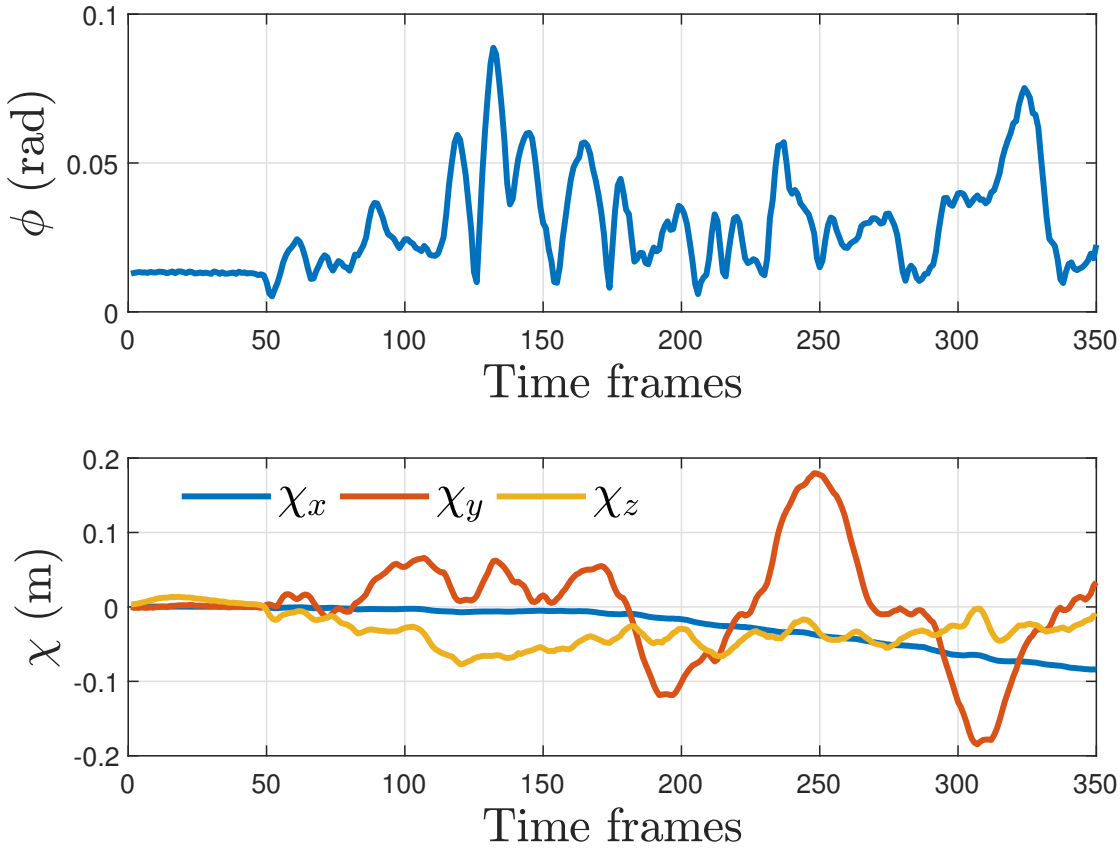

FIGURE 8.10: Experiment 1: Plots of attitude and position estimation errors in the presence of measurement noise in all states.

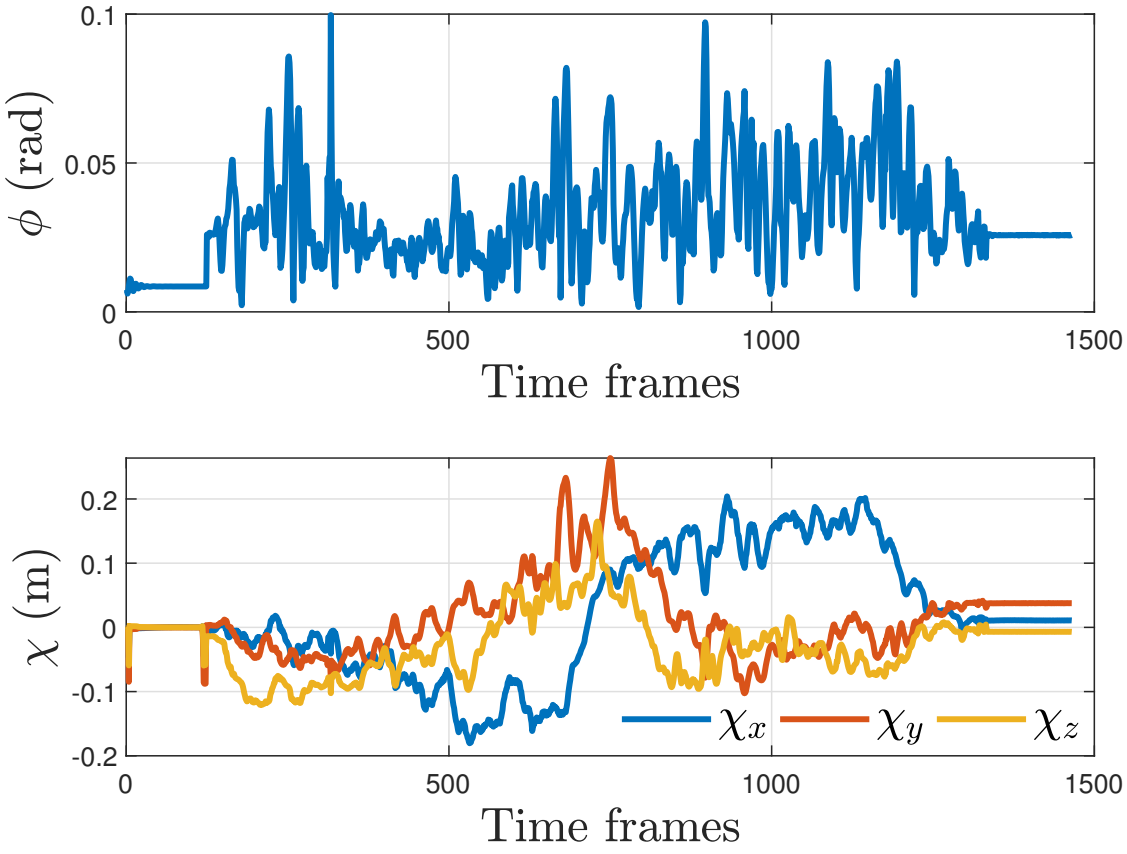

FIGURE 8.11: Experiment 2: Plots of attitude and position estimation errors in the presence of measurement noise in all states.

Chapter 9

Conclusion and Future Work

9.1 Conclusion

We conclude this dissertation by providing a summary of the research presented here, followed by a discussion on related future work.

In Chapter 2, an integrated attitude guidance and tracking scheme that utilizes time-varying artificial potential functions, is proposed. This continuous time scheme is designed directly on the configuration space of rigid-body attitude motion, $SO(3)$. The scheme can generate a desired attitude trajectory through multiple attitude waypoints and then track that desired trajectory through the waypoints. The guidance of the rigid body is achieved by assigning attractive time-varying artificial potentials to desired attitude waypoints, while avoiding undesirable orientations using repulsive potentials. These attractive potentials are generated using asymmetric bump functions of time. A possible future research direction is to consider the full translational and rotational motion of rigid-bodies in $SE(3)$ and create an integrated guidance and control scheme for this full motion. Another research direction is to extend the above scheme to undesirable zones which are dynamic in nature.

Chapter 3, presents a novel scheme for attitude pointing control and guidance of a rigid body with a body fixed sensor. The sensor has to avoid an exclusion zone around an undesirable pointing direction, and is subject to control torque constraints. This scheme relies on the use of an attractive artificial potential to guide the sensor to its desired pointing direction and a repulsive potential to avoid the undesirable pointing direction. A Lyapunov stability analysis for the proposed control law guarantees almost global asymptotic stability of the sensor pointing direction at the desired pointing direction. The control parameters are designed so that they satisfy the control input and pointing direction exclusion zone constraints. Numerical simulations demonstrate the validity of this scheme. The results also show maintenance of the input torque constraints, as a result of the design of control gain parameters.

Chapter 4, considers an application of a recently developed method of integral control barrier functions to guide a control-affine system along safe regions to a target zone, while avoiding unsafe regions and satisfying control constraints. We obtained an integrated guidance and control scheme that solves this problem for control-affine systems under certain assumptions. The comparison of the proposed approach with other approaches, e.g., based on model predictive control and reference governors, will be addressed in future work.

Chapter 5, considers estimation of dynamic uncertain inputs and data-enabled control of a control-affine system for output tracking in discrete time. The dynamics model of the system is partly known, and the uncertain (disturbance) input observer is used to estimate the unknown part of the dynamics. This disturbance observer is designed to be Hölder-continuous and finite-time stable. The data-enabled tracking control scheme uses the disturbance estimate provided by the disturbance observer, for feedforward cancellation

of this disturbance. This control scheme is shown to be finite-time stable in the case of perfect estimation of the disturbance, and robust to this estimation error otherwise.

Chapter 6, considers the design of a reference governor to enforce pointwise-in-time output and control constraints for a system with unknown input-output dynamics modeled by an ULM. At each time instant, a modified command is generated that minimizes the constrained cost function. This command is determined on the basis of a constraint admissible set that is designed to enforce output constraints. The control gain matrix is designed to satisfy the control constraints. A Lyapunov stability analysis shows the convergence of the tracking error and the observer error to bounded neighborhoods of zero error. A numerical simulation is performed for an aircraft pitch control system, subjected to output and control constraints. The simulation results demonstrate the tracking of a reference output trajectory while satisfying the output and control constraints. In the current framework, the output constraint satisfaction for the output trajectory is conservative. This issue will be considered in future work. In addition, the effect of initial selections of the estimate of the unknown model and the control gain matrix on the control input and output response is also illustrated through a numerical simulation study.

Chapter 7, presents theoretical results for a novel nonlinear finite-time stable pose estimation scheme for rigid bodies. The proposed scheme utilizes a minimum of two known linearly independent optical vector measurements from an onboard vision sensor along with inertial vector measurements to estimate pose, angular and translational velocities. It can also be implemented with additional optical sensors to mitigate the effects of measurement noise and sensor failure through sensor redundancy. The FTS pose estimator is Hölder-continuous and model-free, and is designed directly on the Lie group of rigid

body motions, $\mathrm{SE}(3)$. It is shown that the proposed estimator is almost globally finite-time stable from almost all initial conditions except for those in a set of zero measure on $\mathrm{TSE}(3)$. Finite-time stability guarantees a faster convergence of estimation errors in finite time, as well as additional robustness to measurement noise compared to asymptotically or exponentially stable schemes. This work analyzes both finite-time stability and robustness of the FTS pose estimator by using an appropriate Morse-Lyapunov function on $\mathrm{TSE}(3)$. The estimation scheme is discretized using a geometric variational integration scheme that preserves the geometry of the state space. The numerical simulation results validate the efficacy of the proposed estimator by demonstrating its finite-time convergence properties. Moreover, the behavior of this estimation scheme is compared with two state-of-the-art filters for pose estimation. Numerical simulations show that the FTS-PE and VPE, unlike the DQMEKF filter, are always stable and effective in filtering out noise and stable convergence of estimation errors. It is shown that our proposed FTS-PE scheme achieves finite-time stable convergence of estimation errors to $(I, 0)$, and in the presence of measurement noise, it converges to a bounded neighborhood of $(I, 0)$ in finite time.

Chapter 8, given the numerical simulation results and experimental results for the pose estimation schemes given in Chapter 7. The estimation scheme is discretized using a geometric variational integration scheme that preserves the geometry of the state space. The simulation results show that the proposed FTS-PE scheme converges to the zero error in the absence of any measurement noise. In the presence of measurement noise, FTS-PE converges to the bounded neighborhood of zero as shown in the robustness analysis in Chapter 7. Then, the FTS-PE is compared with the two state-of-the-art pose estimators. Numerical simulations show that the FTS-PE and VPE, unlike the DQMEKF filter, are

always stable and effective in filtering out noise and stable convergence of estimation errors. It is shown that our proposed FTS-PE scheme achieves finite-time stable convergence of estimation errors to $(I, 0)$, and in the presence of measurement noise, it converges to a bounded neighborhood of $(I, 0)$ in finite time.

9.2 Ideas for Future Work

The following are ideas to extend the research presented in this PhD dissertation:

- The integral control barrier function approach for state and control constraints in Chapter 4, will be extended for control-affine system in the presence of drift.
- Comparison of efficiency and computational complexities of different methods to satisfy pointwise-in-time output and control constraints, e.g., model predictive control (MPC), reference governors, integral control barrier functions and artificial potential.
- Estimation of control influence matrix when knowledge is not satisfactory and account for bounds in control inputs.
- Development and design of reference governors for systems with uncertainty (“gray box" models), monotonically non-increasing set bounds for the observer error, and systems with delay.
- Future research will look into the problem of discrete-time FTS pose estimation from intermittent measurements and addition of bias. Development of fast finite-time stable pose estimation scheme.

- Experimental validation of data-driven control of systems with unknown input-output dynamics. Inclusion of reference governors to satisfy pointwise-in-time output and control constraints.
- Developing an integral control barrier functions approach for data-driven control of systems with unknown input-output dynamics and for systems with uncertainties.
- Combining finite-time stable pose estimator with finite-time stable control for autonomous systems.

Bibliography

Ames, A. D., J. W. Grizzle, and P. Tabuada (2014). "Control barrier function based quadratic programs with application to adaptive cruise control". In: *53rd IEEE Conf. Decis. and Control*, pp. 6271–6278. DOI: 10.1109/CDC.2014.7040372.

Ames, A. D. et al. (n.d.). "Control Barrier Functions: Theory and Applications". In: *2019 18th European Control Conference (ECC)*, pp. 3420–3431. DOI: 10.23919/ECC.2019.8796030.

Ames, Aaron D. et al. (2021). "Integral Control Barrier Functions for Dynamically Defined Control Laws". In: *IEEE Control Systems Letters* 5.3, pp. 887–892. DOI: 10.1109/LCSYS.2020.3006764.

Assif, M. et al. (2018). "Variational collision avoidance problems on Riemannian manifolds". In: *2018 IEEE Conference on Decision and Control (CDC)*. IEEE.

Aswani, Anil et al. (2013). "Provably safe and robust learning-based model predictive control". In: *Automatica* 49.5, pp. 1216–1226.

Bhat, Sanjay P and Dennis S Bernstein (2000). "A topological obstruction to continuous global stabilization of rotational motion and the unwinding phenomenon". In: *Systems & Control Letters* 39.1, pp. 63–70.

Black, Harold D (1964). "A passive system for determining the attitude of a satellite". In: *AIAA journal* 2.7, pp. 1350–1351.

Blanchini, Franco (1999). "Set invariance in control". In: *Automatica* 35.11, pp. 1747–1767.

Bloch, A.M. (2015). *Nonholonomic Mechanics and Control, ser. Interdisciplinary Applied Mathematics*. Springer, Verlag.

Bloch, A.M. et al. (2003). *Nonholonomic Mechanics and Control, ser. Interdisciplinary Applied Mathematics*. Springer, Verlag.

Boffi, Nicholas et al. (2021). "Learning stability certificates from data". In: *Conference on Robot Learning*. PMLR, pp. 1341–1350.

Bohn, J. and A. K. Sanyal (2014). "Almost global finite-time stable observer for rigid body attitude dynamics". In: *2014 American Control Conference*, pp. 4949–4954.

Bohn, Jan and Amit K Sanyal (2016). "Almost global finite-time stabilization of rigid body attitude dynamics using rotation matrices". In: *International Journal of Robust and Nonlinear Control* 26.9, pp. 2008–2022.

Bonnabel, Silvere, Philippe Martin, and Pierre Rouchon (2009). "Non-linear symmetry-preserving observers on Lie groups". In: *IEEE Transactions on Automatic Control* 54.7, pp. 1709–1713.

Brockett, R. W. (1973). "Lie Theory and Control Systems Defined on Spheres". In: *SIAM Journal on Applied Mathematics* 25.2, pp. 213–225. DOI: 10.1137/0125025. eprint: https://doi.org/10.1137/0125025. URL: https://doi.org/10.1137/0125025.

Brunke, Lukas et al. (2022). "Safe Learning in Robotics: From Learning-Based Control to Safe Reinforcement Learning". In: *Annual Review of Control, Robotics, and Autonomous Systems* 5.1, pp. 411–444. DOI: 10.1146/annurev-control-042920-020211.

Bullo, Francesco and Andrew D Lewis (2004). *Geometric control of mechanical systems: modeling, analysis, and design for simple mechanical control systems*. Vol. 49. Springer Science & Business Media.

Bullo, Francesco and Richard M Murray (1995). "Proportional Derivative (PD) Control on the Euclidean Group". In: *in proceedings of 3rd European Control Conference*.

Chaturvedi, N. A., N. H. McClamroch, and D. S. Bernstein (2009). "Asymptotic Smooth Stabilization of the Inverted 3-D Pendulum". In: *IEEE Transactions on Automatic Control* 54.6, pp. 1204–1215. ISSN: 1558-2523. DOI: 10.1109/TAC.2009.2019792.

Chaturvedi, N. A., A. K. Sanyal, and N. H. McClamroch (2011). "Rigid-Body Attitude Control". In: *IEEE Control Systems Magazine* 31.3, pp. 30–51. ISSN: 1941-000X. DOI: 10.1109/MCS.2011.940459.

Chaturvedi, N.A., A.K. Sanyal, and N.H. McClamroch (2011). "Rigid-body attitude control". In: *Control Systems, IEEE* 31.3, pp. 30–51.

Chaturvedi, Nalin A. and N. Harris McClamroch (2007). "Asymptotic stabilization of the hanging equilibrium manifold of the 3D pendulum". In: *International Journal of Robust and Nonlinear Control* 17.16, pp. 1435–1454. DOI: 10.1002/rnc.1178. eprint: https://onlinelibrary.wiley.com/doi/pdf/10.1002/rnc.1178. URL: https://onlinelibrary.wiley.com/doi/abs/10.1002/rnc.1178.

Chen, Bing et al. (2009). "Novel adaptive neural control design for nonlinear MIMO time-delay systems". In: *Automatica* 45.6, pp. 1554–1560.

Chen, Ziting, Zhijun Li, and CL Philip Chen (2016). "Adaptive neural control of uncertain MIMO nonlinear systems with state and input constraints". In: *IEEE transactions on neural networks and learning systems* 28.6, pp. 1318–1330.

Choukroun, Daniel, Itzhack Y Bar-Itzhack, and Yaakov Oshman (2006). "Novel quaternion Kalman filter". In: *IEEE Transactions on Aerospace and Electronic Systems* 42.1, pp. 174–190.

Coulson, Jeremy, John Lygeros, and Florian Dörfler (2019). "Data-Enabled Predictive Control: In the Shallows of the DeePC". In: *2019 18th European Control Conference (ECC)*, pp. 307–312. DOI: 10.23919/ECC.2019.8795639.

Crassidis, John L, F Landis Markley, and Yang Cheng (2007). "Survey of nonlinear attitude estimation methods". In: *Journal of guidance, control, and dynamics* 30.1, pp. 12–28.

Dai, T. and M. Sznaier (2021). "Nonlinear Data-Driven Control via State-Dependent Representations". In: *2021 60th IEEE Conference on Decision and Control (CDC)*, pp. 5765–5770. DOI: 10.1109/CDC45484.2021.9682919.

De Persis, Claudio and Pietro Tesi (2020). "Formulas for Data-Driven Control: Stabilization, Optimality, and Robustness". In: *IEEE Transactions on Automatic Control* 65.3, pp. 909–924. DOI: 10.1109/TAC.2019.2959924.

Fernando, T. et al. (2011). "Robust adaptive geometric tracking controls on SO(3) with an application to the attitude dynamics of a quadrotor UAV". In: *2011 50th IEEE Conference on Decision and Control and European Control Conference*, pp. 7380–7385. DOI: 10.1109/CDC.2011.6161306.

Filipe, Nuno, Michail Kontitsis, and Panagiotis Tsiotras (2015). "Extended Kalman filter for spacecraft pose estimation using dual quaternions". In: *Journal of Guidance, Control, and Dynamics* 38.9, pp. 1625–1641.

Fliess, Michel (2009). "Model-free control and intelligent PID controllers: towards a possible trivialization of nonlinear control?" In: *IFAC Proceedings Volumes* 42.10, pp. 1531–1550.

Fliess, Michel and Cédric Join (2013). "Model-free control". In: *International Journal of Control* 86.12, pp. 2228–2252. DOI: https://doi.org/10.1080/00207179.2013.810345.

Fry, R. and S. McManus (2002). “Smooth bump functions and the geometry of Banach spaces: a brief survey”. In: *Expositiones Mathematicae* 20.2, pp. 143–183.

Garcia, I. and J. P. How (2005). “Trajectory optimization for satellite reconfiguration maneuvers with position and attitude constraints”. In: *Proceedings of the 2005, American Control Conference, 2005.* 889–894 vol. 2.

Gilbert, Elmer G and Ilya Kolmanovsky (1999). “Fast reference governors for systems with state and control constraints and disturbance inputs”. In: *International Journal of Robust and Nonlinear Control: IFAC-Affiliated Journal* 9.15, pp. 1117–1141.

Goodarzi, Farhad A., Daewon Lee, and Taeyoung Lee (2015). “Geometric control of a quadrotor UAV transporting a payload connected via flexible cable”. In: *International Journal of Control, Automation and Systems* 13, pp. 1486–1498.

Gros, Sébastien and Mario Zanon (2019). “Data-driven economic NMPC using reinforcement learning”. In: *IEEE Transactions on Automatic Control* 65.2, pp. 636–648.

Gupta, R. et al. (2015). “Constrained spacecraft attitude control on SO(3) using fast nonlinear model predictive control”. In: *2015 American Control Conference (ACC)*, pp. 2980–2986.

Hablani, Hari B. (1999). “Attitude Commands Avoiding Bright Objects and Maintaining Communication with Ground Station”. In: *Journal of Guidance, Control, and Dynamics* 22.6, pp. 759–767. DOI: 10.2514/2.4469. eprint: https://doi.org/10.2514/2.4469. URL: https://doi.org/10.2514/2.4469.

Hamel, Tarek, Minh-Duc Hua, and Claude Samson (2020). “Deterministic observer design for vision-aided inertial navigation”. In: *2020 59th IEEE Conference on Decision and Control (CDC)*. IEEE, pp. 1306–1313.

Hamrah, Reza, Rakesh R. Warier, and Amit K. Sanyal (2021). "Finite-time stable estimator for attitude motion in the presence of bias in angular velocity measurements". In: *Automatica* 132, p. 109815. ISSN: 0005-1098.

He, Wei, Yuhao Chen, and Zhao Yin (2015). "Adaptive neural network control of an uncertain robot with full-state constraints". In: *IEEE transactions on cybernetics* 46.3, pp. 620–629.

Hou, Z. and S. Jin (2011). "A Novel Data-Driven Control Approach for a Class of Discrete-Time Nonlinear Systems". In: *IEEE Transactions on Control Systems Technology* 19.6, pp. 1549–1558.

Hu, Q., B. Chi, and M. R. Akella (2019). "Reduced Attitude Control for Boresight Alignment With Dynamic Pointing Constraints". In: *IEEE/ASME Transactions on Mechatronics* 24.6, pp. 2942–2952.

Invernizzi, Davide and Marco Lovera (2017). "Geometric tracking control of a quadcopter tiltrotor UAV". In: *IFAC-PapersOnLine* 50.1. 20th IFAC World Congress, pp. 11565 – 11570. ISSN: 2405-8963.

Isidori, A. (1995). *Nonlinear Control Systems*. 3rd ed.

Izadi, Maziar and Amit K Sanyal (2014). "Rigid body attitude estimation based on the Lagrange–d'Alembert principle". In: *Automatica* 50.10, pp. 2570–2577.

Izadi, Maziar and Amit K. Sanyal (2016). "Rigid body pose estimation based on the Lagrange-d'Alembert principle". In: *Automatica* 71, pp. 78–88.

Izadi, Maziar et al. (2016). "The variational attitude estimator in the presence of bias in angular velocity measurements". In: *2016 American Control Conference (ACC)*, pp. 4065–4070.

Kaiser, Eurika, J Nathan Kutz, and Steven L Brunton (2018). "Sparse identification of nonlinear dynamics for model predictive control in the low-data limit". In: *Proceedings of the Royal Society A* 474.2219, p. 20180335.

Khalil, Hassan K. (2001). *Nonlinear Systems (3rd Edition)*. Prentice Hall: Upper Saddle River, New Jersey.

Khalil, Hassan K (2002). *Nonlinear systems*. Prentice Hall.

Khatib, O. (1985). "Real-time obstacle avoidance for manipulators and mobile robots". In: *Proceedings. 1985 IEEE International Conference on Robotics and Automation*.

— (1986). *The Potential Field Approach And Operational Space Formulation In Robot Control*. Springer, pp. 367–377.

Khatib, O. and J. F. Le Maitre (1978). "Dynamic control of manipulators operating in a complex environment". In: *On Theory and Practice of Robots and Manipulators, 3rd CISM-IFToMM Symp*. Vol. 267.

Kolmanovsky, Ilya and Elmer G Gilbert (1998). "Theory and computation of disturbance invariant sets for discrete-time linear systems". In: *Mathematical problems in engineering* 4.4, pp. 317–367.

Krishnan, Hariharan, Mahmut Reyhanoglu, and Harris McClamroch (1994). "Attitude stabilization of a rigid spacecraft using two control torques: A nonlinear control approach based on the spacecraft attitude dynamics". In: *Automatica* 30.6, pp. 1023 – 1027. ISSN: 0005-1098. DOI: https://doi.org/10.1016/0005-1098(94)90196-1. URL: http://www.sciencedirect.com/science/article/pii/0005109894901961.

Kulumani, S. and T. Lee (2017). "Constrained Geometric Attitude Control on SO(3)". In: *International Journal of Control, Automation and Systems* 15.6.

Kulumani, Shankar and Taeyoung Lee (2017). "Constrained geometric attitude control on SO(3)". In: *International Journal of Control, Automation and Systems* 15.6, pp. 2796–2809. DOI: https://doi.org/10.1007/s12555-016-0607-4.

Kushleyev, Aleksandr et al. (2013). "Towards a swarm of agile micro quadrotors". In: *Autonomous Robots* 35.4, pp. 287–300.

Lageman, Christian, Jochen Trumpf, and Robert Mahony (2010). "Gradient-like observers for invariant dynamics on a Lie group". In: *IEEE Transactions on Automatic Control* 55.2, pp. 367–377.

Lee, Daero, Amit K. Sanyal, and Eric A. Butcher (2015). "Asymptotic Tracking Control for Spacecraft Formation Flying with Decentralized Collision Avoidance". In: *Journal of Guidance, Control, and Dynamics* 38.4, pp. 587–600. DOI: 10.2514/1.G000101. eprint: https://doi.org/10.2514/1.G000101. URL: https://doi.org/10.2514/1.G000101.

Lee, H. et al. (2013). "Backstepping Control on SE(3) of a Micro Quadrotor for Stable Trajectory Tracking". In: *2013 IEEE International Conference on Systems, Man, and Cybernetics*, pp. 4522–4527. DOI: 10.1109/SMC.2013.769.

Lee, T., M. Leok, and N. H. McClamroch (2012). "Nonlinear robust tracking control of a quadrotor UAV on SE(3)". In: *2012 American Control Conference (ACC)*, pp. 4649–4654. DOI: 10.1109/ACC.2012.6315143.

Lee, Taeyoung, Melvin Leok, and N. Harris McClamroch (2010). "Geometric tracking control of a quadrotor UAV on SE(3)." In: *49th IEEE Conference on Decision and Control (CDC)*. IEEE, pp. 5420–5425.

Lee, U. and M. Mesbahi (2011). "Spacecraft Reorientation in Presence of Attitude Constraints via Logarithmic Barrier Potentials". In: *in American Control Conference*, pp. 450–455.

Lee, U. and M. Mesbahi (2011). "Spacecraft reorientation in presence of attitude constraints via logarithmic barrier potentials". In: *Proceedings of the 2011 American Control Conference*, pp. 450–455.

— (2014). "Feedback control for spacecraft reorientation under attitude constraints via convex potentials". In: *IEEE Transactions on Aerospace and Electronic Systems* 50.4, pp. 2578–2592. DOI: 10.1109/TAES.2014.120240.

Leonard, N. E. and E. Fiorelli (Dec. 2001). "Virtual leaders, artificial potentials and coordinated control of groups". In: Orlando, FL, pp. 2968–2973.

Li, Fanbiao et al. (2015). "State estimation and sliding mode control for semi-Markovian jump systems with mismatched uncertainties". In: *Automatica* 51, pp. 385–393.

Li, Weiping and Jean-Jacques E Slotine (1989). "Neural network control of unknown nonlinear systems". In: *1989 American Control Conference*. IEEE, pp. 1136–1141.

Liu, Kaiwen et al. (2019). "Model-free learning to avoid constraint violations: An explicit reference governor approach". In: *2019 American control conference (ACC)*. IEEE, pp. 934–940.

Liu, Kaiwen et al. (2020). "Model-free learning for safety-critical control systems: A reference governor approach". In: *2020 American Control Conference (ACC)*. IEEE, pp. 943–949.

Lopez, I. and C. R. McInnes (1995). "Autonomous Rendezvous Using Articial Potential Function Guidance". In: *Journal of Guidance, Control, and Dynamics* 18.2, pp. 237–241.

Loring, W. Tu (2008). *An Introduction to Manifolds*. Spring.

M. Mancini N. Bloise, E. Capello and E. Punta (2020). "Sliding Mode Control Techniques and Artificial Potential Field for Dynamic Collision Avoidance in Rendezvous Maneuvers". In: *IEEE Control Systems Letters* 4.2, pp. 313–318.

Mahony, Robert and Tarek Hamel (2017). "A geometric nonlinear observer for simultaneous localisation and mapping". In: *Decision and Control (CDC), 2017 IEEE 56th Annual Conference on*. IEEE, pp. 2408–2415.

Mahony, Robert, Tarek Hamel, and Jean-Michel Pflimlin (2008). "Nonlinear complementary filters on the special orthogonal group". In: *IEEE Transactions on automatic control* 53.5, pp. 1203–1218.

Mahony, Robert, Pieter Van Goor, and Tarek Hamel (2022). "Observer design for nonlinear systems with equivariance". In: *Annual Review of Control, Robotics, and Autonomous Systems* 5, pp. 221–252.

Markley, F Landis (2006). "Attitude filtering on SO(3)". In: *The Journal of the Astronautical Sciences* 54.3-4, pp. 391–413.

Markley, F.L. (1988). "Attitude determination using vector observations and the singular value decomposition". In: *The Journal of the Astronautical Sciences* 36.3, pp. 245–258.

Marsden, J. E. and M. West (2001). "Discrete mechanics and variational integrators". In: *Acta Numerica* 10, pp. 357–514.

Mclnnes, Colin R. (1994). "Large angle slew maneuvers with autonomous sun vector avoidance". In: *Journal of Guidance, Control, and Dynamics* 17.4, pp. 875–877. DOI: 10.2514/3.21283. eprint: https://doi.org/10.2514/3.21283. URL: https://doi.org/10.2514/3.21283.

Mellinger, D. and V. Kumar (2011). "Minimum snap trajectory generation and control for quadrotors". In: *2011 IEEE International Conference on Robotics and Automation*, pp. 2520–2525. DOI: 10.1109/ICRA.2011.5980409.

Milnor, J. (1963). *Morse Theory*.

Milnor, J., M. Spivak, and R. Wells (1969). *Morse Theory*. Vol. 51. Princeton University Press. ISBN: 9780691080086. URL: http://www.jstor.org/stable/j.ctv3f8rb6.

Moutinho, Alexandra, Miguel Figueirôa, and José Raul Azinheira (2015). "Attitude estimation in SO (3): A comparative UAV case study". In: *Journal of Intelligent & Robotic Systems* 80.3-4, pp. 375–384.

Murray, Richard M. (2017). *A Mathematical Introduction to Robotic Manipulation*. CRC Press.

Nakano, S. et al. (2018). "Attitude Constrained Control on SO(3): An Explicit Reference Governor Approach". In: *2018 IEEE Conference on Decision and Control (CDC)*, pp. 1833–1838.

Nicotra, M. M. et al. (2020). "Spacecraft Attitude Control With Nonconvex Constraints: An Explicit Reference Governor Approach". In: *IEEE Transactions on Automatic Control* 65.8, pp. 3677–3684.

Nordkvist, N. and Amit K. Sanyal (2010). "A Lie Group Variational Integrator for Rigid Body Motion in SE3 with Applications to Underwater Vehicle Dynamics". In: *49th IEEE Conference on Decision and Control (CDC)*. IEEE, pp. 5414–5419.

Polóni, Tomáš et al. (2014). "Disturbance canceling control based on simple input observers with constraint enforcement for aerospace applications". In: *2014 IEEE Conference on Control Applications (CCA)*. IEEE, pp. 158–165.

Pong, Christopher M. and David W. Miller (2015). "Reduced-Attitude Boresight Guidance and Control on Spacecraft for Pointing, Tracking, and Searching". In: *Journal of Guidance, Control, and Dynamics* 38.6, pp. 1027–1035. DOI: 10.2514/1.G000264. eprint: https://doi.org/10.2514/1.G000264. URL: https://doi.org/10.2514/1.G000264.

Psaltis, Demetri, Athanasios Sideris, and Alan A Yamamura (1988). "A multilayered neural network controller". In: *IEEE control systems magazine* 8.2, pp. 17–21.

PX4 Autopilot Development Team (2022). *Open Source for Drones-PX4 Pro Open Source Autopilot*. https://docs.px4.io/master/en/. Accessed on March 1, 2023.

Renevey, S. and D. A. Spencer (2019). "Spacecraft Formations Using Artificial Potential Functions and Relative Orbital Elements". In: *29th AAS/AIAA Space Flight Mechanics Meeting*,

Rimon, E. and D. E. Koditschek (1992). "Exact Robot Navigation Using Artificial Potential Functions". In: *IEEE Transactions on Robotics and Automation*. Vol. 8. 5. IEEE.

Rudin, Konrad et al. (2011). "A Robust Attitude Controller and its Application to Quadrotor Helicopters". In: *18th IFAC World Congress, Milano (Italy) August 28 - September 2*, pp. 10379–10384.

Sanyal, A. K. (2021). "Discrete-time data-driven control with Hölder-continuous real-time learning". In: *International Journal of Control*, pp. 1–13. DOI: 10.1080/00207179.2021.1901993. eprint: https://doi.org/10.1080/00207179.2021.1901993.

Sanyal, A.K. (2006). "Optimal Attitude Estimation and Filtering Without Using Local Coordinates, Part 1: Uncontrolled and Deterministic Attitude Dynamics". In: *American Control Conference, 2006*. IEEE. Minneapolis, MN, pp. 5734–5739.

— (2022). "Discrete-time data-driven control with Hölder-continuous real-time learning". In: *International Journal of Control* 95.8, pp. 2175–2187.

Sanyal, Amit K., J. Bohn, and A. M. Bloch (2013). "Almost global finite time stabilization of rigid body attitude dynamics". In: *52nd IEEE Conference on Decision and Control*, pp. 3261–3266. DOI: 10.1109/CDC.2013.6760381.

Sanyal, Amit K, Maziar Izadi, and Jan Bohn (2014). "An observer for rigid body motion with almost global finite-time convergence". In: *ASME 2014 Dynamic Systems and Control Conference*. American Society of Mechanical Engineers, V003T41A006–V003T41A006.

Shi, Xiao-Ning, Yong-An Zhang, and Di Zhou (2015). "A geometric approach for quadrotor trajectory tracking control". In: *International Journal of Control* 88.11, pp. 2217–2227. DOI: 10.1080/00207179.2015.1039593.

Shuster, Malcolm D (1990). "Kalman filtering of spacecraft attitude and the QUEST model". In: *Journal of the Astronautical Sciences* 38, pp. 377–393.

Skyrda, Ihor, Valeriy Chepizhenko, and Tetiana Davydenko (2019). "Formation Control of Multiple Autonomous Fixed-Wing Unmanned Aerial Vehicles in Dynamic Environment". In: *Archived Volume*, p. 178.

Spencer, D. A. (2016). "Automated Trajectory Control Using Articial Potential Functions to Target Relative Orbits". In: *Journal of Guidance, Control, and Dynamics* 39.9, pp. 1–7.

Spindler, K (2002). "Attitude Maneuvers Which Avoid a Forbidden Direction". In: *Journal of Dynamical and Control Systems* 8.1, pp. 1–22. DOI: 10.1023/A:1013907732365.

Tanaskovic, Marko et al. (2017). "Data-driven control of nonlinear systems: An on-line direct approach". In: *Automatica* 75, pp. 1–10. ISSN: 0005-1098. DOI: https://doi.org/10.1016/j.automatica.2016.09.032. URL: https://www.sciencedirect.com/science/article/pii/S0005109816303776.

Tatsch, A. and N. Fitz-Coy (2006). "Dynamic Artificial Potential Function Guidance for Autonomous On-Orbit Servicing". In: *6th International ESA Conference on Guidance, Navigation and Control Systems* 606.

Taylor, Andrew J et al. (2021). "Towards robust data-driven control synthesis for nonlinear systems with actuation uncertainty". In: *2021 60th IEEE Conference on Decision and Control (CDC)*. IEEE, pp. 6469–6476.

Tee, Keng Peng, Shuzhi Sam Ge, and Eng Hock Tay (2009). "Barrier Lyapunov Functions for the control of output-constrained nonlinear systems". In: *Automatica* 45.4, pp. 918–927. ISSN: 0005-1098. DOI: https://doi.org/10.1016/j.automatica.2008.11.017.

Tsiotras, Panagiotis and James M. Longuski (1994). "Spin-axis stabilization of symmetric spacecraft with two control torques". In: *Systems & Control Letters* 23.6, pp. 395 –402. ISSN: 0167-6911. DOI: https://doi.org/10.1016/0167-6911(94)90093-0. URL: http://www.sciencedirect.com/science/article/pii/0167691194900930.

Tsiotras, Panagiotis and Jihao Luo (2000). "Control of underactuated spacecraft with bounded inputs". In: *Automatica* 36.8, pp. 1153 –1169. ISSN: 0005-1098. DOI: https://doi.org/10.1016/S0005-1098(00)00025-X. URL: http://www.sciencedirect.com/science/article/pii/S000510980000025X.

Van Goor, Pieter et al. (2021). "Constructive observer design for Visual Simultaneous Localisation and Mapping". In: *Automatica* 132, p. 109803. ISSN: 0005-1098.

Varadarajan, V. S. (1984). *Lie Groups, Lie Algebras, and Their Representations*. Springer New York. DOI: 10.1007/978-1-4612-1126-6.

Vasconcelos, José Fernandes et al. (2010). "A nonlinear position and attitude observer on SE (3) using landmark measurements". In: *Systems & Control Letters* 59.3, pp. 155–166.

Wabersich, Kim P and Melanie N Zeilinger (2018). "Linear model predictive safety certification for learning-based control". In: *2018 IEEE Conference on Decision and Control (CDC)*. IEEE, pp. 7130–7135.

Wahba, Grace (1965). "A least squares estimate of satellite attitude". In: *SIAM review* 7.3, pp. 409–409.

Wang, Weixin, Kanishke Gamagedara, and Taeyoung Lee (2022). "On the observability of attitude with single direction measurements". In: *IEEE Transactions on Automatic Control* 67.9, pp. 4986–4993.

Wang, Zejiang and Junmin Wang (2020). "Ultra-local model predictive control: A model-free approach and its application on automated vehicle trajectory tracking". In: *Control Engineering Practice* 101, p. 104482.

Warier, Rakesh R., Amit K. Sanyal, and Sasi Prabhakaran (2019). "Finite time stable attitude estimation of rigid bodies with unknown dynamics". In: *Asian Journal of Control* 0.0. DOI: 10.1002/asjc.2089.

Warren, C. W. (1990). "Multiple robot path coordination using artificial potential fields". In: *Proceedings. IEEE International Conference on Robotics and Automation*. IEEE.

Wie, Bong and Peter M. Barba (1985). "Quaternion feedback for spacecraft large angle maneuvers". In: *Journal of Guidance, Control, and Dynamics* 8.3, pp. 360–365. DOI: 10.2514/3.19988. eprint: https://doi.org/10.2514/3.19988. URL: https://doi.org/10.2514/3.19988.

Wieland, Peter and Frank Allgöwer (2007). "CONSTRUCTIVE SAFETY USING CONTROL BARRIER FUNCTIONS". In: *IFAC Proceedings Volumes* 40.12. 7th IFAC Symposium on Nonlinear Control Systems, pp. 462–467. ISSN: 1474-6670. DOI: https://doi.org/10.3182/20070822-3-ZA-2920.00076.

Wills, Adrian G and William P Heath (2004). "Barrier function based model predictive control". In: *Automatica* 40.8, pp. 1415–1422.

Yin, Hang, Léa L Cam, and Utpal Roy (2017). "Formation control for multiple unmanned aerial vehicles in constrained space using modified artificial potential field". In: *Math. Model. Eng. Probl* 4.2, pp. 100–105.

Younes, Younes Al et al. (2016). “Robust model-free control applied to a quadrotor UAV”. In: *Journal of Intelligent & Robotic Systems* 84, pp. 37–52.

Zou, An-Min et al. (2011). “Finite-time attitude tracking control for spacecraft using terminal sliding mode and Chebyshev neural network”. In: *IEEE Transactions on Systems, Man, and Cybernetics, Part B (Cybernetics)* 41.4, pp. 950–963.

Dr. Abhijit U. Dongare

Mechanical and Aerospace Engineering

238 Link Hall, Mechanical and Aerospace Engineering, Syracuse University, Syracuse, NY 13244

+1 (610) 714-1745 | audongar@syr.edu | abhidongare | abhijit-dongare

Research Interest

Nonlinear and Geometric Control, Systems Subjected to Constraints, Optimal and Predictive Control, Pose Estimation, Disturbance Observers, Autonomous Unmanned vehicles, Robotics, Spacecraft Dynamics and Control and Astrodynamics.

Education

Syracuse University *Syracuse, NY*

PhD in Mechanical and Aerospace Engineering *2019 - 2023*

- Advisor: Dr. Amit Sanyal.
- Thesis title: Control and Estimation of Unmanned Aerospace Vehicles in the Presence of Constraints and Dynamic Uncertainties

Syracuse University *Syracuse, NY*

MS in Mechanical and Aerospace Engineering *2017 - 2018*

University of Mumbai *Mumbai, India*

BE in Mechanical Engineering *2011 - 2015*

- Project title: Design of Vertical Take-off and Landing Aircraft, advised by: Bharat Kale.

Professional Experience

Research and Teaching Experience

2022-2023 Research Assistant, Mechanical and Aerospace Engineering, Syracuse University.
Pose estimation using variational principle in absence of GPS signal using cameras. Constraint satisfaction for data-driven control using reference governor approach.

2022 Teaching Assistant, Mechanical and Aerospace Engineering, Syracuse University.
Held recitations and office hours for undergraduate Dynamics class.

2021 Research Assistant, Mechanical and Aerospace Engineering, Syracuse University.
Pointing control of rigid body in the presence of pointing direction and control constraints using artificial potential functions. Guidance and Control for a class of Control-affine Systems.

2021 Teaching Assistant, Mechanical and Aerospace Engineering, Syracuse University.
Held recitations and office hours for undergraduate Control Systems class.

2018 Computational analysis of environment on fluid flow and bluff body stabilization of flames.

2018 Teaching Assistant, Mechanical and Aerospace Engineering, Syracuse University.

Work Experience

2021-2023 Akrobotix (start-up)
Snowbotix - Development of autonomous snow removal multi-utility robot.

The concept and prototype development of multi-utility autonomous snow removal robot while considering the customer's need, reliability, safety and design for manufacturability.

2019-2020 Akrobotix (start-up)

NSF SBIR Phase 1: A universal flight management unit for unmanned aircraft systems.

The development of integrated flight management with complete guidance, navigation and control stack for unmanned aerial vehicles.

Publications

Published

1. A. Dongare, R. Hamrah and A. K. Sanyal, "Finite-time Stable Pose Estimation for Unmanned Vehicles in GNSS-denied Environments using an Onboard Camera" accepted in 2024 AIAA SciTech, 8-12 January 2024.
2. A. Dongare, A. K. Sanyal and R. Hamrah, "Discrete-time Control of Nonlinear Control-Affine Systems with Uncertain Dynamics" accepted in Indian Control Conference (ICC-9), 18-20 December 2023.
3. A. Dongare, R. Hamrah, I. Kolmanovsky and A. K. Sanyal, "Reference Governor for Constrained Data-Driven Control of Aerospace Systems with Unknown Input-Output Dynamics" in Conference on Control Technology and Applications (CCTA) 2023, Bridgetown, Barbados.
4. A. Dongare, A. K. Sanyal, I. Kolmanovsky and S. Viswanathan, "Integrated Guidance and Control of Driftless Control-affine Systems with Control Constraints and State Exclusion Zones" in 2022 American Control Conference, ACC 2022, Atlanta, GA USA, June 8-10, 2022.
5. A. Dongare, A. K. Sanyal, and S. P. Viswanathan, "Attitude pointing control using artificial potentials with control input constraints," in 2021 American Control Conference, ACC 2021, New Orleans, LA, USA, May 25-28, 2021, 2021.
6. A. Dongare, A. K. Sanyal, H. Eslamiat and S. P. Viswanathan, "Guidance and Tracking Control for Rigid Body Attitude Using Time-Varying Artificial Potentials" in AAS/AIAA Astrodynamics Specialist Conference, South Lake Tahoe, CA, August 9-13, 2020.

Under Review

1. A. Dongare, R. Hamrah and A. K. Sanyal, "Finite-time Stable Pose Estimation on $\mathrm{SE}(3)$ using Onboard Optical Sensors" submitted to Automatica.

Awards, Fellowships, & Grants

2023 **Nominated for Best Student Paper Award,** Indian Control Conference (ICC-9).

2017-2018 **Academic Scholarship**, Syracuse University.

Outreach & Professional Development

Programming skills

ROS(Robot Operating System), C/C++, Python, Git, Matlab, Julia, Fortran.

Service and Outreach

2014-2015 **Undergraduate Student Association**, Committee Member.

Development

- SAE Baja 2015 - Design and development of All-Terrain Vehicle for SAE Baja.
- Automobile Design Workshop.
- Fuel Cell Technology and Hybrid Cars training program.

Peer Review

- American Control Conference.
- Journal of Intelligent and Robotic Systems.
- International Journal of Control.